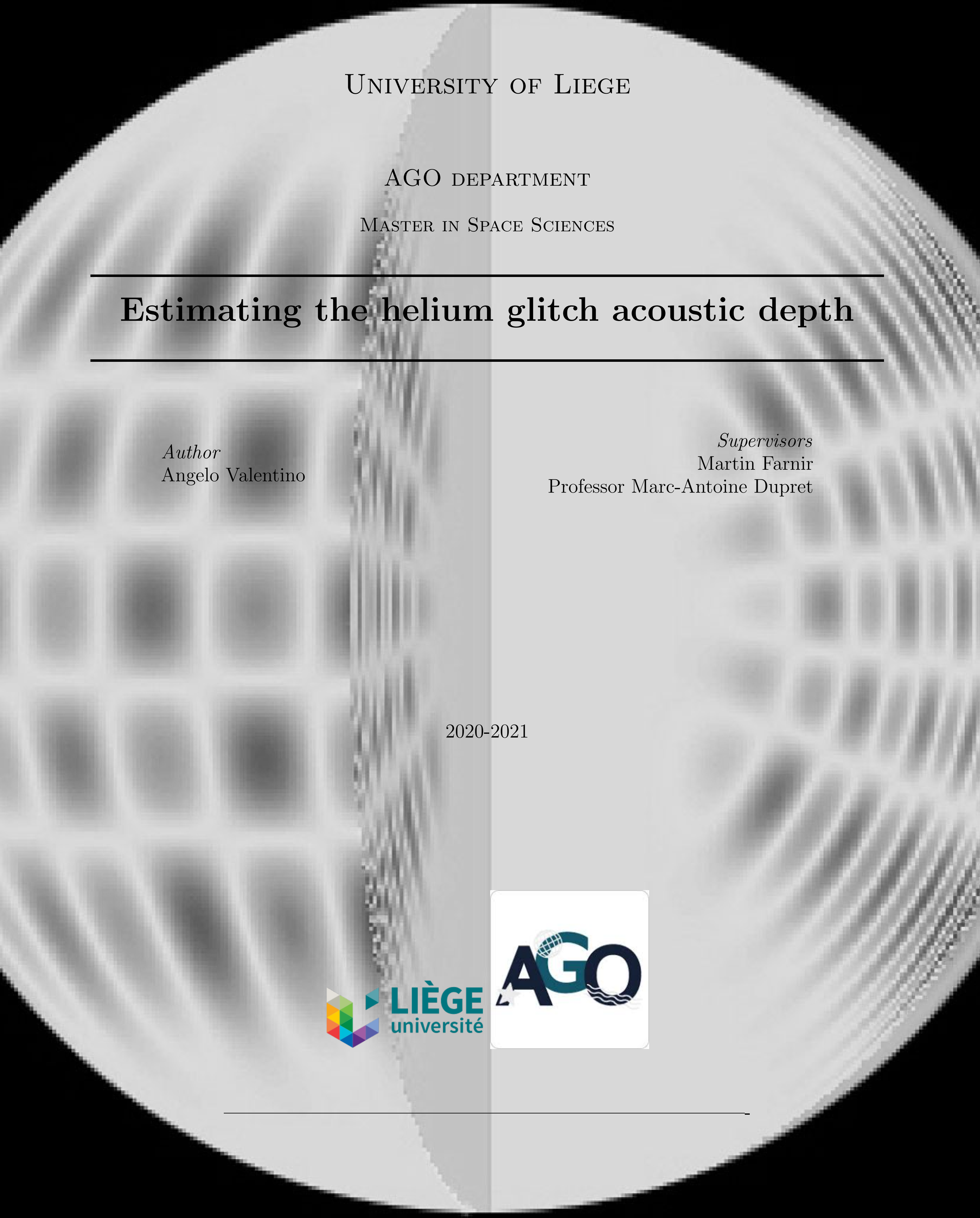

UNIVERSITY OF LIEGE

AGO DEPARTMENT

MASTER IN SPACE SCIENCES

Estimating the helium glitch acoustic depth

Author
Angelo Valentino

Supervisors
Martin Farnir
Professor Marc-Antoine Dupret

2020-2021

Contents

Abstract

In the past decade, space missions, such the CoRoT, Kepler and TESS, have provided the asteroseismic community with a vast amount of observations, of unprecedented quality. This gave the opportunity to stellar astrophysicists, to study the stellar interiors of a large variety of pulsating stars. Amongst them, are the solar-like stars, that are low-mass main-sequence stars, reaching up to 2.3 solar masses.

During the main-sequence phase, the solar-like stars are stable, and they present frequencies that are very regular, which is most obvious in a power spectrum. Nevertheless, there are some departures from that equidistance, to which we refer as the smooth part, and one of the reasons for that, are the glitches. The glitches are due to sharp variations, on the internal structure of the stars, which introduce an oscillatory feature, as a function of the frequency, in the oscillation spectrum. Solar-like stars experience mostly two glitches, the helium glitch, for which our study is about, and the convection zone glitch. The former is located in the second ionization zone of helium, quite close to the stellar surface, and the latter, is located in the transition region between the convective envelope and the radiation zone. The study of those glitches is important, because they provide information about their respective regions, which further helps constrain the internal structure of a star. The amplitude of the helium glitch, is directly linked to the helium abundance, in that area and, since that area is very close to the surface, and convection dominates there, it provides information about the surface helium abundance. This is the only way to obtain that value, because the stellar surface of solar-like stars, does not have the required temperature for the excitation of helium, and thus, few or no emission lines can be obtained spectroscopically.

There exists a number of methods that use the observed frequencies, and derive seismic constraints, which are used to derive information about the stellar structure, through stellar modeling. The one that we used for our analysis, is the Whole Spectrum and Glitches Adjustment (WhoSGlAd). It uses both the smooth part of the spectrum, along with the glitches part, to derive seismic indicators, as little correlated as possible. The accuracy of those indicators, allows them to be used as constraints by minimization techniques, in order to retrieve precise values about global quantities, as is the mass, the age and the chemical composition.

In the case of WhoSGlAd, one of the constraints that is used is the helium glitch amplitude, but for its value we need to know the helium acoustic depth. When we work with observations this value is not available and so, we have to derive it by a model, to estimate the helium acoustic depth, which takes time and it is inconvenient, since it makes the results model dependent. In this study, we propose a method, that uses a linear relation, in order to derive this acoustic depth, which uses only observed quantities and so, makes the procedure much faster. We prove the efficiency and the accuracy of that method, by using both models and observations. This means that it does not make any sacrifices in the precision of WhoSGlAd. Moreover, since this method is linear, and uses only observables, it can be implemented in already existing codes, and provide results much faster. The method, as a result of the assumed linear formulation, does not apply to cases that are not linear. This occurs in cases beyond the main sequence, or with convective cores. This can happen for example, for the case of stars ≥ 1.2 solar masses, for some chemical compositions.

The use of our method can decrease significantly the required computation time, for asteroseismic

data. This can ease the study of big amounts of data, such those expected by future space missions, such as PLATO, in little time.

Chapter 1

Introduction

1.1 Context

The observation of the stars has been taking place since the early ages of the human history, because the night sky would captivate the humans. It is only in the past few centuries however, that we would scientifically study and try to better understand their properties. The only way of studying them is by observing the photons that they emit. Although this is very important in order to get information, like for example its evolutionary stage or spectral type, we cannot retrieve information about their interior, that would help us obtain exact values about their global properties like their mass, age or chemical composition.

The accuracy of those values is important for a number of reasons. First of all, because the stars act as cosmic furnaces for the production of elements heavier than helium, understanding how they evolve, will help us understand how the universe evolves in general. Furthermore, in the past few years, the field of exoplanetology has become very important, with tens to hundreds of exoplanets being discovered every year. This makes it clear that we also need to characterize those exoplanets, so that we can better understand how planetary systems are formed, and if the conditions for the development of life do exist in other places than the Earth. For that, important planetary features such as their mass , their radius, their distance from their host star, their chemical composition, and the size and the chemical composition of their atmosphere, if they have one, have to be known. However, all the methods that those values are derived from, are indirect and they depend on their host's parameters. From that, it is obvious that the more precise is the characterization of a star, the more precise values we will get for the exoplanets that orbit around it. Last but not least, by combining the aforementioned values, with the dynamical properties of the corresponding stars, we can retrieve information about the evolution of the Galaxy.

Those stellar properties are better constrained when we have a picture of the internal structure. Nevertheless, they are not accessible by direct observations because the interior of the stars is optically thick and so no photons can be received from it. As a result, the photons that we observe are produced in the stellar atmosphere, meaning that they carry information only for the conditions of the most superficial layers. In order to understand the internal structure of the stars we use the theory of stellar evolution to build models that give us information about the quantities that we cannot directly observe. Nonetheless, those models are not perfect, since they lack accuracy for important processes that take place in the interior of the stars, like the mixing and transport processes. This creates degeneracies in the possible set of initial conditions, that would result in a specific set of observations and so the determination of the correct set of free parameters becomes difficult.

Asteroseismology uses constrains that are related to the internal structure of the star and that help to lift some of these degeneracies, and to better constrain processes that can significantly affect the evolution of the star. For that, it uses the observed oscillation frequencies on the stellar surfaces, and by analysing them according to the theory of stellar oscillations, it retrieves information about the stellar structure.

During their lifetime, the stars go through several phases, some of them being stable, e.g. the main-sequence phase. Even in that stable phase however, the star oscillates around the equilibrium state. Those oscillations can be quantified, and by studying them, we can find their frequencies and their amplitudes, and so to retrieve information about the stellar interior. This is possible because those oscillations are due to waves, which propagate on the interior of the stars thus, their properties depend on the stellar structure. In the observed frequencies, there are oscillatory departures from the simple theoretical representations. Those departures are called glitches and they are due to sharp variations in the internal structure of the star. The location of those variations in the stellar interior, is called the acoustic depth. In solar like stars, there are mainly two glitches, the helium glitch, which occurs in the second ionization zone of helium, is located very close to the surface and provides an estimate for the helium surface abundance (Y_S), and the convection zone glitch which is due to the transition region between the radiative and convection zones and it is very important in order to constrain its location, and to constrain mixing processes. In the past few decades the field of asteroseismology has grown importantly and is one of the fields that can answer questions about what is happening in the inside of a star, making it possible to further lift the remaining degeneracies on the sets of the free parameters.

One of the most important degeneracies is between the mass and the initial helium abundance (Y_0), as it is shown by Lebreton & Goupil (2014). They showed that there exist several pairs of Y_0 - M solutions. That means that we could easily derive the mass of the star, if we know Y_0, but without a proper measure of Y_0, the determined M is very imprecise. Nonetheless, for solar-like stars, we cannot obtain that value spectroscopically, because their surface is not hot enough to excite helium. As a consequence, few, or even no helium lines are observed. That means that we have to find the helium abundance in a different way, and asteroseismology is one of the few ways to do so. By studying the helium glitch, we can obtain that value. This is because the amplitude of the helium glitch, or simpler the helium amplitude (A_{He}), is directly associated to the helium abundance in that area, and because to its proximity to the stellar surface, and to the fact that this area is convective, we can retrieve the surface helium abundance.

In the present work we propose a method to directly calculate the helium acoustic depth, which is the distance of the Γ_1 depression, that we explain later, to the surface. When working with observations, it is easier and faster to find the helium amplitude, compared to the previous method, and from that the helium abundance.

The way to obtain that value now is complicated, and thus time consuming., because a partial modeling of the structure is necessary to obtain it, and in turn, A_{He}. At the end, the best model, provides us with all the necessary information, in order to obtain the acoustic depths of both glitches. This procedure needs a lot of time, since it requires the generation of a lot of models, but it is the only way to obtain that values when working with observations of solar-like stars. With the proposed method, the helium acoustic depth is retrieved without the need of model generation, thus it is much faster and model independent.

The present thesis is structured as follows. In the present chapter, we present the theoretical background of asteroseismology, that is needed in the understanding of the present work. We begin with some general characteristics of the stellar structure, then we derive the set of equations of the theory of stellar oscillations, and we close with the case of the solar-like stars. In the second chapter, we present the WhoSGlAd method, which is a method to derive seismic indicators from observed or modeled frequencies, and is the method that we used. In the third chapter, we present our analysis and our results. First, we show our proposed method, and construct a grid of models in order to study whether it is efficient or not. Afterwards, we use observed frequencies, from the *Kepler* target KIC10963065, in order to evaluate its efficiency, when working with observations. We also discuss our results, for each case. In the final chapter, we show our conclusions, and discuss future perspectives.

1.2 Stellar structure

1.2.1 Characteristic times

The stellar oscillations are a dynamical phenomenon, which means that we work with the imbalance of forces. So, it is important to remind some important timescales that are needed to understand the further discussion.

Dynamical time: The two forces that determine whether the star will collapse or explode, are the gravity and the gradient of the gas pressure. For a star in a stable state, like the main sequence, those forces cancel each other. If suddenly the pressure would stop to act, then the star would collapse due to gravity. The acceleration of the collapse would be GM/R^2 and the time needed for that, is $R/t_{dyn}^2 \approx GM/R^2$ which results in

$$t_{dyn} = \sqrt{\frac{GM}{R^3}}, \tag{1.1}$$

where G is the gravitational constant, M is the mass of the star and R is its radius. This timescale is important because it is a measure of the time that the star will need to explode, collapse or pulsate, if for some reason the hydrostatic equilibrium is perturbed. For the Sun it is about 26 minutes.

Thermal or Helmholtz - Kelvin time:

$$t_{HK} = \frac{GM^2}{2RL}, \tag{1.2}$$

where L is the luminosity. In some evolutionary stages, the star radiates energy but this energy is not entirely due to thermonuclear reactions. When this happens we say that the star is in thermal imbalance. This will lead to the contraction of the star and we know from the Virial Theorem that half of the released potential energy will be converted into internal energy and the other half will be radiated. If the gas is non-degenerated, the increase of the internal energy will lead to an increase of the temperature. The timescale of this procedure is given by the thermal or Helmholtz - Kelvin time. For the Sun it is about 3.1×10^7 years.

Nuclear time:

$$t_{nuc} = \frac{E_{nuc}}{L}, \tag{1.3}$$

where E_{nuc} is the energy produced by the nuclear reactions. This timescale provides the time for the evolution of the star during a phase of nuclear burning, that it is in both hydrostatic and thermal equilibrium. In that period, the main energy source for the star, are the thermonuclear reactions that occur in its core, for the case of main-sequence stars. Those reactions alter the chemical composition of the core and eventually of the whole star, and this modification is what drives the evolution of the star, during those phases. Because those reactions take a lot of time, this timescale is the longest of the three, and for the Sun it is of the order of 10 billion years.

1.2.2 Stellar hydrodynamics reminder

To understand how the stellar interior is structured, we should first remind some basic equations from hydrodynamics that are used in stellar physics. In fluid dynamics, we can describe the motion of a fluid in two different coordinate systems. In the first one, we use a reference point in space which is fixed and the description is independent of the motion of the fluid. This is called the *Eulerian* description. The second one follows the motion of a specific parcel of matter, and describes the motion of the whole fluid, from that point of view. This is called the *Lagrangian* description, and is the one that we usually use, when studying stellar oscillations, because we consider that the stellar mass does not change, and so we have to take into consideration only the distance from the stellar center, r, in our analysis.

When we use the *Lagrangian* description, the variation with respect to time is not as usual d/dt, like in the *Eulerian* description, but because we follow the motion of the fluid, it is given for a specific quantity, let's say x, by the following relation

$$\frac{Dx}{Dt} = \frac{\partial x}{\partial t} + \nabla x \cdot \boldsymbol{v}, \tag{1.4}$$

where $\boldsymbol{v}$ is the fluid velocity. This relation is called the material derivative and connects the time derivative of the *Lagrangian* description (D/Dt), with the one of the *Eulerian* description ($\partial/\partial t$).

1.2.2.1 Conservartion of mass

The mass must be conserved at any time and this is expressed as

$$\frac{D\rho}{Dt} + \rho\nabla \cdot \boldsymbol{v} = \frac{\partial \rho}{\partial t} + \nabla \cdot (\rho\boldsymbol{v}) = 0, \tag{1.5}$$

where ρ is the density. This equation actually indicates that the rate of change of density in a specific volume, depends on the flow through that volume. Of course, we consider that matter is not created or destroyed inside that volume.

1.2.2.2 Conservation of momentum

In stellar conditions we can neglect viscosity. This comes from the fact that the Reynolds number is very high in those cases due to the very small mean molecular weight (μ) of hydrogen ($Re = \rho V R/\mu$, where Re is the Reynolds number that defines the kind of flow that we will have, and V is the stellar volume). So the forces that act on a volume of gas in a star are the surface forces, like the pressure gradient, and the body forces that act on the whole volume, like gravity. This results in

$$\frac{D\boldsymbol{v}}{Dt} = \frac{\partial \boldsymbol{v}}{\partial t} + \boldsymbol{v} \cdot \nabla\boldsymbol{v} = -\nabla\psi - \frac{\nabla P}{\rho}, \tag{1.6}$$

where ψ represents the potential of the body forces per unit mass. P is for the pressure and represents the force that is exerted on a surface element dA, with the positive direction being the radially outward one.

1.2.2.3 Poisson equation

The only body force that we consider in our analysis is gravity, with the gravitational potential being represented by ψ. That means that the Poisson equation becomes

$$\nabla^2\psi = 4\pi G\rho, \tag{1.7}$$

where ∇^2 is the Laplacian operator.

1.2.2.4 Conservation and transport of energy

In order to describe the conservation of energy in the stars, we have to use the first and second laws of thermodynamics, that connect the heat transfer to the work, and to the entropy, respectively.

$$\frac{Dq}{Dt} = T\frac{Ds}{Dt} = \frac{Du}{Dt} + P\frac{Dv}{Dt}, \tag{1.8}$$

where q is the heat, T is the temperature, s is the specific entropy, u is the internal energy of the gas and v is the specific volume. When we study stellar oscillations, it is more convenient to work with ϵ, which is the rate of energy production per unit mass and per unit time, from nuclear reactions, and with F_R, which is the radiative flux. So equation 1.8 becomes

$$T\frac{Ds}{Dt} = \epsilon - \frac{\nabla \cdot \boldsymbol{F}_R}{\rho}, \tag{1.9}$$

with $\boldsymbol{F}_R$

$$\boldsymbol{F}_R = -\frac{4ac_\star T^3}{3\kappa\rho}\nabla T, \tag{1.10}$$

where a is the radiation density constant, $c_\star$ is the speed of light and κ is the opacity.

In the equation for the conservation of energy, we only considered radiative transfer. We neglegted conduction, because it is negligible for non-degenerated stellar matter. Convection on the other hand is important in the convective layers. In order to describe it, we would have to include in our calculations all the turbulent motions that involve a large spectrum of spatial (the dissipation of heat being of the order of 1 cm and having to be calculated up to the stellar scale), and temporal scales. This is because the convective motion is considered to be in a fully developed state, meaning that it is the dominant way of energy transport there. The analytical approaches, one of which being the mixing length theory, are very approximate, and they need to introduce a number of free parameters. The only way to study convection and oscillations, is to seperate the motions due to those two effects. That would lead to the introduction of the covective flux, it would add in the energy equation and it is given by

$$F_C = \rho c_p V_c \Delta T. \tag{1.11}$$

However, the problem now is that we do not know, how F_C interacts with the oscillations. That means that we do not know how the energy is transferred from the turbulent motions to the oscillations and vice versa, and also we do not know how the oscillations affect the convective motions, and the convective flux. From that discussion, it is clear that convection makes the calculations of the oscillations very complicated, and for that reason we neglect it in our analysis.

In order to see whether convection or radiation will be dominant, we have to see how the gas behaves when a parcel of it is displaced upwards. We assume that the parcel moves much slower than the speed of sound and so, there is pressure equillibrium at all times between the parcel and the surrounding medium. In the following discussion, the index e will correspond to the properties of the parcel at its final position of its displacement, and m will correspond to the properties that the gas around the parcel has at its final position. When there is no index, they will be the properties of the medium and of the parcel at the initial position.

Let's see now the two possible cases. In the first case we have that the density of the element is higher than that of the surrounding medium

$$\rho_e > \rho_m \Leftrightarrow \Delta\rho_e > \Delta\rho_m \Leftrightarrow \frac{\Delta\rho_e}{\rho} > \frac{\Delta\rho_m}{\rho}, \tag{1.12}$$

and that means that the Archimedes force, or else buoyancy, is downwards, and pushes the element back to its initial position. In this case we say that the medium is stable with respect to convection.

The second case is when the density of the parcel is smaller than the medium around it in the position that it arrived,

$$\rho_e < \rho_m \Leftrightarrow \Delta\rho_e < \Delta\rho_m \Leftrightarrow \frac{\Delta\rho_e}{\rho} < \frac{\Delta\rho_m}{\rho}, \tag{1.13}$$

and so, in that case, the total force on the parcel due to the pressure gradient is larger than its weight, the Archimedes force is upwards and pushes the parcel further up. The medium is unstable with respect to convection and the convective motions occur in large scales. In order to find a criterion for convective instability, we consider the gas to be ideal, with $P \propto \rho T \mu$. As we mentioned before there is pressure equillibrium and so we get

$$\frac{\rho_e}{\rho_m} = \frac{T_m}{T_e}\frac{\mu_e}{\mu_m} = \frac{T_m}{T_e}, \tag{1.14}$$

where we assumed that the gas is homogeneous and so $\mu_e = \mu_m$.

From Eqs. 1.13 and 1.14, we have that the convective instability exists only if

$$T_e > T_m \Leftrightarrow \frac{\Delta T_e}{T} > \frac{\Delta T_m}{T}. \tag{1.15}$$

From that result, we get that in convectively unstable regions, the ascending parcels are hotter and less dense than the surrounding medium, while the descending ones are colder and denser. That means that the ascending parcels are taking the heat from the lower levels, and redistribute it in the upper ones. Then, they cool down, and they descend to start the process again. This makes convection an effective mechanism for heat transport towards the exterior.

We can now divide the inequality 1.15 by $\Delta P/P$ and take the limit for infinitesimal changes ($e.g.\, \Delta P/P \to \mathrm{d}\ln P$). This results in

$$\left(\frac{\mathrm{d}\ln T}{\mathrm{d}\ln P}\right)_e < \left(\frac{\mathrm{d}\ln T}{\mathrm{d}\ln P}\right)_m. \tag{1.16}$$

When an element moves upwards, it comes across cooler material and because of that it expands, which helps it cool down and transfer heat to its surrounding medium. So, the heat transfers and, as a result, the decrease of the temperature of the parcel is more efficient than what it would have been in the case of no heat tranfer. So we have

$$\left.\frac{\partial \ln T}{\partial \ln P}\right|_S < \left(\frac{\mathrm{d}\ln T}{\mathrm{d}\ln P}\right)_e < \left(\frac{\mathrm{d}\ln T}{\mathrm{d}\ln P}\right)_m, \tag{1.17}$$

where the first term, called the *adiabatic gradient*, is noted as ∇_{ad} and it is equal to 2/5 for a fully ionized ideal gas, in which we can neglect the radiation pressure. Eq. 1.17 depends only on the local temperature, density and chemical composition, and we say that it is a state variable. The third term of Eq. 1.17, called the *real gradient*, is noted as ∇ and corresponds to the general stratification of the medium. The second term of 1.17 is noted ∇_e. The convective instability is thus given by

$$\nabla > \nabla_e > \nabla_{ad}, \tag{1.18}$$

from which we can write, in a simpler way, the local condition for convective instability

$$\nabla > \nabla_{ad}. \tag{1.19}$$

Since a temperature gradient is always present, radiation will also be present in all parts of the stars, even in convection zones. We can then introduce the *radiative gradient*, which is noted as ∇_{rad}, it describes the total transport of energy only by radiation and is given by

$$\nabla_{rad} = \frac{3\kappa P L}{16\pi a c G m T^4}. \tag{1.20}$$

From that we can now get the Schwarzchild criterion for convective instability:

1. If $\nabla_{rad} > \nabla_{ad}$, then the medium is convectively unstable. When $\nabla > \nabla_{ad}$, we have that $L > L_R$, since convection also carries energy, and thus $\nabla_{rad} > \nabla$. So $\nabla_{rad} > \nabla_{ad}$.

2. If $\nabla_{rad} < \nabla_{ad}$, then the medium is convectively stable. When $\nabla \leq \nabla_{ad}$, we have that $L = L_R$, and thus $\nabla_{rad} = \nabla$. So $\nabla_{rad} \leq \nabla_{ad}$.

where L_R is the power of radiation crossing the sphere of radius r, and it is given by

$$L_R = 4\pi r^2 F = -\frac{16\pi r^2 a c T^3}{3\kappa\rho}\frac{\mathrm{d}T}{\mathrm{d}r} \tag{1.21}$$

1.2.2.5 Equilibrium equations of stellar structure

The stellar oscillations that we study, are small compared to the size of the star, and for that reason we treat them as small perturbations of the equilibrium state. We describe here that equilibrium state. In our analysis, we consider that the stars are not rotating and we also don't take into consideration the magnetic effects, as they are small in main-sequence, low-mass stars. That assumption means that the star is spherically symmetric, and that parameters like density (ρ), pressure (P), and temperature (T), can be described by two variables, their distance from the centre (r) and by time. In order to retrieve the equations for the equilibrium state, we neglect all the time derivatives, and set the velocity ($\boldsymbol{v}$) equal to zero. Moreover, by taking advantage of the fact that the stars are spherical, we can express those equations in the spherical coordinates, and so we get for the conservation of mass

$$\frac{dm}{dr} = 4\pi r^2 \rho, \tag{1.22}$$

for the hydrostatic equilibrium

$$\frac{\mathrm{d}P}{\mathrm{d}r} = -\frac{\rho G m}{r^2}, \tag{1.23}$$

for the conservation of energy

$$\frac{\mathrm{d}L}{\mathrm{d}r} = 4\pi r^2 \rho(\epsilon_n + \epsilon_{grav}), \tag{1.24}$$

where ϵ_n is the production rate of energy by nuclear reactions per unit time and unit mass, and ϵ_{grav} is the energy production rate by contraction. Finally, the transport of energy is

$$\frac{\mathrm{d}T}{\mathrm{d}r} = -\frac{3\kappa\rho L}{16\pi a c_\star r^2 T^3}. \tag{1.25}$$

1.3 Stellar oscillations

In this section we will discuss the derivation of the equations of stellar oscillations.

1.3.1 Small perturbations

The equations for the oscillations are derived by perturbing the equilibrium equations. We consider those perturbations to be sufficiently small and, for that reason, in the linear theory, we only keep the first order terms and we neglect terms of the second order and higher. As it is mentioned earlier, there are two ways to describe those perturbations, the Eulerian description, which is denoted by a prime symbol ($'$), and the Lagrangian description which is denoted by the letter δ, in the following discussion. So we write

$$f(\boldsymbol{r}, t) = f_0(\boldsymbol{r}) + f'(\boldsymbol{r}, t), \tag{1.26}$$

$$f(\boldsymbol{r}, t) = f_0(\boldsymbol{r}_0) + \delta f(\boldsymbol{r}_0, t), \tag{1.27}$$

where the index 0 stands for an equilibrium quantity. The connection between the two descriptions is given by

$$\delta f(\boldsymbol{r}, t) = f'(\boldsymbol{r}, t) + \boldsymbol{\xi} \cdot \nabla f_0(\boldsymbol{r}), \tag{1.28}$$

where $\boldsymbol{\xi} \equiv \boldsymbol{r} - \boldsymbol{r}_0$ is the displacement of first order in the Lagrangian description, and $\cdot$ is the scalar product. The displacement vector $\boldsymbol{\xi}$ shows that, in the unperturbed case, the parcel of matter would be in the position $\boldsymbol{r} = \boldsymbol{r}_0$. The time variations are given by $\mathrm{d}\delta f(\boldsymbol{r}, t)/\mathrm{d}t$ and $\partial f'(\boldsymbol{r}, t)/\partial t$ and those expressions are linked through Eq. 1.4

By applying a Lagrangian perturbation to the mass conservation (Eq. 1.5), by neglecting the derivative of the perturbation, and by integrating over time we get for the continuity equation:

$$\frac{\delta\rho}{\rho} = -\nabla \cdot \delta\boldsymbol{r}, \tag{1.29}$$

for the equation for the conservation of momentum (Eq. 1.6) we use that

$$\boldsymbol{v} = \frac{\partial \delta\boldsymbol{r}}{\partial t}, \tag{1.30}$$

and that $\boldsymbol{v} = 0$ in the equilibrium configuration. Then we take the perturbation of Eq. 1.5 and we get

$$\frac{\partial^2 \delta\boldsymbol{r}}{\partial t^2} = -\nabla\psi' - \frac{\nabla P'}{\rho} + \frac{\rho'}{\rho^2}\nabla P, \tag{1.31}$$

and for the Poisson equation (Eq. 1.7) we get

$$\nabla^2\psi' = 4\pi G\rho'. \tag{1.32}$$

We saw in section 1.2.1 the important time-scales that we have to take into consideration, when studying stellar oscillations. Those are the dynamical time (t_{dyn}), the thermal or Helmholtz-Kelvin time (t_{HK}) and the nuclear time (t_{nuc}), and their values for the Sun are approximately 26 minutes, 10^7 years, and 10^{10} years, respectively. The amount of heat that is exchanged by a parcel of matter in the timescale of one oscillation, is denoted ΔQ and is proportional to the t_{dyn}, and more specifically $\mid \Delta Q \mid \simeq L t_{dyn}$. From the Virial theorem however, we know that the energy released by contraction is converted into internal energy:

$$\int_0^M \frac{GM}{R}\mathrm{d}m = 2\int_0^M u\mathrm{d}m. \tag{1.33}$$

By replacing that equation in the Helmholtz-Kelvin time, that gives an estimate for the thermal exchanges we get

$$t_{HK} = \frac{GM^2}{2RL} \simeq \frac{1}{L}\int \frac{GM}{R}\mathrm{d}m \simeq \frac{\int_0^M u\mathrm{d}m}{L} \simeq \frac{uM}{L}, \tag{1.34}$$

which is much larger than the dynamical time. Also, we assumed that u remains constant with respect to m. From that we can derive

$$t_{dyn} = \frac{\Delta Q}{L} \ll \frac{uM}{L} \Rightarrow \Delta Q \ll uM \simeq c_v T M, \tag{1.35}$$

where we have also used from thermodynamics that $u = c_v T$, with c_v being the heat capacity at constant volume. From that discussion, it is obvious that, in the timescale of the oscillations, that we study, the gas does not have enough time to exchange significant amounts of heat, when we compare it to the global heat capacity of the star. That means that the oscillations are adiabatic and so, we can neglect the heat diffusion term in the equations. It is important to mention here that this is not the case everywhere in the star. In the layers near the stellar surface, the heat exchange per unit mass is of about the same order as the internal energy $\Delta Q \simeq u = c_v T$, which means that the oscillations there are non-adiabatic. The area where the oscillations are adiabatic is seperated from the non-adiabatic area by the transition region.

The relation between the density (ρ) and the pressure (P) in the adiabatic case, is given by

$$\frac{\mathrm{d}\ln P}{\mathrm{d}\ln\rho} = \left.\frac{\partial \ln P}{\partial \ln\rho}\right|_s \equiv \Gamma_1 \Rightarrow \frac{\delta P}{P} = \delta(\ln P) = \frac{\mathrm{d}\ln P}{\mathrm{d}\ln\rho}\delta(\ln\rho) = \Gamma_1\frac{\delta\rho}{\rho}, \tag{1.36}$$

where Γ_1 is the first adiabatic index. The Eqs. 1.29, 1.31, 1.32 and 1.36 form the complete set of equations that we use when we study the adiabatic stellar oscillations.

1.3.2 Radial oscillations

The variations in the radial direction are well distinct from the variations in the horizontal direction, and so we can consider them separately. The most simple case of stellar oscillations are those that take place only in the radial direction. In order to study them, we consider that the spherical symmetry is maintained during the oscillation ($\delta\boldsymbol{r} = \delta r(r)\sin(\sigma t)$), with σ being the angular frequency, and by using that condition in Eqs. 1.29, 1.31 and 1.32, we can combine them into a Sturm-Liouville problem

$$\frac{\mathrm{d}}{\mathrm{d}r}\left(r^4\Gamma_1 P\frac{\mathrm{d}}{\mathrm{d}r}\left(\frac{\delta r}{r}\right)\right) + \left[r^3\frac{\mathrm{d}}{\mathrm{d}r}((3\Gamma_1 - 4)P) + \sigma^2\rho r^4\right]\frac{\delta r}{r} = 0, \tag{1.37}$$

in which we can replace $\frac{\delta r}{r} = \xi$, which is the displacement vector and also the eigenmodes of the problem. The two boundary conditions are, that the pressure must be equal to zero ($P(0) = P(R) = 0$), at the center of the star and at its surface. That problem has some very important properties:

1. The eigenmodes are orthonormal to each other. That means that, for two eigenmodes ξ_1 and ξ_2, we have that $\langle \xi_1 \mid \xi_2\rangle = \int_0^M \delta r_1 \delta r_2 \mathrm{d}m = 0$.
2. We have a countable set of frequencies that tends to infinity $\sigma_0^2 < \sigma_1^2 < ... < \sigma_n^2 \to \infty$, where n is the radial order, corresponding to the number of modes of the eigenfunctions.
3. The eigenmodes form a complete base.
4. There exists a variational principle that allows us to compute small variations in the eigenfrequencies, from small perturbations in the stellar structure.
5. The eigenfunction modes are interweaved. That is, the modes of ξ_{n+1} are located between those of ξ_n

1.3.3 Non-radial oscillations

For the previous discussion we considered only the radial oscillations. Nevertheless, those oscillations are the simplest ones, and they are only a subcategory of the general case, which is about oscillations that are also occuring in the horizontal (non-radial) direction. For that reason, we will take into consideration the other two coordinates of the spherical set (θ, ϕ), for the oscillations in the horizontal direction. In order to treat the whole system, we can use the method of variable separation, to separate the spatial from the temporal coordinates, and so we get

$$P' = P'(r,\theta,\phi)e^{i\sigma t}, \tag{1.38}$$

and the displacement vector is

$$\delta\boldsymbol{r} = \xi_r\hat{e}_r + \xi_\theta\hat{e}_\theta + \xi_\phi\hat{e}_\phi = \delta\boldsymbol{r}(r,\theta,\phi)\sin(\sigma t). \tag{1.39}$$

By replacing the previous expression in the equation for the conservation of momentum (Eq. 1.31), we get

$$\sigma^2\xi_r = \frac{\partial\psi'}{\partial r} + \frac{\rho'}{\rho}\frac{Gm}{r^2} + \frac{1}{\rho}\frac{\partial P'}{\partial r}, \tag{1.40}$$

$$\sigma^2\xi_\theta = \frac{1}{r}\frac{\partial}{\partial\theta}\left(\psi' + \frac{P'}{\rho}\right), \tag{1.41}$$

$$\sigma^2 \xi_\phi = \frac{1}{r \sin\theta} \frac{\partial}{\partial \phi} \left(\psi' + \frac{P'}{\rho} \right). \tag{1.42}$$

For the mass conservation equation (Eq. 1.29) we get

$$\frac{\delta\rho}{\rho} + \left[\frac{1}{r^2} \frac{\partial}{\partial r} (r^2 \xi_r) + \frac{1}{r \sin\theta} \frac{\partial}{\partial \theta} (\sin\theta \xi_\theta) + \frac{1}{r \sin\theta} \frac{\partial \xi_\phi}{\partial \phi} \right] = 0. \tag{1.43}$$

We can now combine the equations for the horizontal motion (Eqs. 1.41 and 1.42), with Eq. 1.43, and we have

$$\frac{\delta\rho}{\rho} + \frac{1}{r^2} \frac{\partial}{\partial r} (r^2 \xi_r) - \frac{1}{\sigma^2 r^2} \mathcal{L}^2 \left(\psi' + \frac{P'}{\rho} \right) = 0, \tag{1.44}$$

where $\mathcal{L}$

$$\mathcal{L} = -r^2 \nabla_h^2 = -\frac{1}{\sin\theta} \frac{\partial}{\partial \theta} \left(\sin\theta \frac{\partial}{\partial \theta} - \frac{1}{\sin^2\theta} \frac{\partial^2}{\partial \phi^2} \right), \tag{1.45}$$

is the Legendrian operator and h stands for the horizontal component of any vector.

The Poisson equation (Eq. 1.32) becomes

$$\nabla^2 \psi' = \frac{1}{r^2} \frac{\partial}{\partial r} \left(r^2 \frac{\partial \psi'}{\partial r} \right) - \frac{1}{r^2} \mathcal{L}^2 \psi' = 4\pi G \rho'. \tag{1.46}$$

Eqs. 1.40, 1.44 and 1.46 form the set of equations that we need to solve for the case of non-radial adiabatic stellar oscillations. In order to solve it, we use the method of variable separation, in which we can search for solutions of the form

$$X'(r, \theta, \phi) = X'(r) F(\theta, \phi). \tag{1.47}$$

This can be done because $\partial/\partial\theta$ and $\partial/\partial\phi$ appear only in the operator $\mathcal{L}^2$. The eigenfunctions of $\mathcal{L}$ are the spherical harmonics $Y_l^m(\theta, \phi)$ and so we get

$$\mathcal{L}^2 Y_l^m(\theta, \phi) = l(l+1) Y_l^m(\theta, \phi), \tag{1.48}$$

and by replacing that into 1.47 we have solutions of the form

$$X'(r, \theta, \phi) = X'(r) Y_l^m(\theta, \phi). \tag{1.49}$$

The spherical harmonics are given by

$$Y_l^m(\theta, \phi) = N P_l^{|m|} \cos(\theta) e^{im\phi}, \tag{1.50}$$

where $P_l^{|m|}$ corresponds to the Legendre polynomial, θ is the angular distance from the polar axis, or else co-latitude, ϕ is the longitude, and N is a normalization constant. l is called the spherical degree of the mode and gives the total horizontal number of nodes, and the azimuthal order m is the number of nodes along the equator. In the nodes, the amplitude of the oscillation is zero and, on its one side is positive, with the material moving outwards and, on its other side is negative, with the material moving inwards. This is represented in figure 1.1. In that figure, are represented a few spherical harmonics, with contour plots, for different sets of l and m. The positive contours, showed by continuous lines, correspond to material that moves outwards, and the negative contours, showed by dashed lines, to material that moves inwards.

The set of three equations that we use (Eqs. 1.40, 1.44, and 1.46), contains 4 unknowns (ρ', P', ξ_r', and ψ'). In order to solve it, we can eliminate ρ' by using the adiabatic relation, Eq. 1.36 and now we get for the radial motion (Eq. 1.40)

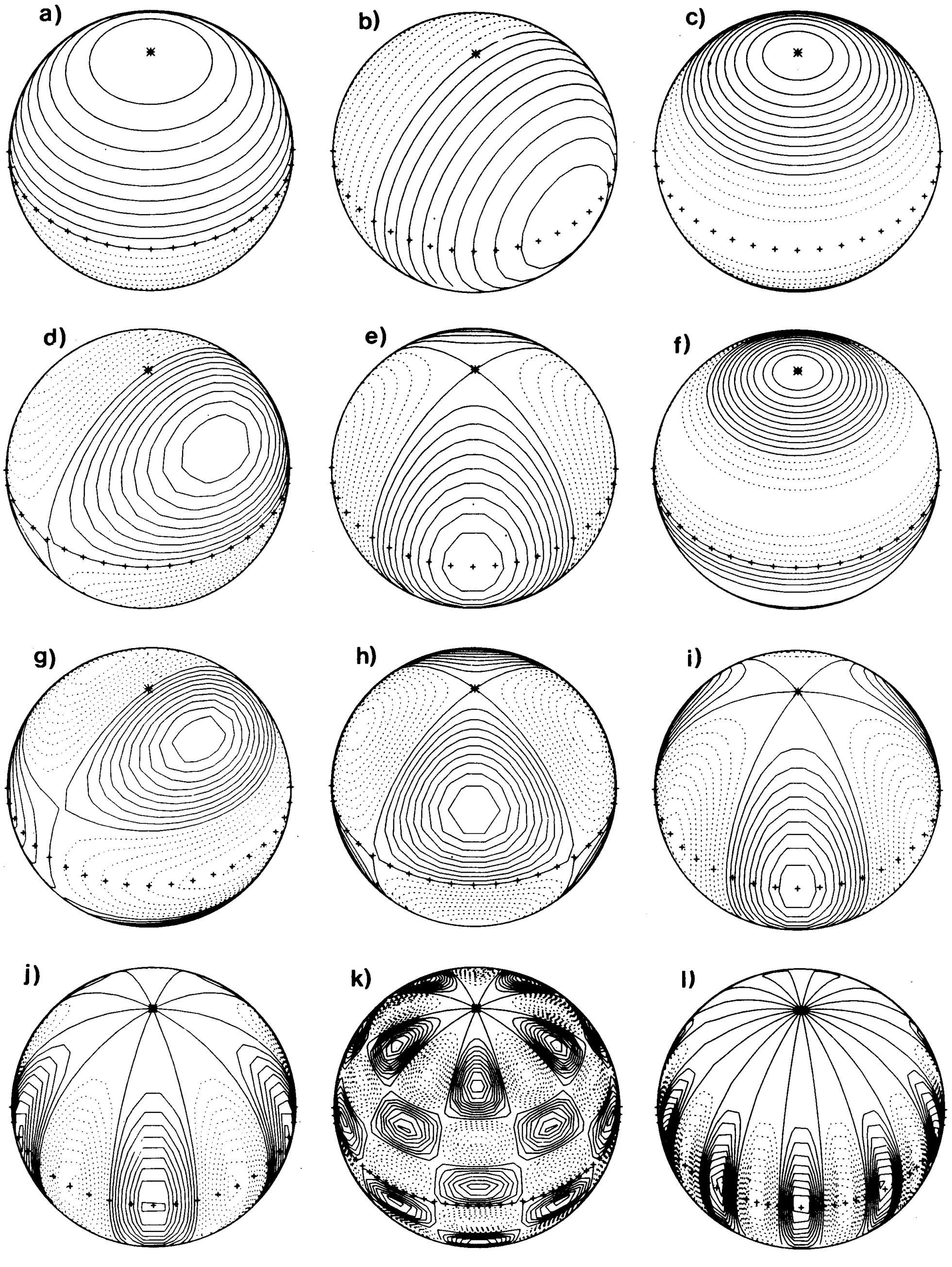

Figure 1.1: The representation of the real part of spherical harmonics Y_l^m. The continuous lines are for positive contours while the dashed lines are for negative contours. The line showed by the '+++' symbols, represents the equator and the pole is indicated by the star. The cases that are shown here are: a) $l = 1$, $m = 0$, b) $l = 1$, $m = 1$, c) $l = 2$, $m = 0$, d) $l = 2$, $m = 1$, e) $l = 2$, $m = 2$, f) $l = 3$, $m = 0$, g) $l = 3$, $m = 1$, h) $l = 3$, $m = 2$, i) $l = 3$, $m = 3$, j) $l = 5$, $m = 5$, k) $l = 10$, $m = 5$, and l) $l = 10$, $m = 10$.

$$\frac{\mathrm{d}P'}{\mathrm{d}r} = \rho\frac{d\psi'}{\mathrm{d}r} + \frac{g}{c^2}P' = (\sigma^2 - N^2)\rho\xi_r, \tag{1.51}$$

for the expression of the horizontal motion (Eq. 1.44), and the mass conservation (Eq. 1.43)

$$\frac{P'}{\rho c^2}\left(1 - \frac{L_l^2}{\sigma^2}\right) - \frac{l(l+1)}{\sigma^2 r^2}\psi' - \frac{g}{c^2}\xi_r + \frac{1}{r^2}\frac{\mathrm{d}}{\mathrm{d}r}(r^2\xi_r) = 0, \tag{1.52}$$

and for the Poisson equation

$$\frac{1}{r^2}\frac{\mathrm{d}}{\mathrm{d}r}\left(r^2\frac{\mathrm{d}\psi'}{\mathrm{d}r}\right) - \frac{l(l+1)}{r^2}\psi' = 4\pi G\rho', \tag{1.53}$$

where we introduced the squared Brunt-Väisälä or buoyancy frequency

$$N^2 = \frac{Gm}{r^2}\left(\frac{1}{\Gamma_1}\frac{\mathrm{d}\ln P}{\mathrm{d}r} - \frac{\mathrm{d}\ln\rho}{\mathrm{d}r}\right), \tag{1.54}$$

and the squared Lamb frequency

$$L_l^2 = \frac{l(l+1)c^2}{r^2}. \tag{1.55}$$

Eq. 1.54 is a measure of the Ledoux criterion, for convective instability. The Ledoux criterion, named after the famous Liège astrophysicist, Paul Ledoux, takes into consideration the modification of the chemical composition, due to several processes (microscopic diffusion, nuclear reactions,...), in the treatment of the equations. Those processes create chemical stratification in the radiative zones. It is given by:

$$\nabla_{\mathrm{rad}} - \frac{\phi}{\delta}\nabla_\mu = \nabla_{\mathrm{ad}}, \tag{1.56}$$

where μ is the molecular weight, $\phi = \frac{\partial\ln\rho}{\partial\ln\mu}\Big|_{\mathrm{P,T}}$, $\delta = -\frac{\partial\ln\rho}{\partial\ln T}\Big|_{\mathrm{P},\mu}$ and $\nabla_\mu = \frac{\mathrm{d}\ln\mu}{\mathrm{d}\ln P}\Big|_{\mathrm{m}}$. We can understand this criterion like that. We consider a region where the molecular weight decreases upwards, which is the most common case. If in that region, a parcel of matter starts moving upwards, it will reach an area where the molecular weight is lower. If the temperature and pressure do not change, it will be denser than the surrounding matter, and so, it will be pushed downwards, by the Archimedes force. If an area is stable with respect to the Ledoux criterion, but unstable with respect to the Schwarzchild criterion, the parcel of matter will be forced in an oscillatory motion, with frequency given by Eq. 1.54. This induces a slow mixing of the stellar material, which is referred to as semi-convection.

Mathematically we can think Eq. 1.54 like this. The term outside the parenthesis, Gm/r^2, and $1/\Gamma_1$ are always positive and so the sign of N^2 is defined by the values of $\mathrm{d}\ln P/\mathrm{d}r$ and of $\mathrm{d}\ln\rho/\mathrm{d}r$, that are the indicators of the stratification of pressure and of density respectively. When $N^2 > 0$, the parcel is heavier than its surroundings which means that, due to buoyancy (Archimedes force), it is pushed back to its original position, and this corresponds to convective stability. On the other hand, when $N^2 < 0$ the parcel is lighter than its surroundings and so buoyancy will make it continue moving upwards, which corresponds to convective instability. In the first case, the parcel will be forced to an oscillatory motion around the equilibrium position, while, on the second case, the parcel will be permanently pushed away from it. From the form of Eq. 1.54 we can get

$$\frac{\mathrm{d}\ln\rho}{\mathrm{d}\ln P} > \frac{1}{\Gamma_1}, \tag{1.57}$$

as an alternative condition for the $N^2 > 0$ case. We see that Eq. 1.55 is directly linked to the spherical degree of the mode, and to the $c = \sqrt{\Gamma_1\frac{P}{\rho}}$, which is the sound speed in the plasma. The restoring force for the waves that is characteristic of p-modes, is the pressure gradient that the plasma exerts on the parcel, and so they are called *pressure waves* or *p-modes*.

By combining the equations of conservation of momentun in the horizontal direction, Eqs. 1.41 and 1.42, with the equation for the variable separation, Eq. 1.49, we can get for the horizontal components of the displacement vector:

$$\xi_\theta = \frac{1}{\sigma^2 r}\left(\psi^2 + \frac{P'}{\rho}\right)\frac{\partial Y_l^m(\theta,\phi)}{\partial\theta}, \tag{1.58}$$

$$\xi_\phi = \frac{1}{\sigma^2 r}\left(\psi^2 + \frac{P'}{\rho}\right)\frac{1}{\sin\theta}\frac{\partial Y_l^m(\theta,\phi)}{\partial\theta}, \tag{1.59}$$

and by defining

$$\xi_h = \frac{1}{\sigma^2 r}\left(\psi' + \frac{P'}{\rho}\right), \tag{1.60}$$

we get for the displacement vector

$$\xi' = \xi_r(r) Y_l^m(\theta,\phi)\boldsymbol{e}_r + \xi_h(r)\left(\frac{\partial Y_l^m(\theta,\phi)}{\partial\theta}\boldsymbol{e}_\theta + \frac{1}{\sin\theta}\frac{\partial Y_l^m(\theta,\phi)}{\partial\phi}\boldsymbol{e}_\phi\right), \tag{1.61}$$

and for the continuity equation

$$\frac{\delta\rho}{\rho} + \frac{1}{r^2}\frac{\mathrm{d}}{\mathrm{d}r}(r^2\xi_r) - l(l+1)\frac{\xi_h}{r} = 0. \tag{1.62}$$

1.3.3.1 The Cowling approximation and propagation cavities

The Poisson equation (Eq. 1.7) for the gravitational potential can be written in integral form as

$$\psi'(\boldsymbol{r},t) = -G\int_V \frac{\rho(\boldsymbol{r}',t)\mathrm{d}V}{|\boldsymbol{r}-\boldsymbol{r}'|}, \tag{1.63}$$

which can also be written in the form

$$\psi'(\boldsymbol{r}) = \frac{4\pi G}{2l+1}\left[\frac{1}{r^{l+1}}\int_0^r \rho'(\boldsymbol{r}')r'^{l+2}\mathrm{d}r' + r^l\int_r^R \frac{\rho'(\boldsymbol{r}')}{r'^{l+1}}\mathrm{d}r'\right], \tag{1.64}$$

from which we take that in some cases we can neglect the perturbation to the gravitational potential ($\psi' \ll$). Those cases are when

1. the spherical degree l is large or
2. the radial order n is large

Usually the radial order n is much larger than the spherical degree l, and so we can take that ψ'=0, according to the Cowling approximation, and further simplify the equations to make them an eigenvalue problem of second order

$$\frac{\mathrm{d}P'}{\mathrm{d}r} + \frac{g}{c^2}P' = (\sigma^2 - N^2)\rho\xi_r, \tag{1.65}$$

$$\frac{P'}{\rho c^2}\left(1 - \frac{L_l^2}{\sigma^2}\right) - \frac{g}{c^2}\xi_r + \frac{1}{r^2}\frac{\mathrm{d}}{\mathrm{d}r}\left(r^2\xi_r\right) = 0. \tag{1.66}$$

In addition, when the number of eigenmodes is large we get that

$$\frac{dP'}{dr} \simeq (\sigma^2 - N^2)\rho\xi_r, \tag{1.67}$$

which gives us

$$\frac{P'}{\rho c^2}\left(1 - \frac{L_l^2}{\sigma^2}\right) + \frac{d\xi_r}{dr} = 0, \tag{1.68}$$

and, by deriving Eq. 1.68, with respect to r, and combining it with Eq. 1.67 we get:

$$\frac{\mathrm{d}^2\xi_r}{\mathrm{d}r^2} \simeq -\frac{\mathrm{d}}{\mathrm{d}r}\left\{\left(1 - \frac{L_l^2}{\sigma^2}\right)\frac{P'}{\rho c^2}\right\} \simeq -\left(1 - \frac{L_l^2}{\sigma^2}\right)\frac{1}{\rho c^2}\frac{\mathrm{d}P'}{\mathrm{d}r} \simeq -\frac{1}{c^2}\left(1 - \frac{L_l^2}{\sigma^2}\right)(\sigma^2 - N^2)\xi_r. \tag{1.69}$$

From that we write

$$\frac{\mathrm{d}^2\xi_r}{\mathrm{d}r^2} + k^2(r)\xi_r \simeq 0, \tag{1.70}$$

where k is the *wavenumber* and is equal to

$$k^2(r) = \frac{1}{c^2}\left(1 - \frac{L_l^2}{\sigma^2}\right)(\sigma^2 - N^2). \tag{1.71}$$

The above expression is very important because it provides the conditions for the wave propagation. If $k^2 > 0$, the wave can propagate and we can observe a mode, while if $k^2 < 0$ we have an evanescent zone and the wave cannot propagate. So, in order to have a positive k^2, and taking into consideration that $1/c^2$ and σ^2 are always positive, we must have that

1. $\sigma^2 > L_l^2, N^2$ or
2. $\sigma^2 < L_l^2, N^2$

In the former case we have the propagation of pressure modes and, in the latter we have the propagation of gravity modes. This is clearly illustrated in Fig. 1.2, where we see the regions of propagation for the two different modes, in the case of the Sun.

In the JWKB approximation we get the asymptotic solution

$$\bar{\xi}_r(r) \simeq \frac{A}{k(r)^{1/2}}\cos\left(\int^r k(r)\mathrm{d}r\right). \tag{1.72}$$

If, on the other hand, the square of the frequencies (σ^2) is larger than one of the aforementioned frequencies, but smaller than the other, then we have an evanescent zone, and the wave amplitude varies exponentially. The asymptotic solution is given by

$$\bar{\xi}_r(r) \simeq \frac{A}{k(r)^{1/2}}\exp\left(\int^r k(r)\mathrm{d}r\right). \tag{1.73}$$

In the limiting case where $\sigma^2 \gg N^2$, L_l^2, we can simplify Eq. 1.71 for the p-modes

$$k^2(r) \simeq \frac{\sigma}{c}\left(1 - \frac{L_l^2}{\sigma^2}\right) \simeq \frac{\sigma^2}{c^2}, \tag{1.74}$$

and Eq. 1.70 becomes a Sturm-Liouville problem of the form

$$\frac{\mathrm{d}^2\xi_r}{\mathrm{d}r^2} + k^2 f(r)\xi_r = 0, \tag{1.75}$$

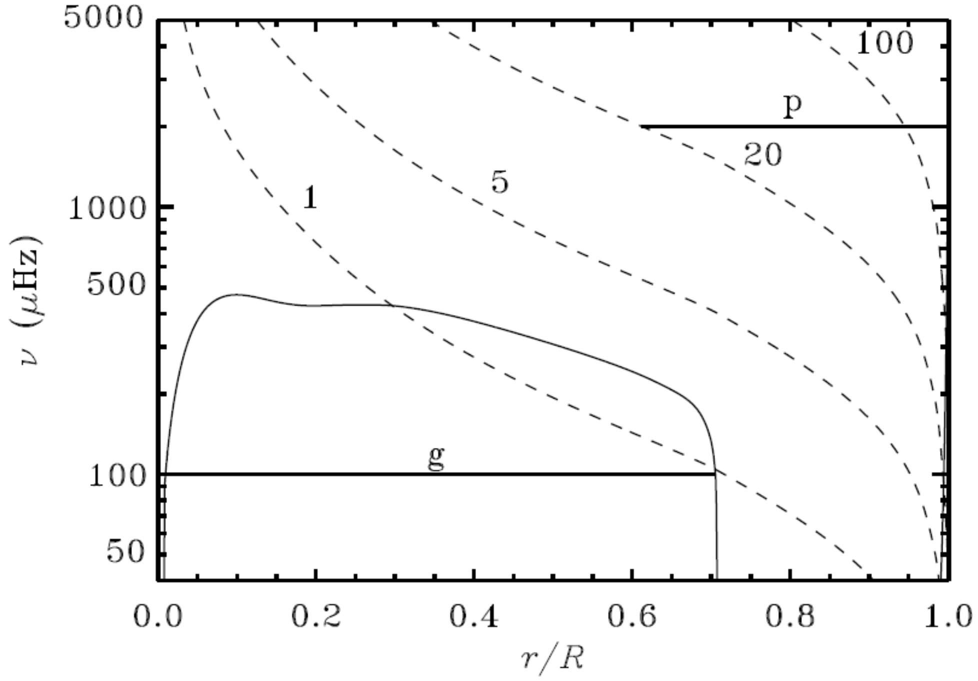

Figure 1.2: The propagation and evanescent cavities for the case of the Sun. In this plot, the frequencies ν, measured in μHz, are shown as a function of the normalized radius. The dashed lines correspond to p-modes, of different spherical degree l, which is shown by the number, next to the line. The p-modes can only propagate in the region on the right of that line, and so they are trapped between the surface and the turning point. The continuous, curved line corresponds to the region where the g-modes can propagate. We see that, for solar-like stars the g-modes cannot reach the surface.

where the solutions of that problem are the squared eigenvalues σ^2. There is an infinite number of solutions and they tend to infinity for increasing spherical degree.

In that limiting case ($\sigma^2 \gg N^2$, L_l^2), we finally have for the pressure modes that the wave relation is

$$\frac{\mathrm{d}^2\xi_r}{\mathrm{d}r^2} + \frac{\sigma^2}{c^2(r)}\xi_r \simeq 0, \tag{1.76}$$

which is the the same as for the acoustic waves in the organ pipe (see section 1.3.4). We thus understand that the pressure modes in stars are comparable to acoustic standing waves. As in the atmosphere of the Earth, the gas is compressed in some points and the pressure gradient is the restoring force that produces those waves. The sound speed profile is given by

$$c^2 = \frac{\Gamma_1 P}{\rho} \propto \frac{\Gamma_1 T}{\mu}, \tag{1.77}$$

for the case of a perfect gas, for the second equality. It is important to note that, the first equality is always valid by definition. Because of c^2 in Eq. 1.76, the eigenfrequencies (σ^2) are directly related to c^2. So, measuring σ^2 ,allows asteroseismology to probe the sound speed profile. We need enough modes, so that we can get profiles, but usually we have bulk properties.

For the limiting case of the $\sigma^2 \ll N^2, L_l^2$ we get for the gravity modes that

$$k^2 = \frac{N^2 L_l^2}{\sigma^2 c^2} = \frac{l(l+1)N^2}{\sigma^2 r^2}, \tag{1.78}$$

and Eq. 1.70 becomes a Sturm-Liouville problem of the form

$$\frac{\mathrm{d}^2\xi_r}{\mathrm{d}r^2} + \frac{g(r)}{\sigma^2}\xi_r = 0, \tag{1.79}$$

where the solutions of that problem are the negative squared eigenvalues σ^{-2}. Those solutions are infinite and they tend to zero for increasing spherical degree.

For the case of $l \geq 2$, between the frequencies of the gravity and pressure modes, there is the fundamental mode (f).

1.3.4 Semi-open organ pipe

One simple example that helps to better understand the previous set of equations, is the case of the semi-open organ pipe. In that case we can consider the medium to be homogeneous and, by taking into consideration the Cowling approximation, see section 1.3.3.1, we have that $\nabla P = \nabla\rho = \nabla\Gamma_1 = \nabla\psi = 0$. So we can write $\delta P = P'$, $\delta\rho = \rho'$. By applying that in the previous equations we get for the mass conservation equation (Eq. 1.29)

$$\frac{\rho'}{\rho} = -\nabla \cdot \delta\boldsymbol{r}, \tag{1.80}$$

for the momentum conservation equation (Eq. 1.31)

$$\frac{\partial^2 \delta\boldsymbol{r}}{\partial t^2} = -\frac{\nabla P'}{\rho}, \tag{1.81}$$

and for the adiabatic relation (Eq. 1.36)

$$\frac{P'}{P} = \Gamma_1 \frac{\rho'}{\rho}. \tag{1.82}$$

In order to find the behavior of the gas in the perturbed case, we calculate the divergence of the momentum equation (Eq. 1.81) and use Eqs. 1.80 and 1.82

$$\nabla \cdot \frac{\partial^2 \delta \boldsymbol{r}}{\partial t^2} = \frac{\partial^2 \nabla \cdot \delta \boldsymbol{r}}{\partial t^2} = -\frac{\partial^2 (\rho'/\rho)}{\partial t^2} = -\frac{1}{\Gamma_1 P}\frac{\partial^2 P'}{\partial t^2} = -\frac{\nabla^2 P'}{\rho}, \tag{1.83}$$

from which we get the wave equation

$$\frac{\partial^2 P'}{\partial t^2} = c^2 \nabla^2 P', \tag{1.84}$$

and so we see, that the stellar oscillations can also be due to acoustic sound waves. We can understand that, by thinking the stars as resonators, that reflect the acoustic waves in their interior. That has the consequence to let only waves with specific frequencies to propagate in their interior, while cancelling all the other waves. The quantities that appear in the equations like density ($\rho(\boldsymbol{r}, t)$), and pressure ($P(\boldsymbol{r}, t)$), depend only on their radial coordinate (r), and so we can separate those two variables and write the dependence on time as $e^{i\sigma t}$, where σ is the angular angular frequency and is connected to the linear frequency by

$$\sigma = 2\pi\nu. \tag{1.85}$$

The solution to the wave equation (Eq. 1.84) is given by

$$P'(\boldsymbol{r}, t) = P'(\boldsymbol{r})e^{i\sigma t} = P'(\boldsymbol{r})(i\cos(\sigma t)) + \sin(\sigma t) = \sin(\sigma t)P'(\boldsymbol{r}), \tag{1.86}$$

in which we kept the real part of the equation and, by replacing in Eq. 1.84, we get

$$\sigma^2 P' + c^2 \nabla^2 P' = 0. \tag{1.87}$$

The problem has become an eigenvalue problem of the form

$$A\boldsymbol{x} = \sigma^2 \boldsymbol{x}, \tag{1.88}$$

where σ^2 is the requested eigenvalue, $A = -c^2\nabla^2$ is a linear operator, and $\boldsymbol{x} = P'$ is the eigenfunction. To solve that, we will also need some boundary conditions that we will see in a while.

We assume that the semi-open organ pipe has lenght R, and that the distance increases from the closed edge. The maximum displacement that a parcel would get, is the length of the pipe. Since we are talking about standing waves, there must be no pressure difference in the closed edge of the pipe and, in the open edge, the pressure perturbation should be zero, since it comes in contact with the environment. That gives us the two boundary conditions that we need in order to solve the wave equation (Eq. 1.84)

$$\left.\frac{\mathrm{d}P'}{\mathrm{d}r}\right|_{r=0} = P'(R) = 0, \tag{1.89}$$

and, if we consider the sound speed to be constant in all the medium, then the solution takes the form

$$P'(r, t) = A\sin(\sigma t)\cos\left(\frac{\sigma r}{t}\right). \tag{1.90}$$

The second boundary condition is satisfied only when the cosine reaches zero, and this happens when its argument is half multiples of π. This corresponds to

$$\frac{\sigma R}{c} = \pi\left(\frac{1}{2} + n\right) \Rightarrow \frac{\sigma}{2\pi} = \nu = \frac{c}{2R}\left(\frac{1}{2} + n\right), \tag{1.91}$$

where n is positive inreger, and corresponds to the number of nodes of the stationary wave. In the stars, it corresponds to the number of nodes in the radial direction, and is called the radial order. For acoustic waves, which we study, it takes positive values. We can define, for two consecutive frequencies, the large separation

$$\Delta\nu = \nu_n - \nu_{n-1} = \frac{1}{2}\frac{c}{R}, \tag{1.92}$$

From that we have the important conclusion of the equidistance of frequencies of the same spherical degree, with consecutive radial orders.

In that analysis, we considered that the sound speed (c), remains constant in the medium. Nevertheless, we know that c depends on the density and on the temperature of the medium in which it propagates, and those quantities vary in the stellar interior. When we consider that c varies with the distance from the center ($c(r)$), we can treat the wave equation (Eq. 1.84) through the JWKB approximation. In the general case we can write the wave equation as

$$\frac{\mathrm{d}^2u}{\mathrm{d}x^2} + k(x)^2u = 0, \tag{1.93}$$

and the solution is, under the JWKB approximation, assuming the solutions to be plane waves,

$$u(x) = k(x)^{1/2}\cos\left(\int_0^x k(x)\mathrm{d}x\right), \tag{1.94}$$

which, in our case, is

$$P'(r) \simeq Ac(r)^{1/2}\cos\left(\sigma\int_0^r \frac{\mathrm{d}r}{c}\right). \tag{1.95}$$

From the boundary condition requiring that P'(R) = 0, we get that the argument of the cosine must be half multiples of π. That gives us

$$\sigma\int_0^R \frac{\mathrm{d}r}{c} = \pi\left(\frac{1}{2}+n\right) \Rightarrow \frac{\sigma}{2\pi} = \nu = \frac{1}{2}\left(\frac{1}{2}+n\right)\left(\int_0^R \frac{\mathrm{d}r}{c}\right)^{-1}, \tag{1.96}$$

from which we can define the large separation $\Delta\nu$ as in the case of constant c as

$$\Delta\nu = \left(2\int_0^R \frac{dr}{c}\right)^{-1}. \tag{1.97}$$

From that, we get that the frequencies are equidistant for large n, and this defines the asymptotic regime of the frequencies. The quantity $\int_0^R \frac{\mathrm{d}r}{c}$ is called the *acoustic radius*, and is a measure of the time that the wave would need, in order to propagate from the center of the star to the surface.

1.4 Solar-like stars

The method that we propose in our work is for solar-like stars. In that section we present the structure and oscillatory characteristics of those stars.

1.4.1 Internal Structure

When we are talking about solar-like stars, we talk about stars that are of approximatelly the same mass as the Sun ($\pm 0.2M_\odot$) and which are also in the same evolutionary stage, the main sequence. With such a mass, those stars are considered to be of low- to intermediate- mass stars. As they are in the main sequence, they produce their energy by fusing hydrogen in their core to produce mainly helium nuclei and energy, as it is shown in appendix A. The energy that is produced by those reactions is equal to the energy that is radiated by the star (luminosity). The main-sequence stars are located in a long, diagonal strip in the Hertzsprung-Russel (HR) diagram, from the top left to the bottom

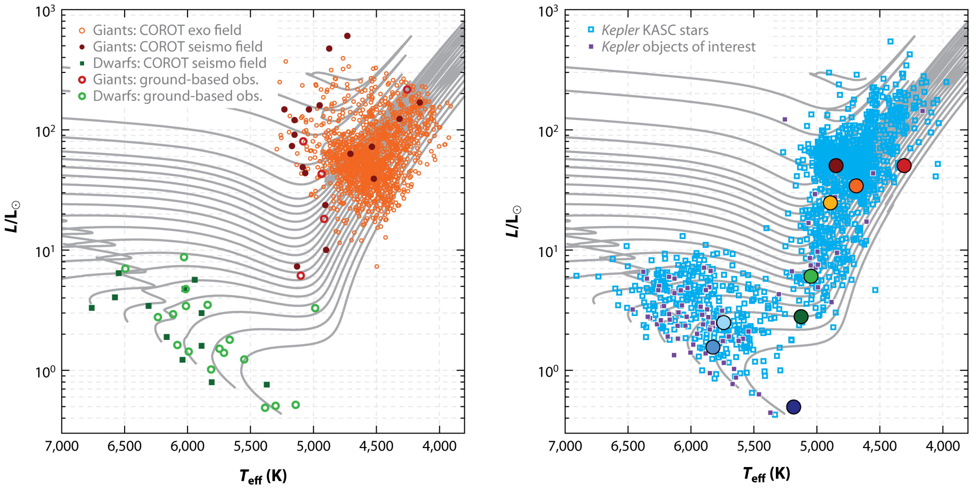

Figure 1.3: The stars that are observed by CoRoT (Baglin et al. 2009), on the left plot, and by *Kepler* (Borucki et al. 2010), on the right plot, from Chaplin & Miglio (2013). We can easily distinguish between the main-sequence stars, on the bottom left of the plots, from the giants, on the top right.

right. This phase is the longest one in their life. In that stage they are in hydrostatic equilibrium which means that they neither collapse nor explode.

We show in Fig. 1.3 HR plots ($L/L_\odot$ as a function of $T_{\rm eff}0$, of the CoRoT (Baglin et al. 2009), on the left plot, and of the *Kepler* (Borucki et al. 2010), on the right plot, from Chaplin & Miglio (2013). In the left plot we see that we have asteroseismic data for giant stars, in addition to the main-sequence stars, that we are interested in our study. We see that the main-sequence stars are located in a diagonal strip, at the bottom left of the plots, while the giant stars are located in the giant branch, at the top right of the plots. Also, it is obvious from those plots, the large amount of data that those missions provide.

In main-sequence stars, the energy is produced only in their cores where the thermonuclear reactions take place. This affects the structure of the whole star because that energy is transferred outwards, and is eventually radiated by its surface and its atmosphere. The core in solar-like stars is in most cases radiative, and they also have a convective envelope. In the case of the Sun, this envelope extends from about $0.7R_\odot$ up to the surface.

1.4.2 Solar-like oscillations

The Sun is the closest star to us and, for that reason, we can observe hundreds of thousands of modes. As we can see in Fig. 1.2, not all modes can propagate everywhere. In the case of the Sun, and of the solar-like stars, the gravity modes, for example, cannot propagate in the upper layers of the Sun. That means that there are propagation and evanescent cavities for the different kinds of modes. This is shown in Fig. 1.2, from Christensen-Dalsgaard (2003), where the frequencies are represented, in μHz, with respect to the normalized distance to the center. In that plot the curved continuous line depicts the Brunt-Väisälä frequency, Eq. 1.54, and so the possible range of frequencies and distances for which gravity modes can propagate. For higher frequencies, or higher distances than those included within that curve, the gravity modes are damped. The dashed lines depict the Lamb frequency, Eq. 1.55, for different spherical degrees, symbolized by the number. That means that they represent the lower limit of the propagation cavities, for the pressure modes. From that plot, we see that for the case of solar-like stars, the gravity modes are restricted to the interior of the star, up to a radius of about $0.7M_\odot$, and so, we cannot observe them. For the pressure modes on the other hand, they are trapped between the surface and a point in the staller interior.

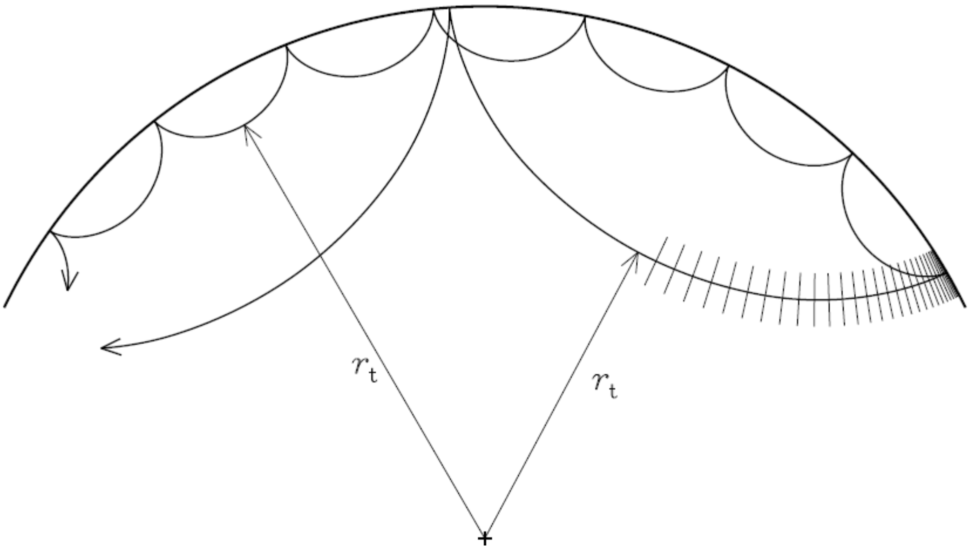

Figure 1.4: The pathways of two pressure modes of different spherical degrees.

The deepest point of the stellar interior that a pressure wave could reach, is called the turning point (r_t), and is directly linked to their spherical degree l, through the Lamb frequency, Eq. 1.55. It is called turning point because, when the wave reaches that point, it is reflected towards the outer regions of the star, until it arrives at the surface, where it is reflected again. This is better shown in Fig. 1.4 (Christensen-Dalsgaard 2003), where we see a schematization of the pathways of two pressure modes with $l = 30$, for the one that reaches deeper, and for $l = 100$ for the other one. We can understand how that turning point acts, by considering the waves as plane waves. As the plane wave travels inside the star, its deeper parts are located in an area with higher density and thus, the sound speed there is higher. As a result, they travel faster, and the direction of propagation shifts away from the radial direction. At the reflection point, the wave travels horizontally and then it travels towards the surface of the star. We see from that plot that the lower the spherical degree, the deeper in the star, the wave can go. This is very important because it means that waves of different spherical degrees, carry information about different layers.

When we work in the asymptotic regime, where $n \gg l$, Gough (1986) showed that the frequencies are approximated by

$$\nu = \left(n + \frac{l}{2} + \epsilon\right) \Delta\nu, \tag{1.98}$$

where $\Delta\nu$ is called the large separation and is the distance between two successive frequencies of the same spherical degree, and ϵ is a constant. In Fig. 1.5 (Christensen-Dalsgaard 2003), we show the power spectrum of the Sun, where the frequencies ν, in μHz, are shown in the abscissa, and in the ordinate is the power $P(\nu)$, in $cm^2 s^{-2} \mu Hz^{-1}$. The power spectrum is obtained by Fourier transforming the light curve, which allows us to get the frequencies. The lower panel is an expanded view of the central region of the upper panel. In those plots we can see that the majority of the observed solar frequencies are of the order of 5 minutes. From that plot, we can also see that the frequencies, in the case of solar-like stars, appear in groups, and that they are almost equidistant. Departures from that equidistance do exist and they are due to higher - order terms in Eq. 2.13. One example of such higher-order terms are the acoustic glitches, which we will discuss in the next chapter.

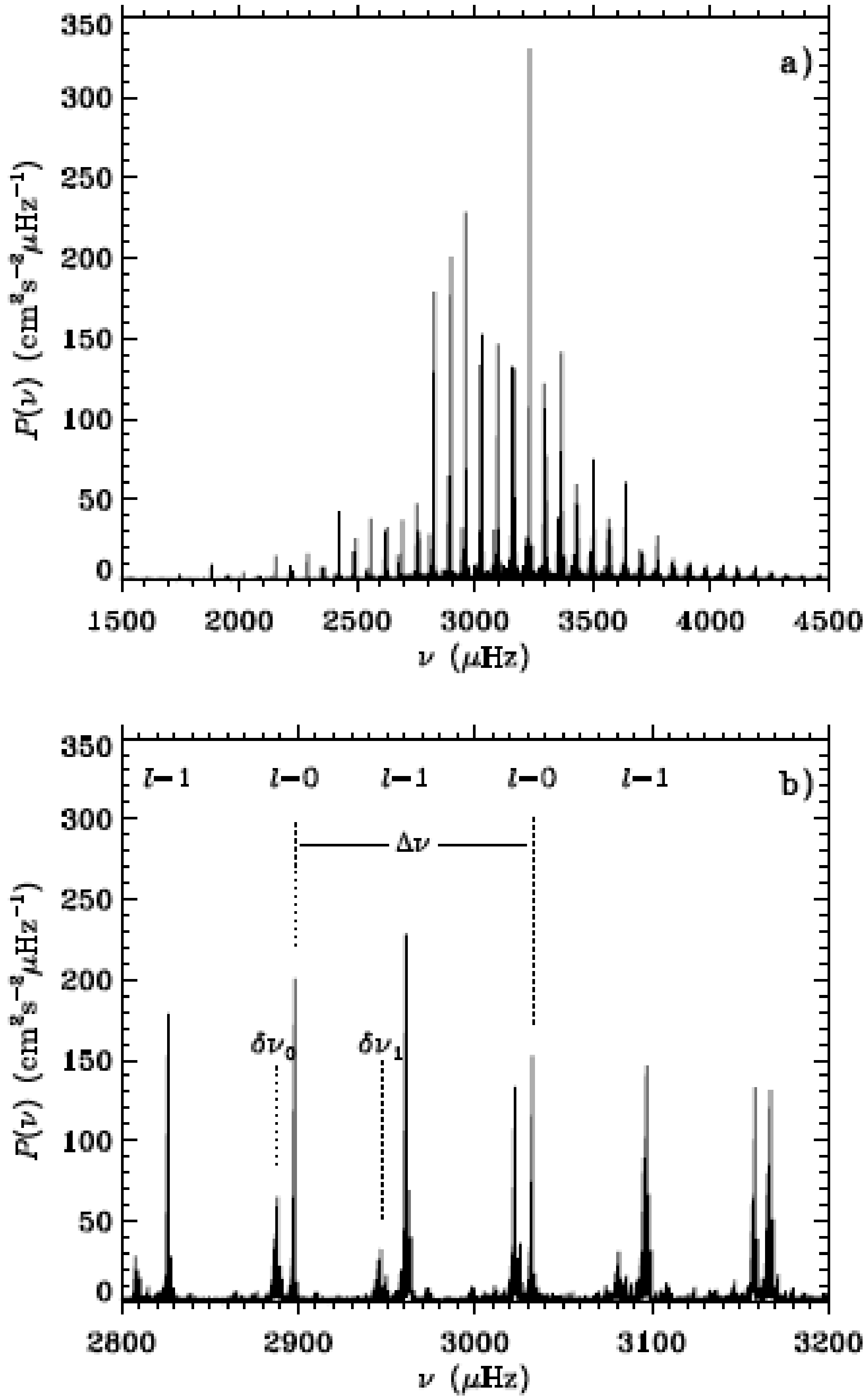

Figure 1.5: The power spectrum in the case of the Sun. The lower panel is an expanded view of the upper panel, where we can better see the equidistance of the frequencies ν, and that they appear in groups.

Chapter 2

The method for adjusting the glitches signature

The seismic data that are needed in order to constrain the internal structure of stars are obtained through observations, as in all other domains of astrophysics. However, to constrain the stellar structure, we measure small and periodic variations in the luminosity, which are of the order of one part per million. It is therefore obvious that those kind of observations were difficult to obtain, up to about a decade ago. Because of its short distance from Earth, which increases the precision of the observations, we could only retrieve quality data only for the Sun. The modes that could be observed were over a thousand, which helped us not only to put constrains on the characteristics of the internal structure of the Sun, but also to improve our theory of stellar evolution and to refine our models.

In asteroseismology, to derive precise asteroseismic diagnoses, extremely precise data is necessary. This justifies the need for space instruments, that evade the problems imposed by the Earth's atmosphere, like atmospheric seeing. Also, space intruments can take continuous observations for many weeks in a row since they are not interrupted by the day and night cycle which is a disadvantage of ground observations. In the recent years, with the advent of new space telescopes, such as the CoRoT (Baglin et al. 2009) and the *Kepler* (Borucki et al. 2010) missions, that have stopped operating, and the ongoing TESS (Ricker et al. 2014) space mission, that provided quality seismic data, the scientific community had the ability to apply asteroseismic techniques to stars other than the Sun. There is a variety of techniques that can be used in order to take advantage of those data. First of all, there is the approach that constrains the stellar models using the forward modelling by using individual oscillation frequencies, or by using frequency separations. Moreover, there are the inversion techniques that use frequencies, observed or modelled, in order to put tight constrains to the physical properties on the whole interior of the stars. Finally, there are some techniques that retrieve information about the stellar structure by taking into consideration the acoustic glitches as well.

The oscillation spectrum of solar-like stars can be divided into two parts. The smooth part, which varies slowly and can be described by the asymptotic theory of stellar oscillations, Eq. 2.13, and an oscillating part, the acoustic glitches. The acoustic glitches are faint signatures in the oscillation spectrum, which are caused by sharp variations in the stellar structure. By sharp variation we mean that those variations expand in much smaller spatial scales than the wavelength of the mode itself. The main two glitches that exist in solar-like stars are, firstly, due to the discontinuity of the temperature gradient in the transition region between the radiative and the convective zone (BCZ) and secondly, due to the second helium ionization zone. Both of them are located quite close to the stellar surface. The convection zone glitch helps to constrain the exact position of this area but also provides us with information about the mixing processes that affect the chemical profile around the bottom of that region (turbulent diffusion due to differential rotation, ...), and affect that position. Unfortunately, its signature is quite faint, in comparison to its uncertainty, in solar-like stars, and thus carries little information. For the latter, because of the helium ionization in the second He ionization zone, energy

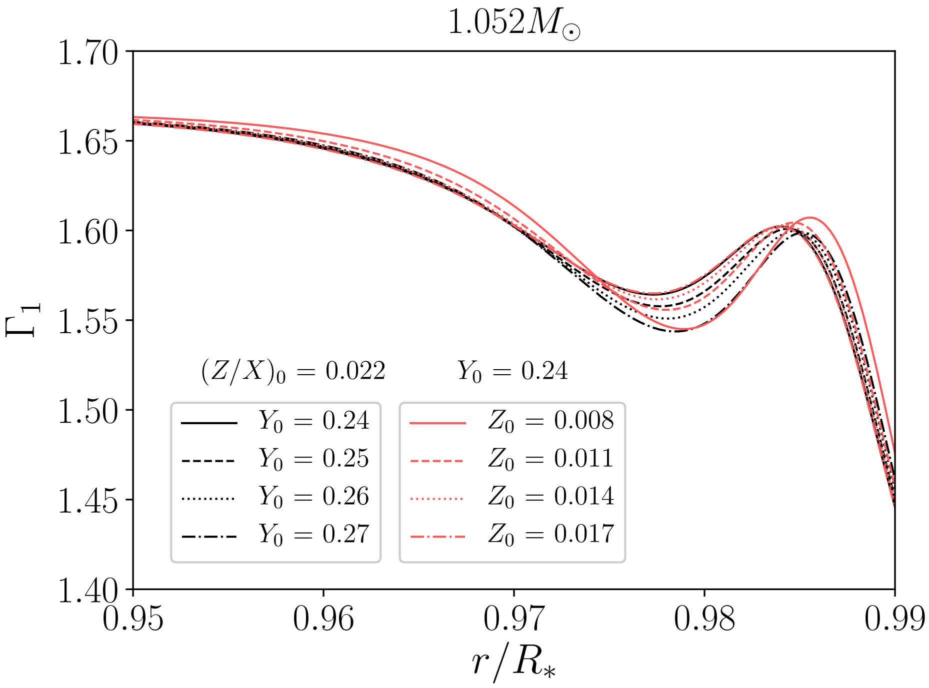

Figure 2.1: The Γ_1 profile, as a function of the reduces radius, near the stellar surface.

is absorbed and this causes the pressure P, and density ρ, to increase at different rates. As a result, the first adiabatic index ($\Gamma_1 = \frac{\partial \ln P}{\partial \ln \rho}\Big|_S$, where S is the entropy) experiences a depression in that region, which causes the helium acoustic glitch.

This is shown in Fig. 2.1. In that figure, from Farnir et al. (2019), we see the profile of the first adiabatic index, with respect to the normalized distance from the center, for a star with $M = 1.052M_\odot$. We see the aforementioned depression in Γ_1, for helium abundances with values of 0.24, 0.25, 0.26, and 0.27 and with an initial metallicity of $(Z/X)_0 = 0.022$, with the black curves. The red curves correspond to surface helium abundance of $Y_0 = 0.24$ and to initial metallicities $(Z/X)_0$ that vary and take values of 0.008, 0.011, 0.014, and 0.017. It is obvious from that figure that the higher the helium abundance, the deeper this depression gets, but also that the metallicity affects that depth in the oppossite way, making it shallower for higher values. That depth can help constrain the helium abundance in this region and, since it is so close to the surface, we can take it to be the surface helium abunbance. This is very important because the surface helium abundance cannot be constrained by other means, in main-sequence solar-like stars, like, for example, spectroscopy.

The use of data of high quality, as those provided by the aforementioned instruments, lead to the need for improving the existing techniques, so that we could benefit from all the information that they contain. Since we wanted to study the helium glitch, we used the **WhoSGlAd** (**Who**le **S**pectrum and **Gl**itches **Ad**justment), which makes a very efficient use of the helium glitch signature. The strength of this method lies in the fact that it makes use of both the smooth and the glitches parts simultaneously. It also combines the oscillation frequencies in a clever way to build seismic indicators as little correlated as possible and representative of the stellar structure.

2.1 Mathematical notations

In the subsequent sections of the present chapter, we describe the WhoSGlAd method following Farnir et al. (2019). The mathematical notations that we use are

1. A basis of vectors over a given N-dimensional Euclidean vector space is represented by curly brackets: $\{\boldsymbol{x}\} = \{\boldsymbol{x}_1 \dots \boldsymbol{x}_N\}$;
2. The scalar product of two vectors $\boldsymbol{x}$ and $\boldsymbol{y}$ is represented as: $\langle \boldsymbol{x} | \boldsymbol{y} \rangle$;
3. The norm of a vector is: $\parallel \boldsymbol{x} \parallel = \sqrt{\langle \boldsymbol{x} | \boldsymbol{x} \rangle}$;
4. The weighted mean of a vector is noted as: $\bar{\boldsymbol{x}}$.

Expressions for the scalar product and the weighted mean will be given when necessary.

2.2 Gram - Shmidt orthonormalisation

The WhoSGlAd method is based on the Gram-Schmidt orthonormalisation process. With this technique we can build an orthonormal basis from any given basis over a N dimensional Euclidean vector space. An orthonormal basis is a base of which the components are normal to each other and of unit length. By assuming that we have an ordinary basis of vectors $\{\boldsymbol{p}\} = \{\boldsymbol{p}_1 \dots \boldsymbol{p}_N\}$, we can build the orthonormal basis $\{\boldsymbol{q}\} = \{\boldsymbol{p}_1 \dots \boldsymbol{q}_N\}$ in the following way.

First, we normalise one of the vectors of our set

$$\boldsymbol{q}_1 = \frac{\boldsymbol{p}_1}{\parallel \boldsymbol{p}_1 \parallel}. \tag{2.1}$$

Then we build the basis by adding new elements one by one. To do so, we remove from each basis element $\boldsymbol{p}_i$, its projection on all the previously normalised basis elements $\sum_{j=1}^{i-1} \langle \boldsymbol{p}_i | \boldsymbol{q}_j \rangle \boldsymbol{q}_j$. This results in the orthogonal vector:

$$\boldsymbol{u}_i = \boldsymbol{p}_i - \sum_{j=1}^{i-1} \langle \boldsymbol{p}_i | \boldsymbol{q}_j \rangle \boldsymbol{q}_j. \tag{2.2}$$

This vector is not a unit vector however and the next step is to normalise it by

$$\boldsymbol{q}_i = \frac{\boldsymbol{u}_i}{\parallel \boldsymbol{u}_i \parallel}. \tag{2.3}$$

In a matrix form, we have

$$\boldsymbol{q}_i = \sum_{j=1}^{i} R_{i,j}^{-1} \boldsymbol{p}_j, \tag{2.4}$$

where $R_{i,j}^{-1}$ is the tranformation matrix for the i-th and j-th element between regular and orthonormal basis elements.

2.3 Adjustment and representation of the frequencies

When we presented earlier the mathematical expressions for the non-radial oscillations (section 1.3.3), we saw that they can be described by three integer numbers: the radial order n, the spherical degree l, and the azimuthal order m, which was set to 0, as we neglect rotation. This assumption is valid in most cases, since main-sequence solar-like stars are slow rotators. WhoSGlAd is based on linear algebra in an Euclidean vector space and that vector space is the set of N observed oscillation frequencies ν_i. Each observed frequency is associated with its standard deviation, σ_i. For two known frequency vectors, $\boldsymbol{x}$ and $\boldsymbol{y}$, we define their scalar product as

$$\langle \boldsymbol{x} | \boldsymbol{y} \rangle = \sum_{i=1}^{N} \frac{x_i y_i}{\sigma_i^2}. \tag{2.5}$$

It is useful in asteroseismology to compare two sets of frequencies, like for example the observed and the theoretical frequencies, by using a merit function which is defined as

$$\chi^2 = \sum_{i=1}^{N} \frac{(\nu_{obs,i} - \nu_{th,i})^2}{\sigma_i^2}, \tag{2.6}$$

where $\boldsymbol{\nu}_{th}$ are for the theoretical frequencies and $\boldsymbol{\nu}_{obs}$ are for the observed ones. We can use the scalar product that we defined before to represent it

$$\chi^2 = \|\boldsymbol{\nu}_{obs} - \boldsymbol{\nu}_{th}\|^2. \tag{2.7}$$

Houdek & Gough (2007) showed that, when there is a glitch, we can separate its oscillatory component from the smooth part of the spectrum. So, the frequencies are represented by separating the glitch contribution from that of the smooth part. The frequencies, both observed and theoretical, are projected over the vector basis elements and, from those projections, the seismic indicators are defined. From that comes that an orthonormal basis element over the vector sub-space is advantgeous and we acquire it by the Gram-Shmidt orthonormalization process (see section 2.2), associated with the definition of the scalar product (Eq. 2.5). By defining j and j_0 to be the indices that are related to the basis elements, $\boldsymbol{p}_j$ to be the former basis elements, $\boldsymbol{q}_{j_0}$ to be the orthonormal basis elements and R^{-1}_{j,j_0} to be the transformation matrix we get:

$$q_{j_0,l}(n) = \sum_{j \leq j_0} R^{-1}_{j,j_0} p_{j,l}(n), \tag{2.8}$$

where the appearence of n and l means that the basis elements are evaluated at each observed value of the radial order n and they have different values for each spherical degree l. The projections are done in such a way that the value of the merit function (Eq. 2.6) is minimum. The projection of the fitted coefficents over the basis elements is written as $a_j = \langle \boldsymbol{\nu} | \boldsymbol{q}_j \rangle$. So the fitted frequencies are given by

$$\nu_{f,l}(n) = \sum_j a_j q_{j,l}(n), \tag{2.9}$$

where f is for the fitted frequencies.

A very important remark about the orthonormalization, is that the standard deviations of the coefficients a_j are $\sigma(a_j) = 1$, and they are independent. This property gives the ability to the method to build seismic indicators that are as little correlated as possible and to put stringent constrains on the stellar structure, with reduced standard deviations, compared to classical indicators.

2.3.1 Smooth component

Let's see now the vector sub-space for the smooth component. In the observed frequencies, the set of radial orders and σ_i are often different for each spherical degree. In addition, the smooth component depends on l, because it is affected most by the deep layers of the star, which makes its basis elements to also depend on l. The polynomials are given then by the general form:

$$p_{lk} = \delta_{ll'} p_k(n), \tag{2.10}$$

where $\delta_{ll'}$ is the *Kronecker* delta which compares two spherical degrees l and l'. It is zero when they are different and 1 when they are the same. This leads to the distinction of the basis elements from one l to the other, $p_k(n)$ is a polynomial in the radial order n, and k represents the order of the polynomial. What was defined previously as j, now is splitted into two indices, the spherical degree l, and the ordered power k. In order to comprehend better, the spherical degree and the ordering will be explicitely written for the transformation matrix as R^{-1}_{l,k,k_0}. The orthonormal basis elements will then be given by:

$$q_{lk}(n, l') = \delta_{ll'} q_{lk}(n), \tag{2.11}$$

which in turn gives

$$a_{lk} = \langle \boldsymbol{\nu} | \boldsymbol{q}_{lk} \rangle = \sum_n \frac{\nu(n, l) q_{lk}(n, l)}{\sigma^2}, \tag{2.12}$$

in which we see that the introduction of the Kronecker δ, in Eqs. 2.10 and 2.11, results in the sum to collapse over only one fixed spherical degree. For the smooth part, the observed frequencies are grouped based on their spherical degree, and they are treated separately, so that the parameters that are associated to a specific degree, depend only on the frequencies of this degree.

The observed frequencies of solar-like stars, are limited mostly to modes of low spherical degree ($l \leq 3$) and high radial order, which makes the use of the asymptotic theory of non-radial stellar oscillations (Gough (1986)) possible. Therefore, we get that, at first order, the formulation of the expected frequencies as a function of n and l is given by:

$$\nu(n, l) \simeq \left(n + \frac{l}{2} + \epsilon \right) \Delta, \tag{2.13}$$

where ϵ is a constant offset mainly affected by the superficial layers, $\Delta = \left(2 \int_0^{R_\star} \frac{\mathrm{d}r}{c(r)} \right)^{-1}$ is the asymptotic large frequency seperation, $c(r)$ is the sound speed profile in the adiabatic case, and $R_\star$ is the radius of the star. Inspired by this formulation, we use a linear representation for the first 2 polynomials. The polynomials in n, from the right hand side of Eq. 2.10, that are used to represent the smooth part of the spectrum are given by

$$p_0(n) = 1, \tag{2.14}$$

$$p_1(n) = n, \tag{2.15}$$

$$p_2(n) = n^2, \tag{2.16}$$

where the last one was obtained after testing several combinations of powers in order to get the optimal χ^2 value. We have that, since there are three polynomials for each l value, the vector sub-space that is built for the smooth component, is $3 \times l$ dimensions. That means that, if we have four values for l (0, 1, 2, 3 for example, which is quite common for observations), we have 12 dimensions in total. It is important to mention that, we need more than three observed frequencies for each l in order for the method to be able to work, because we need at least one constrain per free parameter.

2.3.2 Glitch component

Previously developed methods that also adjust for the glitches (see for example Verma et al. 2014), are using formulations that are non-linear. As a result, most of those methods can be unstable, and need quite some time to process the frequencies, which is an important drawback when working with a big amount of data. The WhoSGlAd method uses a linearlised formulation for the glitches to solve these problems. Furthermore, it was developed to limit the correlations between indicators and to adjust simultaneously and coherently, the glitch and the smooth components. The formulations that are used are the following, for the helium glitch:

$$p_{\mathrm{He},Ck}(\tilde{n}) = \cos(4\pi T_{\mathrm{He}}\tilde{n})\tilde{n}^{-k}, \tag{2.17}$$

$$p_{\mathrm{He},Sk}(\tilde{n}) = \sin(4\pi T_{\mathrm{He}}\tilde{n})\tilde{n}^{-k}, \tag{2.18}$$

with k=(4,5) and for the convection zone glitch:

$$p_{CC}(\tilde{n}) = \cos(4\pi T_{\mathrm{CZ}}\tilde{n})\tilde{n}^{-2}, \tag{2.19}$$

$$p_{CS}(\tilde{n}) = \sin(4\pi T_{\mathrm{CZ}}\tilde{n})\tilde{n}^{-2}, \tag{2.20}$$

where $\tilde{n} = \left(n + \frac{l}{2}\right)$, ν is replaced by its first order approximation $\tilde{n}\Delta$, from equation 2.13 of the asymptotic formulation, and $T_{\mathrm{He}} = \tau_{\mathrm{He}}\Delta$ and $T_{\mathrm{CZ}} = \tau_{\mathrm{CZ}}\Delta$ are the dimensionless forms of the acoustic depths and we will refer to them as *dimensionless acoustic depth.* Also, the indices He and CZ correspond to the helium glitch and the convective zone glitch, respectively. The above formulations are linear and so we do not get the disadvatages of non-linearity.

The degrees −4 and −5 were chosen by the authors, after they proved that they are the best to reproduce the decrease of the glitch amplitude towards high frequencies. They also showed that the method is stable. The glitches finally are given by:

$$\delta\nu_{\mathrm{He}}(\tilde{n}) = \sum_{k=5}^{4}[s_{\mathrm{He},k}p_{\mathrm{He},Sk}(\tilde{n}) + c_{\mathrm{He},k}p_{\mathrm{He},Ck}(\tilde{n})], \tag{2.21}$$

$$\delta\nu_{\mathrm{CZ}}(\tilde{n}) = [s_{\mathrm{CZ}}p_{CS}(\tilde{n}) + c_{\mathrm{CZ}}p_{CC}(\tilde{n})]. \tag{2.22}$$

This formulation allows the Gram-Shmidt process to take place and to generate the orthonormal vectors to append the smooth component basis.

The glitch is generated in the superficial layers and so it doesn't depend on l. For that reason, the basis elements are defined independently of l and so are the coefficients c and s. This makes the vector sub-space, associated to the glitch, to be of only 6 dimensions, and it is used to complete the orthonormal basis, over which the frequencies are projected. The glitch contribution can then be given by:

$$\delta\nu_g = \delta\nu_{\mathrm{He}} + \delta\nu_{\mathrm{CZ}}. \tag{2.23}$$

We should note, at this point, that the basis functions depend on the acoustic depths of the second helium ionization zone for T_{He}, and on the base of the convective zone for T_{CZ}, and this dependance is non-linear. In order for the linearity of the method to be maintained, it is necessary for the values of T_{He} and of T_{CZ} to be provided, and to keep them unchanged for the generation of the basis, over which the frequencies are projected. When working with models, because we have access to the stellar structure, this value is obtained by using:

$$\tau_{\mathrm{He/CZ}} = \int_{r_{\mathrm{He,CZ}}}^{R_\star} \frac{\mathrm{d}r}{c(r)}, \tag{2.24}$$

which is the definition of the acoustic depth. In that relation $r_{\mathrm{He,CZ}}$ is the position of the second ionization zone of helium and of the base of the convective zone, respectively. For r_{He} we find the position of the local maximum between the two local minima of the Γ_1 depletion, due to the partial ionization zone of He and, for r_{CZ}, we find the last point below the surface for which $\nabla < \nabla_{\mathrm{rad}}$, accoding to the Schwarzchild criterion (see section 1.2.2.4 for more details).

When we work with observations however, r_{He}, r_{CZ}, and $c(r)$ are not known and so we cannot provide a value for τ_{He} and for τ_{CZ}, respectively. In order to retrieve an initial guess, we first fit a

Table 2.1: The set of frequencies used in the example.

$l=0$			$l=1$			$l=2$		
n	$\nu(\mu Hz)$	$\sigma(\mu Hz)$	n	$\nu(\mu Hz)$	$\sigma(\mu Hz)$	n	$\nu(\mu Hz)$	$\sigma(\mu Hz)$
13	1498.89	0.07	13	1546.42	0.07	13	1596.42	0.19
14	1603.60	0.07	14	1651.36	0.09	14	1701.68	0.17
15	1708.55	0.08	15	1755.56	0.08	15	1805.69	0.11
16	1812.40	0.07	16	1860.40	0.05	16	1910.30	0.10
17	1916.65	0.06	17	1965.44	0.05	17	2016.47	0.08
18	2022.56	0.05	18	2071.47	0.05	18	2122.70	0.06
19	2128.56	0.04	19	2178.50	0.04	19	2229.41	0.06
20	2234.84	0.05	20	2284.98	0.05	20	2336.56	0.09
21	2341.67	0.05	21	2391.77	0.06	21	2443.24	0.13
22	2448.06	0.08	22	2499.11	0.08	22	2550.54	0.21
23	2554.95	0.16	23	2606.15	0.13			

model to seismic indicators of the smooth part, which are independent of the glitches. Then, because we have the structure of that model, we may use Eq. 2.24. The next step could be the use of any minimisation algorithm in order to optimize over the values of τ_{He} and of τ_{CZ}. This nevertheless would break the linearity of the problem. In addition, the obtained values of τ_{He} and of τ_{CZ}, stay close to the theoretical values and, as a result, they do not contribute much in the minimisation of the merit function (2.6). For those reasons we do not use it.

In the present work, we developed a method that solves this problem, and provides a value for the helium acoustic depth by using linear relations. In that way we skip the partial modeling, which is necessary for the estimation of τ_{He}, making the method faster, when working with observations. Moreover, the problem becomes linear again, which means that the computations are fast. Furthermore, it is model independent, which means that it can be implemented in the code and provide results in an automated way, which makes it more efficient. Something similar could be done for the convection zone glitch as well. However, we did not do that here because the signal of this glitch, hence its amplitude, is quite weak in solar-like stars and so it carries little information.

τ_{He} is necessary to derive the helium amplitude (A_{He}), which is a proxy for the helium abundance in that area, and, since it is very close to the surface, we can derive the surface helium abundance of the star, something which is not possible to retrieve in solar-like stars, from other methods, that do not use the glitches.

2.3.3 An example

In order to illustrate the basis elements, that are given by their method, Farnir et al. (2019) provided an example, proving that their adjustments work. To do so, they used the set of frequencies listed in table 2.1. Those data are from the 16 Cygni A with a magnified convection zone glitch by a factor of 3, so that it would be better visualized.

In Fig. 2.2 and 2.3 the authors show the successive adjustments of the basis functions, which shows that they represent well the data, and, as a result, it shows that the method is accurate. Those values were obtained by the procedure mentioned in subsections 2.3.1 and 2.3.2. To recap it, the frequencies are being processed using the Gram-Schmidt orthonormalization procedure. The elements of the former basis elements, $p_j(n,l)$ are projected one after another, on an othogonal basis (Eq. 2.8) and then they are normalised in order to obtain the orthonormal basis elements $q_{j_0}(n,l)$, and the tranformation matrix, R^{-1}_{j,j_0}. The fitted frequencies, $\nu_f(n,l)$ (Eq. 2.9), of the smooth part come as the result of the projection of the frequencies on the orthonormal basis, related to the smooth component.

For the glitch part, the frequencies are projected on the corresponding basis elements at the same time for all the spherical degrees, because their coefficients do not depend on it.

In Fig. 2.2 and 2.3, we illustrate the basis elements used for the example. In Fig. 2.2, is presented the smooth part of the frequencies from table 2.1, with respect to their radial order n. The straight line in the upper panel of Fig. 2.2 corresponds to the zero and first order functions, and the points with the errorbars are the data. In the lower panel of the same figure, the continuous curved line corresponds to the second order functions only, and the points respresent the residuals of the adjustment of first order, again with respect to the radial order n. We see that there is important improvement, but there are still some differences. The fact that the fitting is so close to the values, shows that the linear approximation, of the asymptotic theory, already provides a good representation, but still there is a small departure.

Figure 2.3 presents the basis elements of the two glitches, without the smooth component, over $\tilde{n} = \left(n + \frac{l}{2}\right)$. The helium glitch is shown in the upper panel and the convection zone glitch is shown in the lower one, for all the frequencies. The points with the errorbars represent the residuals, of the corresponding glitch amplitude, from which we see that they are very low, and thus, they contribute by a small amount to the frequencies. We see that the signal of the glitch is indeed very small, since it is of the order of 1 μHz. while the frequencies themselves are of the order 1000 μHz. Especially the convection zone glitch has very small amplitude, and this is obvious by the fact that its values in that plot have been multiplied by a factor of 3, in order to be obvious. The line is the fitting for the values of the glitches, by which we can clearly see the oscillatory nature of the glitches.

2.4 Seismic indicators

The use of the Gram-Schmidt process provides fitted coefficients, that are independent of each other. This allows WhoSGlAd to define seismic indicators that are as little correlated as possible.

2.4.1 The large separation

One of the most used seismic indicators is the large separation, $\Delta\nu$. In WhoSGlAd, the Gram-Schmidt orthonormalisation begins with the smooth component of each spherical degree, and subsequently treats them in increasing polynomial order. So, the first one to be treated is the zero order, of the smooth component, of the radial modes, that is with $l = 0, k = 0$. Next is the first order polynomial of the radial modes and so on. The reason for proceeding in that specific order is because, frequencies can be approximated at first order by the formulation of the asymptotic theory, Eq. 2.13. This formulation is linear as a function of the radial order and $\Delta\nu$ corresponds to its slope. That means that, for each l, the projection of the frequencies over the first 2 basis elements provides us with a linear adjustment of the frequencies and an estimator of the large separation. So, WhoSGlAd defines a different $\Delta\nu$ for each subset of frequencies of the same spherical degree, as the slope of that set and it is given by:

$$\Delta_l = a_{l,1} R_{l,1,1}^{-1}. \tag{2.25}$$

We could also express it as a function of frequencies and radial orders. By knowing the vector of frequencies that is associated to the spherical degree l, $\boldsymbol{\nu}_l$, and the vector of corresponding radial orders, $\boldsymbol{n}_l$, we have that:

$$\Delta_l = \frac{\langle \boldsymbol{\nu}_l | \boldsymbol{n}_l \rangle / \parallel \mathbf{1} \parallel^2 - \overline{\boldsymbol{n_l}}\, \overline{\boldsymbol{\nu}_l}}{\parallel \boldsymbol{\nu}_l \parallel^2 / \parallel \mathbf{1} \parallel^2 - \overline{\boldsymbol{n}_l}^2}, \tag{2.26}$$

where $\mathbf{1} = (1, 1, ..., 1)$ and the $\bar{\cdot}$ is called the weighted mean and is given by

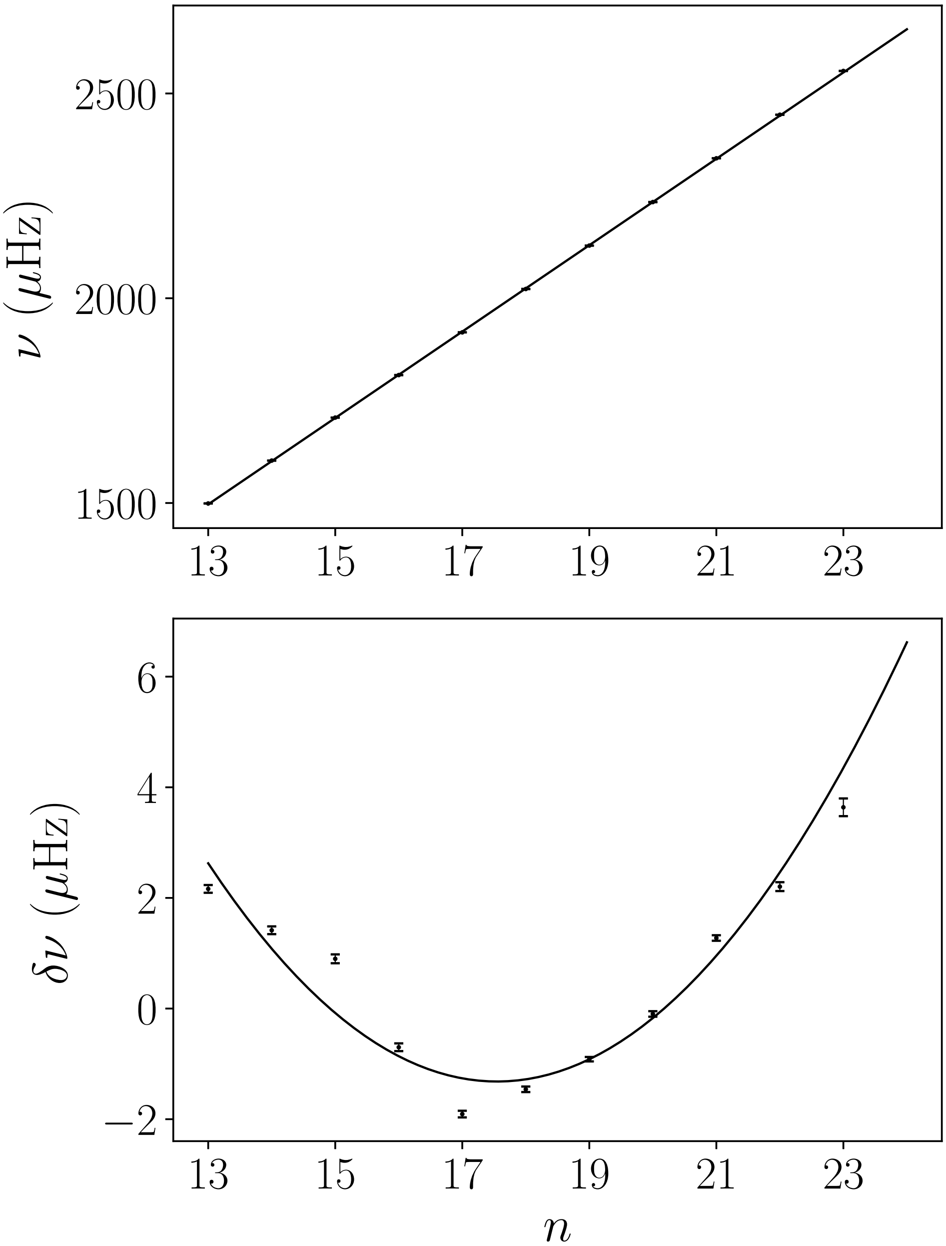

Figure 2.2: The basis elements of the example. *Upper panel*: The first order fit of the smooth part of the frequencies with respect to the radial order. The points with the errorbars correspond to the data. *Lower panel*: The second order fit of the residuals between the frequencies and their first order fit, for the smooth part as well. The points with the errorbars correspond to the data, as well.

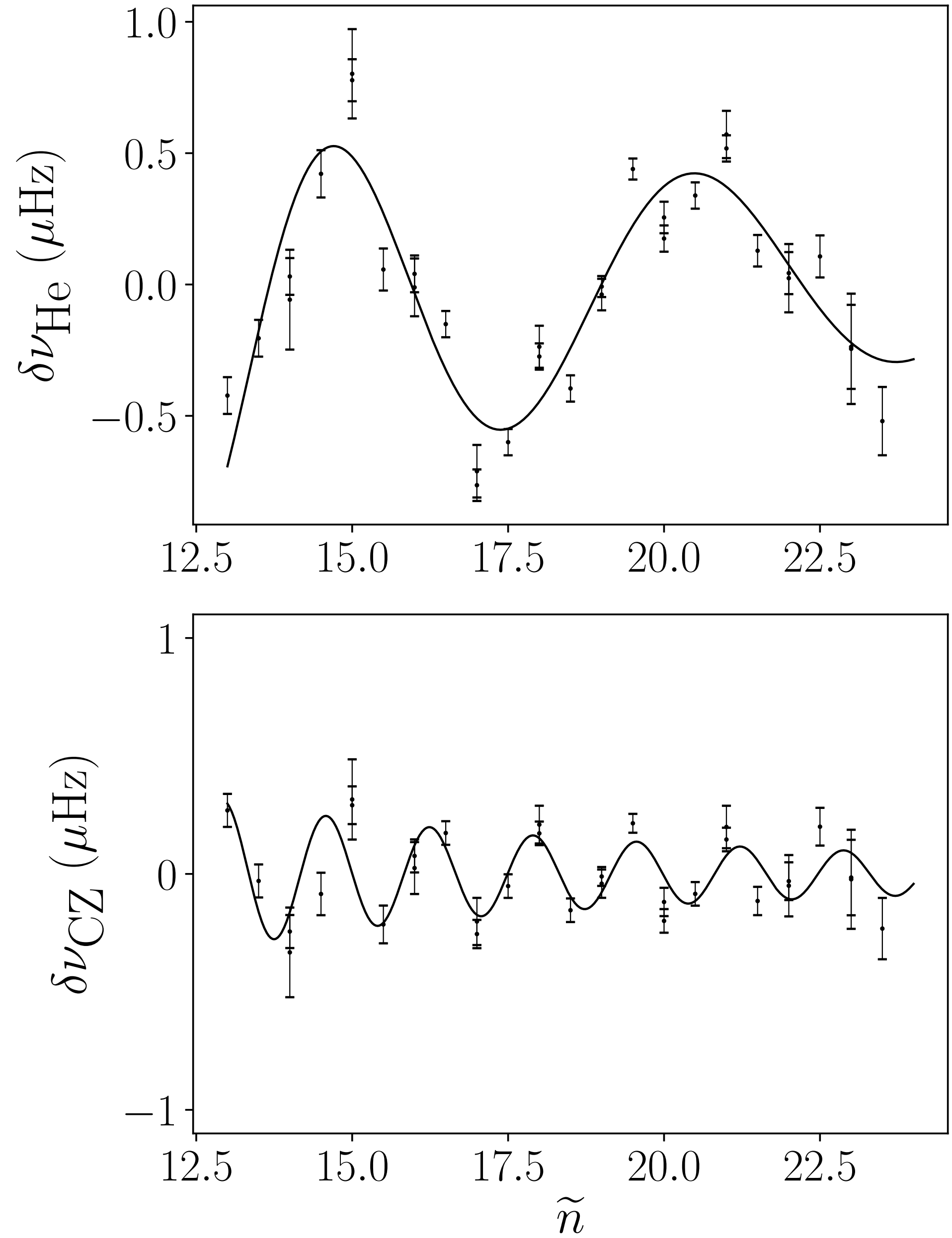

Figure 2.3: *Upper panel*: Adjustment for the helium glitch. *Lower panel*: Adjustment for the convection zone glitch (lower panel) for the frequencies of spherical degree l =0. The points with the errorbars represent the residuals, of the corresponding glitch amplitude.

$$\overline{\boldsymbol{\nu}} = \frac{\langle \boldsymbol{\nu}|\mathbf{1}\rangle}{\| \mathbf{1} \|^2} = \frac{\sum_{i=1}^{N} \nu_{n_i}/\sigma_i^2}{\sum_{i=1}^{N} 1/\sigma_i^2}. \tag{2.27}$$

The previous definitions are for only one spherical degree. The mean large separation, or else the large separation over all the spherical degrees, is also given by

$$\Delta = \overline{\boldsymbol{\Delta_l}} = \frac{\sum_l \Delta_l/\sigma^2(\Delta_l)}{\sum_l 1/\sigma^2(\Delta_l)}, \tag{2.28}$$

where $\sigma(\Delta_l)$ is the uncertainty on the large separation of degree l. This is one of the most important seismic indicators because it is a proxy of the mean stellar density, accordingly to Ulrich (1986) and is sensitive to both the age and mass of the star.

2.4.2 Normalised small separations

Other important indicators are the small separations. Common definitions are the following:

$$d_{01}(n) = (\nu_{n,1} - 2\nu_{n,0} + \nu_{n+1,1})/2, \tag{2.29}$$

$$d_{02}(n) = \nu_{n,0} - \nu_{n-1,2}, \tag{2.30}$$

where the indices of d are for the spherical degree while those of ν correspond to the radial order and spherical degree. So the first equation corresponds to the separations between radial and dipolar modes, and the second one to differences between radial and quadrupolar modes. They are important because they allow for a measurement of the spacing between the observations and the asymptotic relation (Eq. 2.13). Their disadvantage is that the surface effects highly influence them. Those effects are due to the non-adiabaticity of the superficial layers of the star, and to the interaction between the convection and the oscillations, which are not well understood. In order to decrease those effects on the small separations, Roxburgh & Vorontsov (2003a) divided them by the large separation and so got new definitions for the small separations that are almost independent of those layers. They are the normalised small seperations:

$$r_{01}(n) = \frac{d_{01}}{\Delta_{\boldsymbol{r},1}(n)}, \tag{2.31}$$

$$r_{02}(n) = \frac{d_{02}}{\Delta_{\boldsymbol{r},1}(n)}, \tag{2.32}$$

where $\Delta_{\boldsymbol{r},l} = \nu_{l,n} - \nu_{l,n-1}$ is the large separation.

Inspired by these definitions, comes the definition of the small separation ratio in WhoSGlAd, that represent the spacing between the ridges of spherical degrees 0 and l, in the échelle diagram. If we consider that the asymptotic relation is valid, the spacing between ridges 0 and l, $\frac{\overline{\boldsymbol{\nu_0}}-\overline{\boldsymbol{\nu_l}}}{\Delta_0}$, can be approximated by $\overline{\boldsymbol{n_0}} + \epsilon_0 - (\overline{\boldsymbol{n_l}} + \epsilon_l + l/2)$. The authors added the term $\overline{\boldsymbol{n_0}} + (\overline{\boldsymbol{n_l}} + l/2)$ in order for the value to come closer to $\epsilon_0 - \epsilon_l$. From that we take the equation:

$$\hat{\boldsymbol{r}}_{0l} = \frac{\overline{\boldsymbol{\nu_0}} - \overline{\boldsymbol{\nu_l}}}{\Delta_0} + \overline{\boldsymbol{n_l}} - \overline{\boldsymbol{n_0}} + \frac{l}{2}, \tag{2.33}$$

which is the mean value of the small separation, and where $\overline{\boldsymbol{\nu_l}}$ and $\overline{\boldsymbol{n_l}}$ are respectively the weighted mean values of $\nu_l(n)$ and of n for the spherical degree l, in agreement with Eq. 2.27. Also $\overline{\boldsymbol{\nu_l}} = a_{l,0}R^{-1}_{l,0,0}$ corresponds to the fitting of zero order of the frequencies of spherical degree l, and so it is its mean value. Eq. 2.33 represents the mean spacing in the échelle diagram while equations 2.29 and 2.30 represent the local spacing. The uncertainties on the WhoSGlAd separation ratios are reduced in comparison to the local values.

The defined small separations are important because they provide information about different features of the stellar interior. $\hat{\boldsymbol{r}}_{02}$ is an indicator for the conditions close to the core and, as a result, it holds information about the evolutionary stage of the star, on the main sequence. That is because its evolution is almost monotonic for solar-like stars, and it is sensitive to the gradient of the sound speed, which highly depends on the chemical composition. As evolution proceeds, H is tranformed into He, and μ changes. $\hat{\boldsymbol{r}}_{01}$, on the other hand side, does not hold information about the evolutionary stage, but it can be used as an indicator for the upper limit of the convective core overshooting and for the chemical composition for example. This was shown by de Meulenaer et al. (2010), for stars with masses and metallicities close to that of α Centauri A (HD128620), by using a similar indicator as $\hat{r}_{01}$. Finally $\hat{\boldsymbol{r}}_{03}$ does not provide any new information, as its evolution is reduntant with that of $\hat{r}_{02}$.

2.4.3 Large separations differences

We may also define differences between the large separations among the sets of modes with spherical degrees 0 and l. For that, the authors built an indicator to compare the large separations for different l which is given by:

$$\Delta_{0l} = \frac{\Delta_l}{\Delta_0} - 1. \tag{2.34}$$

Given that, we can combine $\hat{r}_{01}$, which gives an estimation of the mean values of the orders 0 and 1, with Δ_{01} in order to retrieve information about the amount of core overshooting, as it was shown by Deheuvels et al. (2016).

2.4.4 ϵ estimator

In Eq. 2.13 for the asymptotic regime, there is the constant term ϵ, which is mostly affected by surface effects. For an estimator of ϵ, the method defines a subspace in which the frequencies are represented as:

$$\nu(n,l) = \left(n + \frac{l}{2} + \epsilon\right)\hat{\Delta} = \left(n + \frac{l}{2}\right)\hat{\Delta} + K, \tag{2.35}$$

where $\hat{\Delta}$ and K are free parameters. Then comes the definition of an orthonormal basis over this sub-space: $\tilde{\boldsymbol{q}}_0$ and $\tilde{\boldsymbol{q}}_1$. The last step is the projection of the frequencies over this basis, and the identification of the different coefficients with Eq. 2.13. In doing so, we also get an estimate for the large separation, other than Eq. 2.25. It is shown by the authors that this indicator is sensitive to the mass only when the star gets older on the main-sequence, and that it can be used to distinguish between different choices of surface effects corrections.

2.4.5 Glitch amplitude

All the seismic indicators that we presented so far, had to do with the smooth component of the observed frequencies. We now define indicators associated with the glitch. Very important indicator is the glitch amplitude. By the formulation of the method, it is simply given by the norm of the glitch term and its general form is:

$$A_g = \parallel \boldsymbol{\delta_g} \parallel, \tag{2.36}$$

with $\boldsymbol{\delta_g}$ being the glitch term. More specificaly, for the helium glitch, it is given by:

$$A_{\mathrm{He}} = \sqrt{C_{\mathrm{He},5}^2 + S_{\mathrm{He},5}^2 + C_{\mathrm{He},4}^2 + S_{\mathrm{He},4}^2}. \tag{2.37}$$

Also, it is independent of the other indicators due to the orthonormalisation and has a standard deviation of 1. The authors showed that the helium amplitude is a proxy of the surface helium abundance, Y_f. This is something that makes sense, because a higher helium abundance would lead to a deeper depression of the Γ_1 index, as shown in Fig. 2.1, hence to a higher value of the helium amplitude. However, it is important to mention that the metallicity works in the opposite way, the higher the metallicity, the shallower the depression of Γ_1 gets and so the smaller the helium amplitude gets for a given helium abundance, which shows that the relation between A_{He} and Y_s is model dependent.

The convection zone glitch amplitude is given by

$$A_{\mathrm{CZ}} = \sqrt{C_{\mathrm{CZ}}^2 + S_{\mathrm{CZ}}^2}. \tag{2.38}$$

It provides information about the sharpness of the transition region between the convective envelope and the radiative zone, but we will not discuss it further because it carries little information and we do not consider it in our analysis.

2.5 Limitations

WhoSGlAd is developed in order to study the oscillations of solar-like stars, that present p-modes at their surface. For that reason, it cannot be used for the study of stars evolved beyond the main sequence, because those stars present mixed modes, that contain both pressure and gravity modes. In that case it would be able to show information for the p-modes but not for the g-modes. Moreover, the authors clearly show that stars with mass of $1.25M_\odot$ and higher, and for high helium abundances, the relation between the surface helium abundance and the helium glitch amplitude is not monotonic, and so the method becomes unreliable, to relate the glitch signature to the helium content. Therefore, the inferred helium abundance of high-mass or helium-rich stars has to be regarded carefully. Nevertheless, it remains reliable for the smooth component.

In addition, as we mentioned earlier, the method needs an estimation of the helium acoustic depth, (τ_{He}), in order for it to remain linear. That estimation has to come unavoidably from a model, which in turn imposes biases regarding to the initial helium abundance and the metallicity that it considers, as initial values. Those two values affect the depth of the Γ_1 depression in opposite ways, which shows that they should be adapted for each observed star. This would happen in an indirect way by the use of models, something that adds time to the process of the data, as we will explain later. Our method solves that problem and makes the method fast without breaking its linearity, which is the big advantage of the method. It is important to note that WhoSGlAd needs the same number of frequencies as the number of basis elements, hence of coefficients to be fitted.

Chapter 3

Results

3.1 Measuring the helium acoustic depth

As it was mentioned earlier, one of the limitations of WhoSGlAd is that it needs an estimate for the acoustic depth of the glitches ($\tau_{\mathrm{He/CZ}}$), that will work as the initial guess for the minimization technique. If it was to provide an estimate for the acoustic depths, it would have to go through one more minimization over them, that would result in non-linear relations and in correlations between the parameters of the fit. This is undesired since it would ruin the advantages of the method that are that it is fully linear, which makes it fast, and that the different parameters are as little correlated as possible. In order to avoid that, the introduction of a fixed value for those acoustic depths is necessary. When we work with models, this is not a problem because we have access to the stellar structure and so we know the position of the second ionization zone of He, and of the sound speed profile above it. Therefore, we can calculate it by the following relationship

$$\tau_{\mathrm{He}} = \int\limits_{r_{\mathrm{He}}}^{R_\star} \frac{\mathrm{d}r}{c(r)}, \tag{3.1}$$

where r_{He} is the position of the local maximum of Γ_1, between the two minimums, $R_\star$ is the radius of the star, and $c(r)$ is the sound speed as a function of the distance from the centre of the star.

When we work with observed data however, this is not the case since we do not have access to the stellar structure of the star we observe. In order to find the acoustic depths, we would rather proceed in the following way:

1. First we use the observed frequencies to retrieve a set of seismic indicators that are connected to the smooth part of the spectrum, and indicative of the stellar structure, like for example $\Delta, \hat{r}_{01}$, and $\hat{r}_{02}$.
2. The next step is to find a model that best represents the observed seismic indicators. This is a time consuming procedure, since the algorithms that are responsible for the generation of the models have to go through multiple iterations, in order to obtain the optimal one.
3. Since we have now access to the stellar structure of that model, which provides a good approximation of the stellar structure of the observed star, the last step is to use model quantities to calculate the acoustic depth according to Eq. 3.1.

After that, we could use that value as the estimate of the acoustic depth, in order to re-run WhoSGlAd and finally obtain the helium amplitude (A_{He}). It is obvious that this process takes quite some time to be completed, because it requires the generation of the models and, furthermore, it is model dependent, which again ruins the advantage of fast computations of the method. Nevertheless, it does not affect its efficiency, because, as it was shown in Farnir et al. (2019), departures of even up to 10 % from the estimated value have a negligible effect on the measured helium amplitude.

The already large amount of available asteroseismic data, thanks to the already completed missions, such as CoRoT (Baglin et al. 2009) and *Kepler* (Borucki et al. 2010), and the ongoing TESS (Ricker et al. 2014), is expected to be increased vastly, in the coming years, with the advent of new missions like PLATO (Rauer et al. 2014). It is clear that there is the need for an automated, fast, and model independent method that could analyse those data in an efficient way. In regard to those specific needs, the aim of my work was to upgrade WhoSGlAd and to make its analysis of observed seismic data fully automated and model independent, thus enabling the fast treatment of these data. It was based on an idea of one of my supervisors, Martin Farnir, which was to relate the dimensionless acoustic depth of the second ionization zone of helium T_{He}, which is defined in Farnir et al. (2019) as

$$T_{\mathrm{He}} = \tau_{\mathrm{He}} \cdot \Delta, \tag{3.2}$$

to easily accessible and precise observables, for solar-like stars.

Our first choice was to relate it to the effective temperature T_{eff} and to the luminosity L, as in a HR diagram, because those two quantities already provide a lot of information about the evolution of the star. Furthermore, because, for a given pressure, the second ionization of helium takes place at a specific range of temperatures, it would follow that the depth at which it happens, which depends on the stratification of the temperature, would be related to T_{eff}. However, the seismic indicators that are provided by WhoSGlAd, are more precise than the spectroscopic constrains and therefore, we chose Δ_0 and $\hat{r}_{02}$ instead. We chose those two seismic indicators because, Christensen-Dalsgaard (1988) show that the classical $\Delta\nu$ and d_{02}, are good indicators of the stellar evolution, and Farnir et al. (2019), showed that their expressions hold the same information. Moreover, by plotting $\hat{r}_{02}$ as a function of Δ_0, over a grid of models, they showed that they are related in an almost monotonous way. $\hat{r}_{02}$ is similar to the small separation ratio (Roxburgh & Vorontsov 2003b), which is sensitive to the sound speed gradient and, as a result, to the chemical composition. So, it carries information about the conditions near the core, and, as a consequence, about the evolutionary stage of the star on the main sequence, as its evolution is almost monotonous. We show in Fig. 3.1 a seismic diagram, representing $\hat{r}_{02}$ as a function of Δ_0, on a grid of models that we made for our analysis. In this grid, the tracks are for stellar masses from $0.8\,M_\odot$ to $1.15\,M_\odot$ with a step of $0.05\,M_\odot$, for an initial chemical composition of X=0.75 and Z=0.012. From this plot, we can see the almost monotonous relation between those two seismic indicators.

In order to check that $\hat{r}_{02}$, Δ_0, and T_{He} are related by a linear expression, we made a grid of models using different masses ranging from $0.8\,M_\odot$ to $1.2\,M_\odot$, with a step of $0.05\,M_\odot$. We also tested different initial chemical compositions, with values for the hydrogen abundance (X_0) of 0.70, 0.725, and 0.75 and for the metallicity (Z_0) of 0.010, 0.012, and 0.014. We generated the models using the CLES stellar evolution code (Scuflaire et al. 2008), using for the opacity the OPAL opacity table (Iglesias & Rogers 1996), in combination with that of Ferguson et al. (2005) for the case of low temperatures. Moreover we used the FreeEOS code in order to generate the equation of state table from Cassisi et al. (2003), the nuclear reactions rates as given by Adelberger et al. (2011), and we considered only models with a radiative core, for reasons that we will explain later. We also used the AGSS09 solar chemical misxture (Asplund et al. 2009).

We checked whether or not the dimensionless acoustic depth could be connected, at first order, to the mean large seperation, Δ_0 and to the normalised small seperation, $\hat{r}_{02}$, through the relation:

$$T_{\mathrm{He}} = a\Delta_0 + b\hat{r}_{02} + c, \tag{3.3}$$

where a, b, and c are fitting coefficients.

Since we are working with solar-like stars, it is essential to be sure that our models are restricted to the main-sequence phase. Departures from this evolutionary stage would degrade the data because

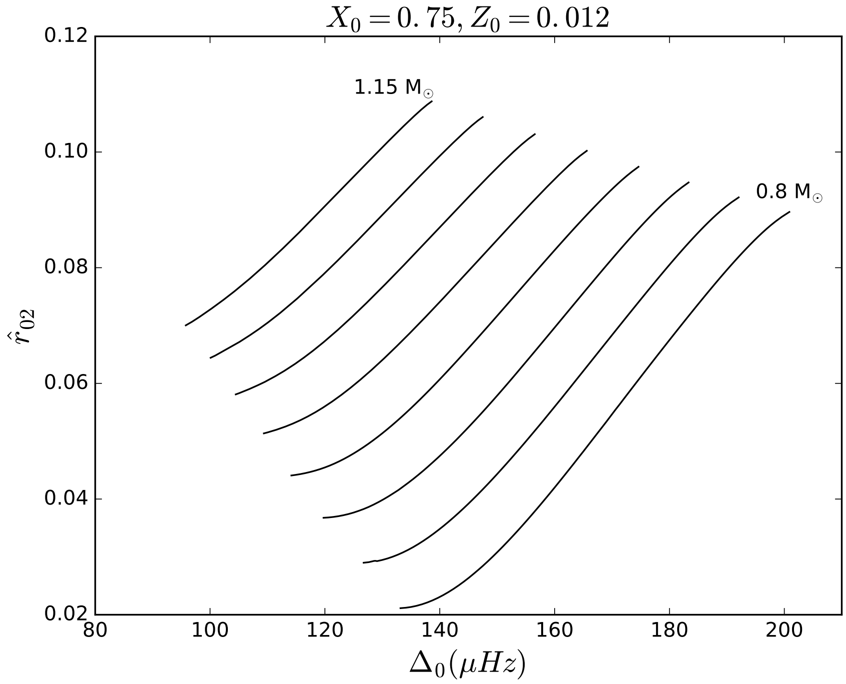

Figure 3.1: The evolution of Δ_0 with $\hat{r}_{02}$ for the masses in the range $[0.8\,M_\odot, 1.15\,M_\odot]$ with a step of $0.05\,M_\odot$, for an initial chemical composition of X=0.75 and Z=0.012.

models that extend beyond the main sequence phase, evolve in a non-monotonous way, as it is shown in Fig. 3.2, which means that non-linearities are introduced. This is problematic because we want to relate $T_{\rm He}$ to Δ_0 and $\hat{r}_{02}$, using a simple linear formulation. In this plot, we show the evolution of Δ_0, measured in μHz with respect to the normalised small separation $\hat{r}_{02}$, as it is defined by WhoSGlAd (Eq. 2.33), for models with masses in the range $0.8\,M_\odot$ to $15\,M_\odot$, with a step of $0.05\,M_\odot$, for an initial chemical composition of X=0.75 and Z=0.012. The evolution goes from the top right part to the bottom left, as Δ_0 decreases with the evolution on the main-sequence phase (Farnir et al. 2019). The color in each track represents the evolution of $T_{\rm He}$, according to Eqs. 3.1 and 3.2, with its values showing on the colorbar on the right.

We see in that plot, that the lines for each track become curved in their bottom part in the plot, from almost straight in the rest of it. This is because the main-sequence phase ends, approximately at the lowest point of the curves, and the models evolve further. As we saw earlier, this introduces non-linearities, and so the Eq. 3.3 does not apply. To select the main sequence models, we used a criterion in central H abundance. The main sequence starts when H has been ignited and its abundance has dropped by approximately 1 %. The main sequence ends once the H is almost fully depleted. This translated into the criteria $X_c \lesssim 5 \times 10^{-2}$.

Also, we noted that the models of $1.2 M_\odot$ and $X_0 = 0.70$, developed convective cores, which lead to the extension of their main-sequence phase. This can be seen in Fig. 3.3, where we used the same criterion for the end of the main-sequence phase as before. This plot is the same as Fig. 3.2 but now with the models being restricted only to the main sequence, via the criteria detailed before. Because the core is fully mixed due to convection, the nuclear reactions have access to a bigger fuel reservoir, which means that they last longer. From the previous discussion, we see that some solar-like stars do have convective cores. This, however, introduces non-linearities, as explained before. Therefore, we rejected the models of $1.2 M_\odot$ from our analysis, regardless of whether they had developed convective cores or not, in order to have comparable and consistent grids.

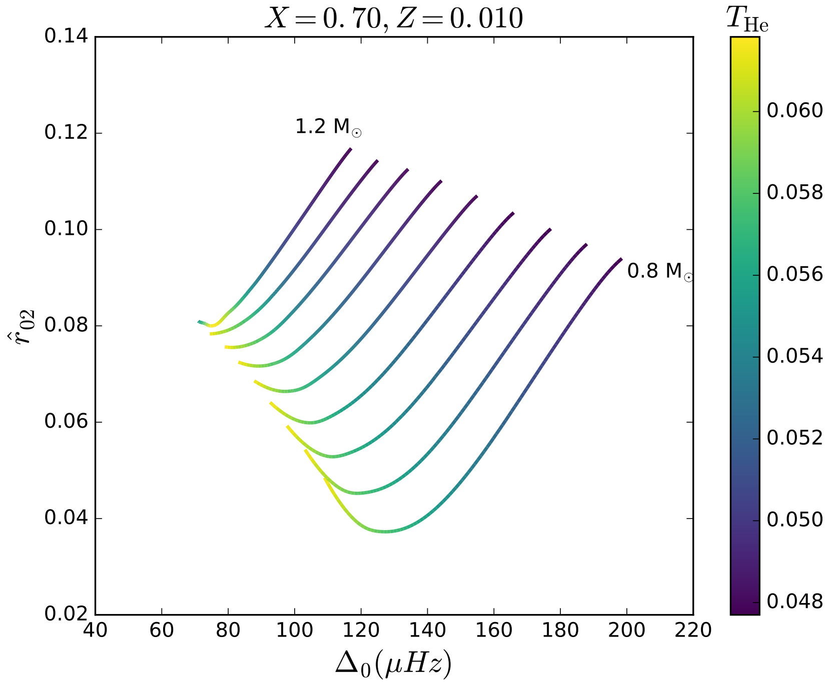

Figure 3.2: The evolution of Δ_0 with $\hat{r}_{02}$ for the masses in range $[0.8\,M_\odot, 1.2\,M_\odot]$, with a step of $0.05\,M_\odot$, for the case of initial chemical composition of X_0=0.70 and Z_0=0.010. The color scale corresponds to the T_{He} value.

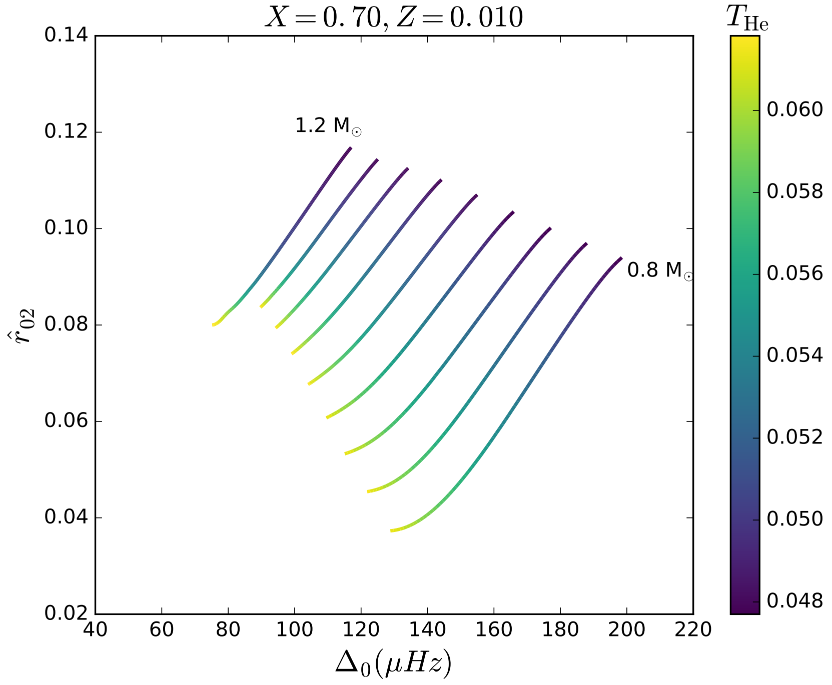

Figure 3.3: The evolution of Δ_0 with $\hat{r}_{02}$ for the masses in range $[0.8\,M_\odot, 1.2\,M_\odot]$, with a step of $0.05\,M_\odot$, for the case of initial chemical composition of X_0=0.70 and Z_0=0.010. The color scale corresponds to T_{He}.

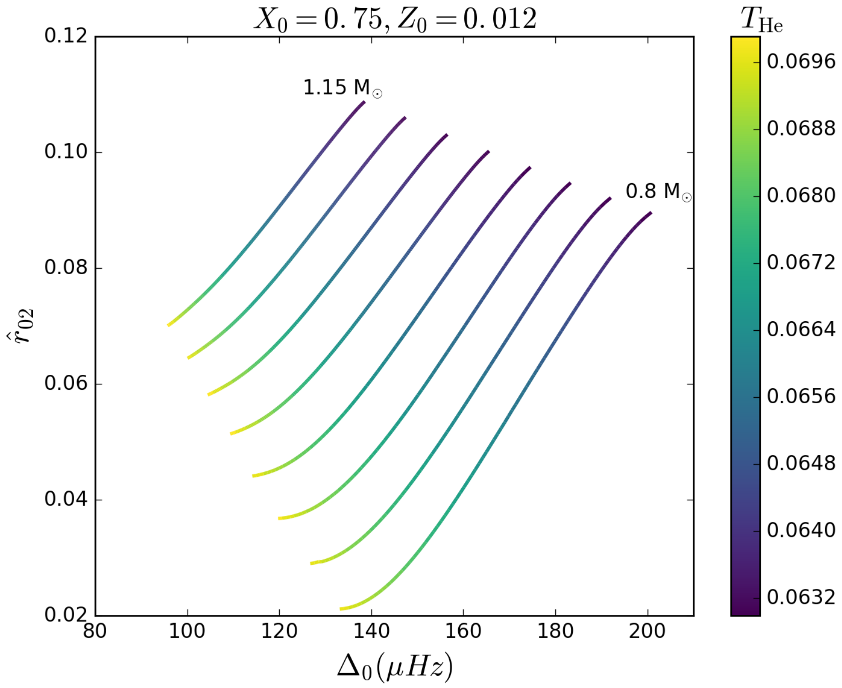

Figure 3.4: The evolution of Δ_0 with $\hat{r}_{02}$ for the masses in range $[0.8\,M_{\odot}, 1.15\,M_{\odot}]$ with a step of $0.05\,M_{\odot}$, for the case of initial chemical composition of X_0=0.75 and Z_0=0.012, which we used as our reference composition. The color scale corresponds here to $T_{\rm He}$ as well.

Next, we checked whether there is s linear relation between $T_{\rm He}, \Delta_0$, and $\hat{r}_{02}$, and we plotted in Fig. 3.4 the evolution of $T_{\rm He}$, over a grid of models for the same mass range as for Fig. 3.2, that are restricted to the main sequence and without convective cores. In that plot, Δ_0 is in the abscissa, $\hat{r}_{02}$ is in the ordinate and $T_{\rm He}$ is represented by the color gradient, like in the previous plots, for the model with initial chemical composition of X_0=0.75 and of Z_0=0.012. We used this chemical composition, as a reference initial chemical composition, for our further analysis. From that plot, we see that there seems to be a linear relation between the three quantities ($T_{\rm He}, \Delta_0$, and $\hat{r}_{02}$), and Eq. 3.3 can be used to estimate the helium acoustic depth. Next, we proceeded to adjust the coefficients of Eq. 3.3. To do so, we fitted Eq. 3.3 to all the tracks in Fig. 3.4, which is our reference initial chemical composition. From the fitting, we obtained the following values for the three coefficients:

$$a \simeq 8.1 \times 10^{-5},\, b \simeq -2.5 \times 10^{-1},\, c \simeq 7.9 \times 10^{-2}. \tag{3.4}$$

The values for the coefficients given in Eq. 3.4, are the ones that we will use in order to provide estimates for $T_{\rm He}$. However, we have first to validate that they are accurate. The first way to validate them was to compare the values of $T_{\rm He}$ that we get with the original method, to those that we get with the new method. We define their relative difference by the relation:

$$\delta T_{\rm He} = \frac{T_{\rm He,fit} - T_{\rm He,mod}}{T_{\rm He,mod}} \tag{3.5}$$

where $T_{\rm He,mod}$ is the value obtained from a model, with Eqs. 3.1 and 3.2, and $T_{\rm He,fit}$ is the value obtained from fitting Eq. 3.3 with the aforementioned coefficients. At first, we did it for the reference chemical composition. We represent in Fig. 3.5, as a color gradient, this difference (Eq. 3.5), over the same grid of models as in Fig. 3.4. It is obvious from that figure that the agreement is extremely good,

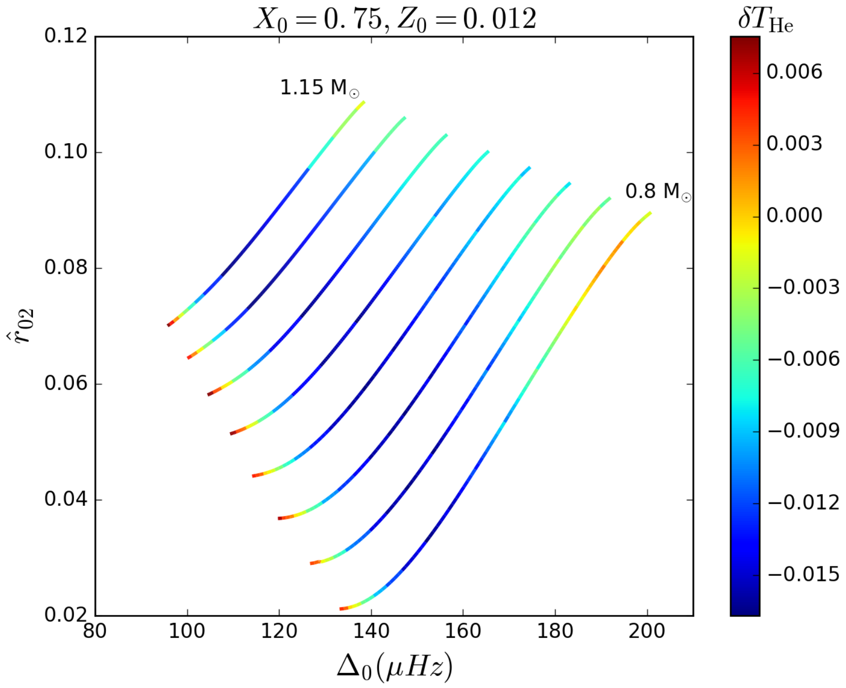

Figure 3.5: The evolution of Δ_0 with $\hat{r}_{02}$ for masses in range $[0.8\,M_\odot, 1.15\,M_\odot]$, with a step of $0.05\,M_\odot$, for the case of initial chemical composition of X_0=0.75 and Z_0=0.012. The color scale here corresponds to the relative difference between the 2 values of $T_{\rm He}$, $\delta T_{\rm He}$.

with a maximum departure for the worst case of only about 1.5 %. This remains well below the 10 % example, that was mentioned earlier to be the maximum disagreement that still yields good results. As a result, we expect the difference to be negligible. In addition, we can see that this difference does not evolve monotonously. As it increases, it goes through a maximum and then decreases during stellar evolution. This is anticipated to happen by non-linearities. Nevertheless, the magnitude of those differences is small, with the maximum being abround 1.5 %, and, thus, it is expected to have negligible effect on the inferred $A_{\rm He}$. In order to be more precise, we found that the biggest difference in $A_{\rm He}$, equals 1.38 %. This discussion shows, that the method we propose is accurate and, therefore, is an excellent replacement of the original method. In that plot, we also see some discontinuities in the color gradient, which we expect to originate from the discrete nature of stellar models, and the determination of $\tau_{\rm He}$, from Eq. 3.1. These discontinuities appear in all the plots that represent the differences according to Eq. 3.5.

From Fig. 3.5 we see that the largest differences appear on the middle parts of the tracks while on their edges the situation is relatively better. In order to better see the differences we illustrated in Fig. 3.6 the evolution of $T_{\rm He,fit}$ and of $T_{\rm He,mod}$ with respect to Δ_0, for the reference chemical composition, for the track of $0.8M_\odot$, which had the biggest differences on the edges. We see from that plot that the differences are quite small, which shows that our method is accurate. In that figure we see that the curve for the track appears several indentations, that we them to be of the same origin as the discontinuities of Fig. 3.5. We also observe that $T_{\rm He}$ evolves almost linearly with Δ_0. The apparent non-linear behaviour of the fitted value arises from the contribution of $\hat{r}_{02}$ (Eq. 3.3).

We carried the same procedure for a different initial chemical composition (X_0 = 0.725, Z_0 = 0.014), using the values for the coefficients that we derived from the previous case, so that we could validate that they can be applied to the other chemical compositions. Figure 3.7 is the same as Fig. 3.5 for the new chemical composition. We see here that, although the differences now are higher, than

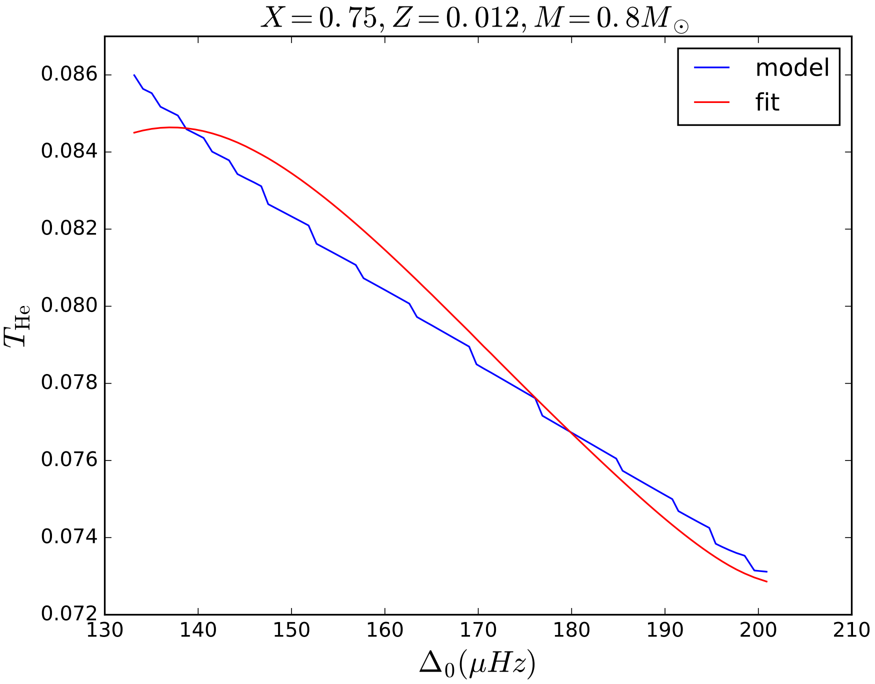

Figure 3.6: The evolution of $T_{\rm He,fit}$ in red, and of $T_{\rm He,mod}$ in blue with respect to Δ_0, for the mass of $1.2M_\odot$, for the case of initial chemical composition of $X_0 = 0.725$ and $Z_0 = 0.014$.

in the other case, with maximum deviation of about 3%, they are still quite low compared to the example of 10% given by the method. Again this validates our method.

In order to check if the $T_{\rm He}$ retrieved with our method is a good substitute of the real $\tau_{\rm He}$ and efficient to use, we calculated the helium amplitude ($A_{\rm He}$), with both of them using observed data, and checked if their difference was within the uncertainties of that parameter ($\sigma = 1$ for the $A_{\rm He}$). We used observations of 16 Cygni A and the original method gave a value of $A_{\rm He}$=29.6 while our method returned a value of $A_{\rm He}$=29.1. Their difference is well in the range of error given by the method, which proves that we can use the Eq. 3.3, in order to have the value of the dimensionless helium acoustic depth directly from Δ_0 and $\hat{r}_{02}$.

To better show the limitations of the method to the cases outside the main sequence, and also to models presenting convective core, we made Fig. 3.8. This figure is the same as Fig. 3.6 but for the model of initial chemical composition of $X_0 = 0.70$ and $Z_0 = 0.010$, which includes post main-sequence models and also icludes the mass of $M = 1.2M_\odot$, which developed a convective core. Δ_0 decreases during the main-sequence phase, as mentioned earlier, because of the slight increase of the stellar radius, which results in the decrease of the mean density and so the beginning of the main sequence is located in the right edge of the curves. The black vertical line indicates the end of the main sequence and so everything to its left, is part of the post main sequence evolution, where we see that the evolution becomes non-linear. On the right of the vertical line, we also see that the evolution is non-linear, for about the second half of the main sequence, which is the effect of the convective core. The offset of the values on that plot, is due to the fact that the fitting coefficients that are used come for the reference initial chemical composition, as it was discussed for the Fig. 3.7.

For the convective core more specifically, we can see it also in Fig. 3.9. This figure is the same as Fig. 3.5 but for $X_0 = 0.70$ and $Z_0 = 0.010$, including the track with convective core. To better illustrate this impact, we carried a new adjustment of Eq. 3.3 on that grid. We see from that figure that the differences become relatively large for that track while they remain small for the rest. Because

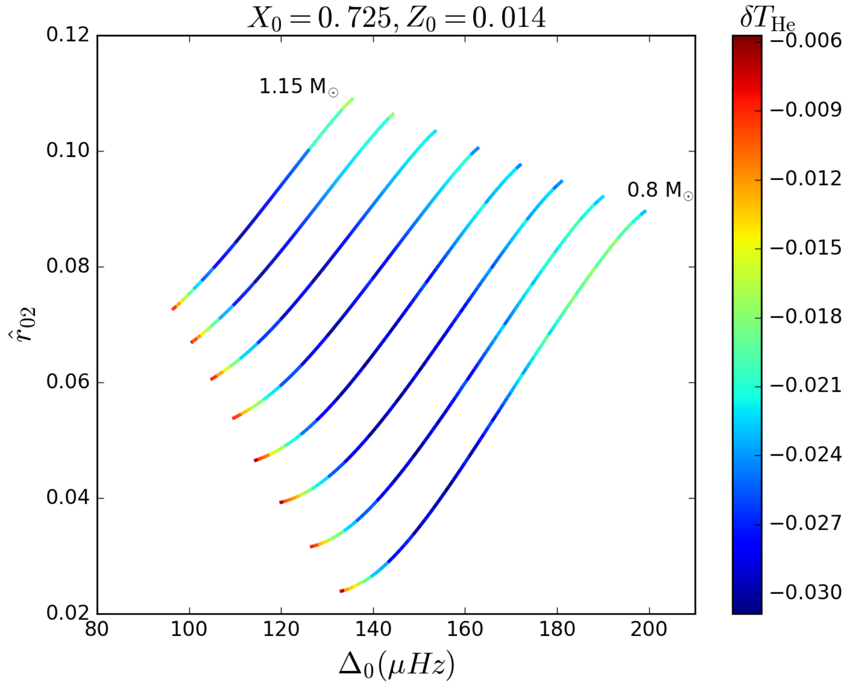

Figure 3.7: The evolution of Δ_0 with $\hat{r}_{02}$ for the masses in range $[0.8\,M_\odot, 1.15\,M_\odot]$ with a step of $0.05\,M_\odot$, for the case of initial chemical composition of X_0=0.725 and Z_0=0.014. The color scale here corresponds to the relative difference between the 2 values of $T_{\rm He}$, $\delta T_{\rm He}$.

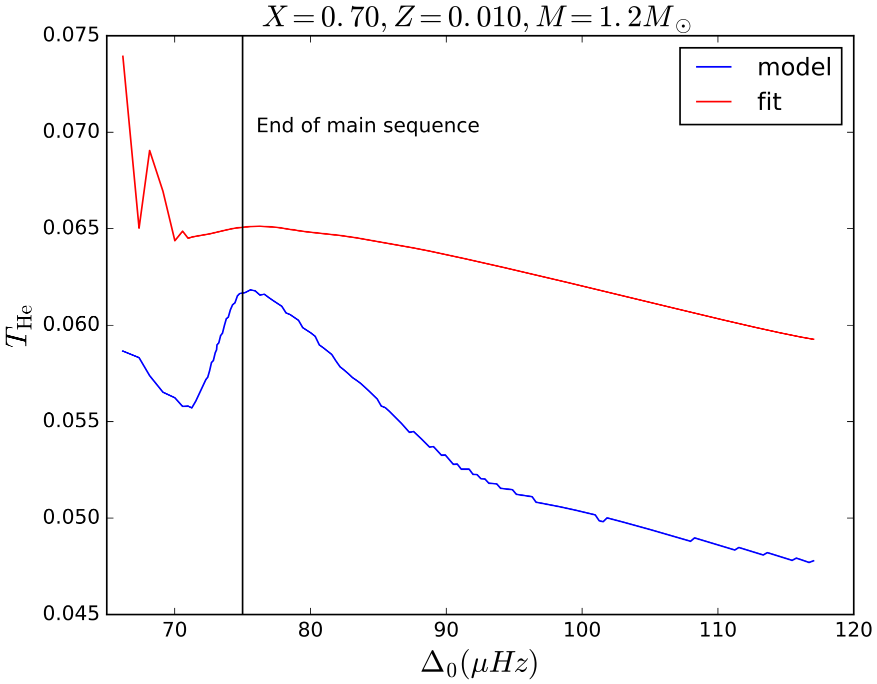

Figure 3.8: The evolution of $T_{\rm He,fit}$ in red, and of $T_{\rm He,mod}$ in blue with respect to Δ_0, for the mass of $1.2M_\odot$, for the case of initial chemical composition of $X_0 = 0.70$ and $Z_0 = 0.010$.

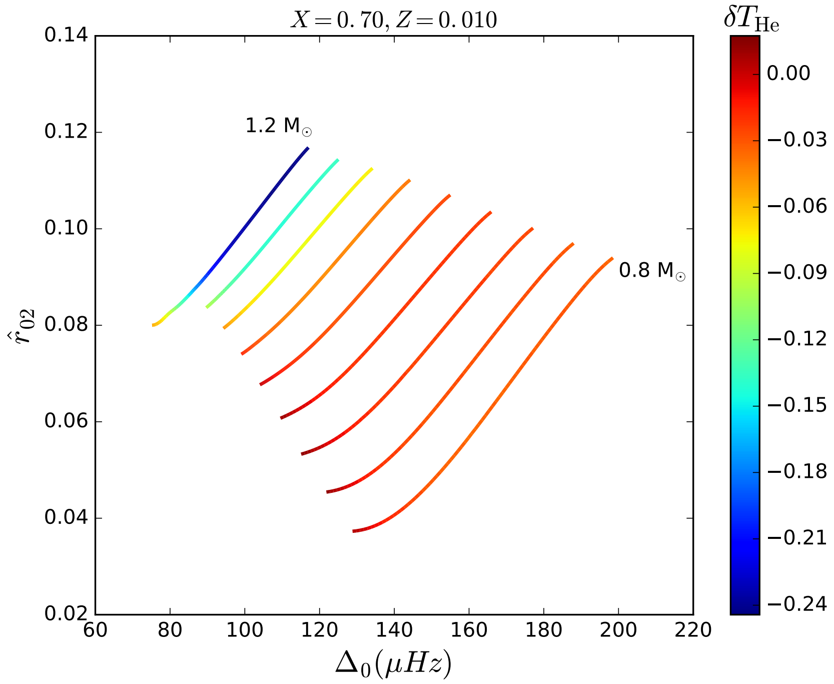

Figure 3.9: The evolution of Δ_0 with $\hat{r}_{02}$ for the 9 different masses, in the range $[0.8\,M_\odot, 1.2\,M_\odot]$, with a step of $0.05\,M_\odot$, for the case of initial chemical composition of X_0=0.70 and Z_0=0.010 for the case of convective core. The color scale here corresponds to the relative difference between the 2 values of T_{He}, δT_{He}. $T_{\mathrm{He,\,fit}}$ has been fitted for all the tracks simultaneously.

the fit is on all the tracks simultaneously, the values of the other tracks are affected too.

To further validate our method, we carried again the same procedure for the compostition that is the furthest away from our reference one ($X_0 = 0.70, Z_0 = 0.010$), using the same values for the coefficients. In Fig. 3.10 we show the same plot as in Fig. 3.5, for that case. The differences here reach values of up to 14 %, for the track of $1.15 M_\odot$, meaning that for further initial chemical compositions our method might not be efficient. In order to see if that is the case or not, we examined the difference of the resulting helium amplitude (A_{He}), between the previous method and our method, for the model that had the biggest δT_{He}. In the former case we retrieved $A_{\mathrm{He}} = 54.53$ and for the latter $A_{\mathrm{He}} = 54.56$. This difference is placed well in the range of $\sigma = 1$, for A_{He} in WhoSGlAd, which shows that our method remains valid even for large values of δT_{He}, hence large variations in the chemical composition. The same procedure was carried for all of the nine models of our grid. Since they present similar results, and the departures of the helium amplitude, are never above the standard deviation defined by WhoSGlAd, we considered that it would be redundant to show them here. Nevertheless, we show them in appendix B for completeness.

3.2 Seismic modeling of KIC10963065

The heart of all the asteroseismic analyses, is the study of stars, with the goal of retrieving values for their internal structure, by modeling. So, in this section, we present the modeling we carried on an observed Kepler target, KIC10963065.

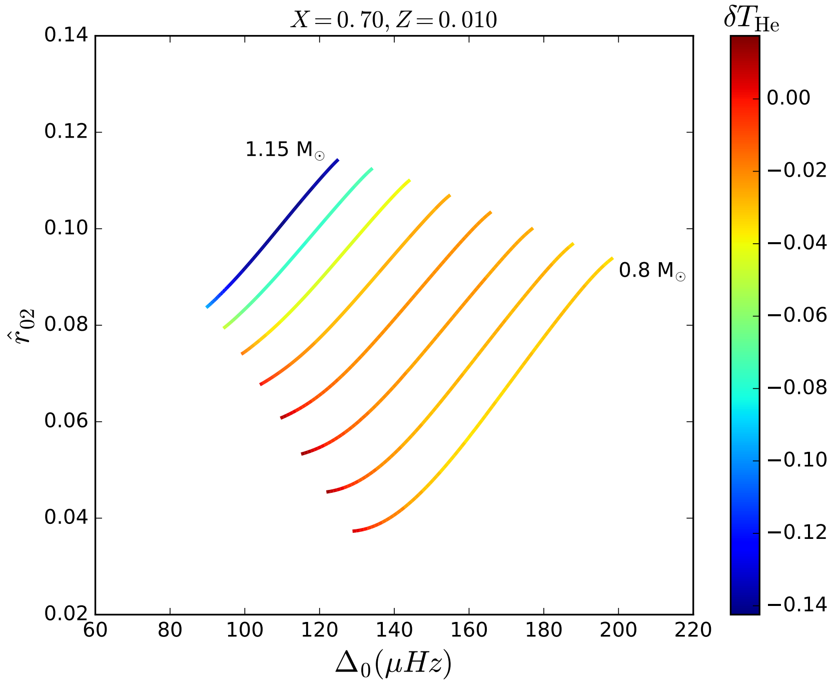

Figure 3.10: The evolution of Δ_0 with $\hat{r}_{02}$ for the masses in the range $[0.8\,M_\odot, 1.15\,M_\odot]$, with a step of $0.05\,M_\odot$, for the case of initial chemical composition of X_0=0.70 and Z_0=0.010. The color scale here corresponds to the relative difference between the 2 values of T_{He}, δT_{He}, fitted for all the tracks simultaneously.

3.2.1 Asteroseismic techniques

In order to derive the stellar parameters from asteroseismic data, there are two kinds of techniques. The first one, which is also the one we used, is the forward modeling. In this technique we use observables of our target in order to retrieve the model that best represents our observations. The observables that can be used for this kind of modeling can be spectroscopic data, like the luminosity (L), the effective temperature (T_{eff}), the surface gravity ($\log g$), or the metallicity ($[Fe/X]$), or seismic quantities like the large frequency separation (Δ), the small frequency separations ($\hat{r}_{0l}$), or even the observed frequencies (ν). The forward techniques try to find the stellar parameters, e.g. $\hat{r}_{01}, \hat{r}_{02}$, of a stellar model that best reproduces the observations, through the minimization of a merit function (χ^2), similar to the one WhoSGlAd uses (Eq. 2.6). The models that are produced by forward modeling, although very close to the observations, do not match perfectly with them. Moreover, the inversion techniques use an alredy existing model and try to bring it even closer to the observations, by applying small changes to the stellar stucture. These changes can be in the profile of one quantity, as the density or the sound speed, or in global indicators, as the mean density. This approach relies on the variational principle, which relates small changes in the stellar structure to small changes in the oscillation frequencies.

Both those techniques use constraints and free parameters. The constraints are the quantities that are used as inputs and the free parameters the quantities that will be adjusted in order to return the constraints. It is important to mention that the minimization techniques, need at least the same number of constrains as free parameters.

3.2.2 The minimization problem

When we perform stellar forward modeling, the goal is to retrieve a set of K stellar parameters a_k, with $k = 1, 2, ...K$, that best reproduce a given set of N observed constraints $C_{i,\text{obs}}$, with $i = 1, 2, ...N$. In order to control the quality of that model, we define a merit function

$$\chi^2(\boldsymbol{a}) = \sum_{i=1}^{N} \frac{(C_{i,\text{obs}} - C_{i,\text{mod}}(\boldsymbol{a}))^2}{\sigma^2}, \tag{3.6}$$

where the subscripts 'obs' and 'mod', correspond to observed and modeled values respectively, σ are for the associated uncertainties, and the vectors are represented by boldface symbols. The merit function measures the squared difference between the observed and the modeled constraints, and all the minimization techniques, try to obtain the smallest value of this function. In our analysis we used the Levenberg-Marquardt technique (Marquardt 1963), which we applied to the modeling of our target, as we show later. When the models depend non-linearly on the set of parameters, the minimization occurs through a series of iterations, which means that, we try to improve an initial value. The procedure stops when the χ^2 is sufficiently low, or when it is not able to be improved anymore.

3.2.2.1 The Levenberg-Marquardt algorithm

The Levenberg-Marquardt technique is not used for the first time, in order to obtain stellar models of high accuracy. For example Miglio & Montalbán (2005) made use of it, for the case of the α Centauri system. We show the developments of that method, as they are given by Press et al. (1992).

When χ^2 is close to its minimum value, we expect that it can be described by a quadratic relation of the form:

$$\chi^2(\boldsymbol{a}) \approx \gamma - \boldsymbol{d} \cdot \boldsymbol{a} + \frac{1}{2} \boldsymbol{a} \cdot \boldsymbol{D} \cdot \boldsymbol{a}, \tag{3.7}$$

where $\boldsymbol{d}$ is an M-vector, $\boldsymbol{D}$ is an $M \times M$ matrix, and γ is a constant. If this approximation is adequate, we can find a better set of parameters ($\boldsymbol{a}_{\mathrm{min}}$), from the current set ($\boldsymbol{a}_{cur}$) by using:

$$\boldsymbol{\alpha}_{\mathrm{min}} = \boldsymbol{a}_{\mathrm{cur}} - \boldsymbol{D}^{-1} \cdot \nabla\chi^2(\boldsymbol{a}_{\mathrm{cur}}), \tag{3.8}$$

where $\boldsymbol{D}$ is the matrix for the second derivatives with respect to the free parameters, or else the Hessian matrix. It is important to note that $\nabla\chi^2(\boldsymbol{a}_{\mathrm{min}}) = 0$. If the approximation is not adequate, then we can only proceed by taking a step down the gradient

$$\boldsymbol{a}_{\mathrm{next}} = \boldsymbol{a}_{\mathrm{cur}} - J\nabla\chi^2(\boldsymbol{a}_{\mathrm{cur}}), \tag{3.9}$$

where J is a constant, and $\boldsymbol{a}_{\mathrm{next}}$ is the newly defined set of best parameters.

By defining

$$\beta_k \equiv -\frac{1}{2}\frac{\partial\chi^2}{\partial a_k}, \tag{3.10}$$

$$\alpha_{k,l} \equiv \frac{1}{2}\frac{\partial^2\chi^2}{\partial a_k \partial a_l}, \tag{3.11}$$

$$\delta a_l \equiv a_{l,\mathrm{next}} - a_{l,\mathrm{cur}}, \tag{3.12}$$

where $\boldsymbol{\delta\alpha}$ is the vector of small increments, we can take a linear form of Eq. 3.8

$$\sum_{l=1}^{K} \alpha_{kl}\delta a_l = \beta_k. \tag{3.13}$$

Now we have a set of linear equations, where the unknowns are the sets δa_l. At the steepest descent, Eq. 3.9 becomes

$$\delta a_l = J\beta_l. \tag{3.14}$$

The inclusion of second-order derivative terms can lead to destabilization, if the model fits badly or if it is contaminated by outlier points, we use a more stable definition of the $\boldsymbol{\alpha}$ matrix, that takes into account only first order derivatives

$$\alpha_{kl} = \sum_{i=1}^{N} \frac{1}{\sigma_i^2}\left[\frac{\partial C_{i,\mathrm{mod}}}{\partial \alpha_k}\frac{\partial C_{i,\mathrm{mod}}}{\partial \alpha_l}\right]. \tag{3.15}$$

If we modify the form of $\boldsymbol{\alpha}$, we will still reach the proper minimum, but from a different iterative route. This is because the condition for the minimum is $\boldsymbol{\beta} = \boldsymbol{0}$, and is independent of how $\boldsymbol{\alpha}$ is defined.

One more problem that needs to be solved is the definition of the J constant in Eq. 3.14. From Eq. 3.10, we see that β_k has the dimensions of $1/\alpha_l$ and, since χ^2 is dimensionless, J must have dimensions of α_l^2. So, its dimension is of $1/\alpha_{ll}$, which is the reciprocal of the diagonal element of the $\boldsymbol{\alpha}$ matrix. We can divide it by a dimensionless factor λ and we have

$$\delta\alpha_l = \frac{1}{\lambda\alpha_{ll}}\beta_l. \tag{3.16}$$

The first difference of the Levenberg-Marquardt method, with respect to the steepest descent is the estimation of J, while its second difference is that we can combine Eqs. 3.13 and 3.16, to redefine the matrix $\boldsymbol{\alpha}$

$$\alpha'_{ll} = (1 + \lambda)\alpha_{ll}, \tag{3.17}$$

$$\alpha'_{kl} = \alpha_{kl}, \tag{3.18}$$

with $k \neq l$. We can now replace Eqs. 3.13 and 3.16 by

$$\sum_{l=1}^{M} \alpha'_{kl} \delta a_l = \beta_k. \tag{3.19}$$

When λ is large, the matrix $\boldsymbol{\alpha}'$ is diagonally dominant and, as a result, Eq. 3.19 becomes identical to Eq. 3.16. On the other hand, when λ is small, Eq. 3.19 becomes identical to Eq. 3.13.

The strength of the Leverberg-Marquardt method lies in the control of λ, in order to converge to one of the cases. By having an initial guess for the parameters of $\boldsymbol{\alpha}$, the technique works as follows

1. First it computes $\chi^2(\boldsymbol{a})$.
2. Afterwards, it picks a modest value for λ.
3. Then, it solves Eqs. 3.19, for δa, and evaluates $\chi^2(\boldsymbol{a} + \delta\boldsymbol{a})$.

The next step, depends on the value of $\chi^2(\boldsymbol{\alpha} + \delta\boldsymbol{\alpha})$. If it is larger than $\chi^2(\boldsymbol{\alpha})$, then in increases λ by a specific factor and returns to the final step of the procedure. If $\chi^2(\boldsymbol{\alpha} + \delta\boldsymbol{a})$ is smaller than $\chi^2(\boldsymbol{\alpha})$, it changes the value of $\boldsymbol{a}$ to be $\boldsymbol{\alpha} + \delta\boldsymbol{\alpha}$, and then returns to the final step. The whole process will eventually stop when the condition for convergence, or for non-convergence, has been met.

When we have finally found the optimal minimum, we set $\lambda = 0$, and we compute the matrix

$$\boldsymbol{C} \equiv \boldsymbol{\alpha}^{-1}, \tag{3.20}$$

which is the covariance matrix of the parameters $\boldsymbol{\alpha}$. The diagonal elements of this matrix correspond to the standard deviations of the individual parameters

$$\sigma(a_k) = \sqrt{(\boldsymbol{\alpha}^{-1}_{kk})}. \tag{3.21}$$

This method has of course its limitations. The first one has to do with the fact that it requires an initial guess. The convergence of the technique, strongly depends on that initial guess. Thankfully, in stellar modeling, we can provide an educated initial guess.

The other disadvantage of the method has to do with the computation of the derivatives. For stellar modeling, the functions $C_{i,\mathrm{mod}}$ do not have an analytical form. However, they are necessary to compute the merit function and their derivatives. As a result, we cannot obtain a formal representation of their derivatives. The most frequently used way to estimate them is by the finite differences

$$\frac{\partial C_{i,\mathrm{mod}}(a_k)}{\partial a_k} \simeq \frac{C_{i,\mathrm{mod}}(a_k + h) - C_{i,\mathrm{mod}}(a_k)}{h}, \tag{3.22}$$

where h is the derivation step. For the choice of h, we have to be careful, because if it is very large, the derivative will not be accurate, but if it is very small, numerical noise might dominate. For our analysis we used the min-cles minimization algorithm, which implements a Leverberg-Marquardt minimization scheme.

3.2.3 The modeling

The last part of my work was the seismic modeling of the solar-like star KIC10963065, from the Kepler Legacy sample, where KIC stands for Kepler Input Catalogue. It is a single star of spectral type F8V with an exoplanet orbiting around it, which has an orbit of about 2.47 days, and radius of $0.82 \pm 0.03 R_{\oplus}$ (Marcy et al. 2014). We computed the seismic indicators, given in Table 3.1, using the frequencies determined by Davies et al. (2015) and for the surface effects we applied the lorentzian

Table 3.1: The seismic parameters that were used as constraints for the fitting.

Δ_0	$\hat{r}_{02}$	$\hat{r}_{01}$	A_{He} (our)	A_{He} (old)
103.76 ± 0.01	0.072 ± 0.001	0.036 ± 0.001	15.08 ± 1.00	15.06 ± 1.00

correction prescribed by Sonoi et al. (2015), as a function of T_{He} and $\log g$. Those seismic indicators were used as constraints in our fitting procedure, that we describe later. The two values of A_{He} that we provide, are for testing the accuracy of our method, as we explain, when we describe how the fitting was carried.

In order to better represent the frequencies we also made the échelle diagram for our target. This kind of diagram is common in asteroseismology and represents the frequencies versus the frequencies over large separation modulo 1. It is like cutting the frequencies, with spacing of the value of the large separation (Δ), and stacking them one over the other. That way, the frequencies appear vertically, grouped based on their spherical degree l. Here, the different spherical degrees are represented by different colors, as they appear in the legend of the plot. Normally, according to the asymptotic theory, they should be exactly one above one another, since they have to be equidistant in frequency, in a power spectrum diagram, but, because of departures from that equidistance due to higher-order terms, and such as the glitches, the expected regularity is disrupted. At first order, we see a departure that creates a parabolic shape, and this is due to the second-order term of the smooth component, as it is shown in Fig. 2.2. There is also however, a higher-order departure, that produces an oscillation around the parabolic shape, and it is mainly due to helium glitch, and to the convection zone glitch. In that plot we have also represented the large separation (Δ), Eq. 2.25, and the second small separation ($\hat{r}_{02}$), Eq. 2.33, as it is given by WhoSGlAd, so that it would be easier to understand what those values actually represent. Δ is the frequency difference between two consecutive frequencies of the same spherical degree, while $\hat{r}_{02}$ is the difference between the mean values of ν/Δ modulo 1, of the spherical degrees l=0 and l=2. The mean values of ν/Δ modulo 1, are shown in the plot with the dashed, vertical lines for each l. The small separation $\hat{r}_{01}$ provides the same difference as $\hat{r}_{02}$, but between the frequencies of spherical degrees l=0 and l=1.

We also show for completeness the power spectrum of our target, as it is given by Davies et al. (2015). We see the expected behaviour for a solar-like star, as it shown in Fig. 1.5 for the case of the Sun. It is clear that the frequencies appear in groups and that they are equally spaced. In this plot, the symbols are the respective points from the échelle diagram. The colors are different from our diagram. The blue squares correspond to frequencies with l=0, the green triangles to frequencies with l=1 and the red circles to frequencies with l=2.

We present the stellar parameters of our target, from other studies, in Table 3.2. In those studies, there was presented a plethora of different parameters. We chose to display only those that are relevant to our analysis, and thus, they will help us compare our results with them. Those parameters are the stellar mass, measured in solar masses ($M_\odot$), the stellar radius, measured in solar radii ($R_\odot$), the age of the star, measured in billion years (Gy), the effective temperature, measured in Kelvin degrees (K), the surface gravity ($\log g$), the stellar luminosity, measured in solar luminosities ($L_\odot$), and the metallicity, ([Fe/H]). We show in the column labeled Marcy, the values from Marcy et al. (2014), in the column labeled Bellinger the values from Bellinger et al. (2019), and in the column labeled Nsamba, the values from Nsamba et al. (2021). The empty places in the table, are due to the fact that the respective studies do not provide that value.

While the Levenberg-Marquardt algorithm is very powerful, see section 3.2.2.1, it is also very sensitive to the initial guesses of the parameters. For that reason, we placed our star in our Δ_0 - $\hat{r}_{02}$ diagram, Fig. 3.13, in order to estimate its mass and age, through a comparison with the values of our grid. The precision of the WhoSGlAd method is also seen by the fact that the errorbars are very small, and so we can get very good first guesses for the aforementioned quantities. Afterwards, we

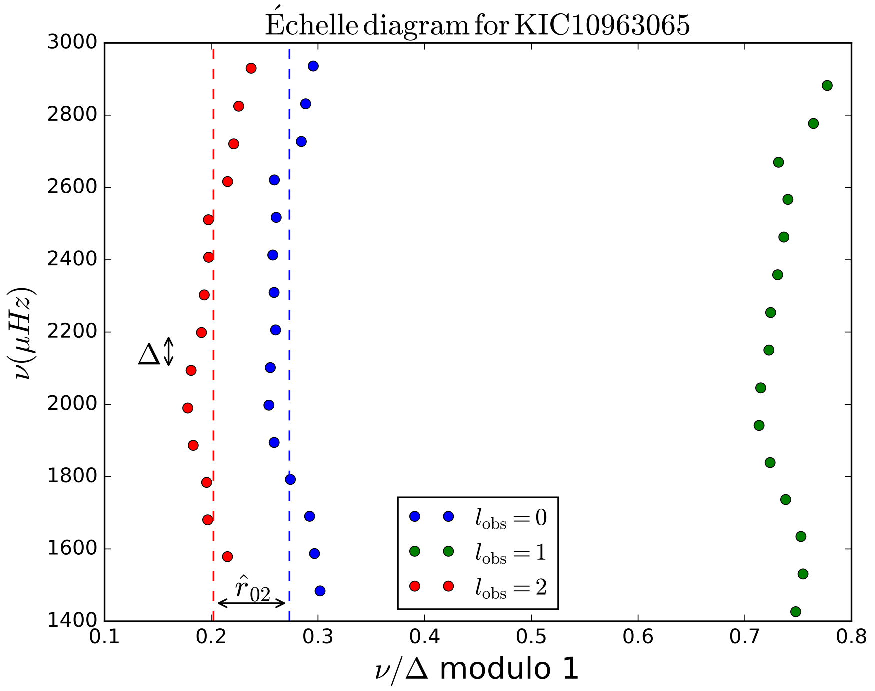

Figure 3.11: The échelle diagram of the star KIC10963065. It shows the frequencies, ν, as a function of ν/Δ modulo 1. The blue diamonds correspond to the frequencies of spherical degree $l = 0$, the green diamonds correspond to the frequencies of spherical degree $l = 1$, and the red diamonds correspond to the frequencies of spherical degree $l = 2$

Table 3.2: Stellar parameters of KIC10963065.

	Marcy	Bellinger	Nsamba
Mass ($M_\odot$)	1.08 ± 0.07	1.065 ± 0.043	1.123 ± 0.044
Radius ($R_\odot$)	1.23 ± 0.03	1.225 ± 0.026	1.244 ± 0.017
Age (Gy)	6.68	4.57 ± 0.48	4.145 ± 0.239
$T_{\rm eff}$ (K)	6104 ± 74	-	6140 ± 77
log$g$	4.294 ± 0.03	-	4.297 ± 0.01
Luminosity ($L_\odot$)	-	1.93 ± 0.13	2.05 ± 0.12
Metallicity	-0.20 ± 0.10	-	-0.19 ± 0.10

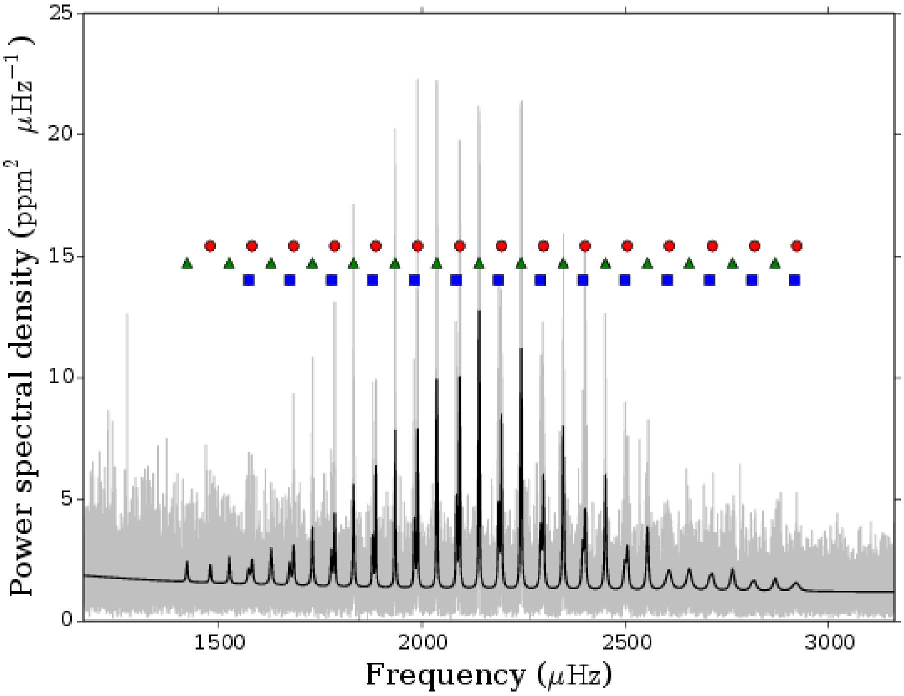

Figure 3.12: The power spectrum of KIC10963065, as it is given by Davies et al. (2015). The blue squares correspond to frequencies with l=0, the green triangles to frequencies with l=1 and the red circles to frequencies with l=2

proceeded in successive adjustments of increasing dimensions. First, we fixed the reference composition and we started for the estimated mass and age, and we adjusted those two parameters, to match the observed Δ_0 and $\hat{r}_{02}$, retrieved by WhoSGlAd. Next, we added $\hat{r}_{01}$ to the constraints and Z_0/X_0 to the parameters. At the end, we adjusted X_0, to represent the observed A_{He}. This process is sensitive to the guesses of the parameters, and so we proceeded in steps, in order to ease its convergence.

The results of our fitting appear in Table 3.3. In that table we show the values of the age, in billion years (Gy), of the mass, in solar masses ($M_\odot$), of the metallicity (Z_0/X_0), and of the hydrogen abundance (X_0), that were used as free parameters, for each step. We also show the values of the χ^2 for each step, in order to show its quality. The column labeled '2 parameters' corresponds to the case when we used only two constraints, the column '3 parameters' corresponds to the case when we use three parameters, and the columns labeled '4 parameters' to the two cases where we used four parameters.

To demonstrate that our method yields results, that are as precise as the old way, we proceeded by using a T_{He} value estimated from a model, we carried two minimization procedures with four parameters: one with our T_{He} estimate, and one with the old estimate. The differences between the two procedures is visible in the A_{He} constraint, as visible in Table 3.1. In order to obtain the A_{He} as in the old procedure, we used the optimal model of the case with the three parameters, in order to obtain the dimensionless helium acoustic depth (T_{He}), Eq. 3.1. We then carried a new modeling with four parameters, with the previous method, Eq. 3.3, in order to observe the impact of the different constraints, on the optimal stellar parameters. We show the values of the helium amplitude in Table 3.1. The results for the former case appear in the column labeled '4 parameters (our)', and for the latter case in the column labeled '4 parameters (old)'. We see that for the cases of the 4 parameters, the value of χ^2 is of the order of 10^{-3}, which is extremely small, and depicts that we can expect an exact solution. Furthermore, it illustrates that our method is as precise as the previous one, and thus

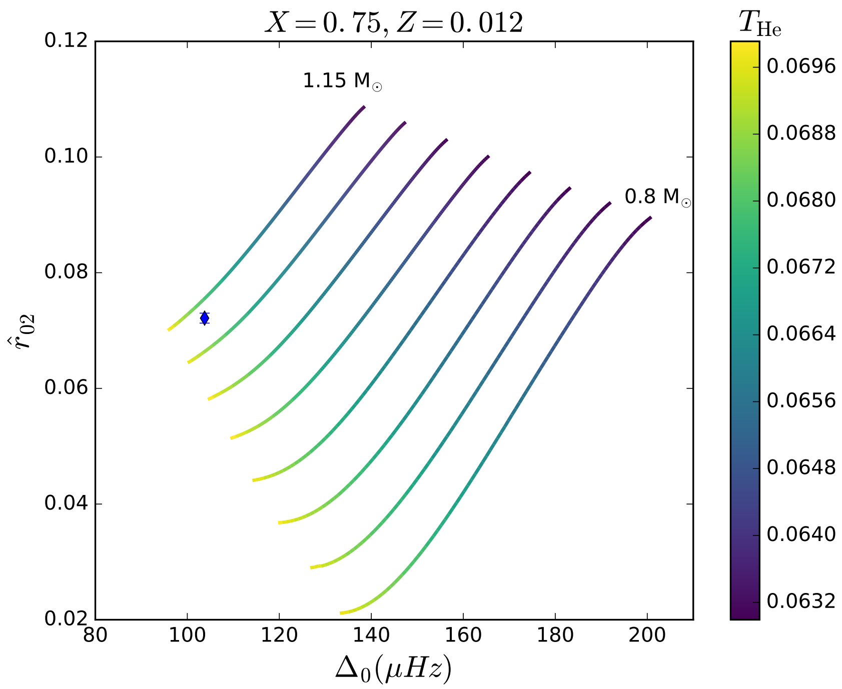

Figure 3.13: The evolution of Δ_0 with $\hat{r}_{02}$ for the 8 different masses, in the range $[0.8\,M_\odot, 1.15\,M_\odot]$, with a step of $0.05\,M_\odot$, for the case of initial chemical composition of X_0=0.75 and Z_0=0.012. The color scale corresponds here to T.

Table 3.3: Parameters of fitting of KIC10963065.

	2 parameters	3 parameters	4 parameters (our)	4 parameters (old)
Age (Gy)	3.960 ± 0.116	4.035 ± 0.127	4.177 ± 0.154	4.188 ± 1.047
Mass ($M_\odot$)	1.151 ± 0.001	1.089 ± 0.023	1.070 ± 0.023	1.070 ± 0.035
Z_0/X_0	-	0.0102 ± 0.002	0.008 ± 0.001	0.008 ± 0.005
X_0	-	-	0.756 ± 0.023	0.756 ± 0.081
χ^2	1.089	2.106	0.004	0.009

can make WhoSGlAd faster. For the values of other important parameters we derived $L/L_\odot = 2.22$, $T_{\rm eff} = 6373K$, for the helium mass fraction, $Y_0 = 0.24$, and for the metallicity a value of -0.35.

It is important to dedicate some time to compare the results of our fitting, shown in Table 3.3, with the values provided for our target from other studies, shown in Table 3.2. We can see that, although in some cases our values, with their respective uncertainties, fall within the ranges of those studies, for example our derived age, agree with those from Bellinger et al. (2019) and Nsamba et al. (2021), there are cases that the values do not agree with each other, for instance, again in the case of our derived age, and that from Marcy et al. (2014). In order to locate the reason behind those disagreements, we must show how those studies were carried.

In the case of Marcy et al. (2014), they used optical 'templates' spectrums from the Keck telescope, and the HIRES echelle spectrometer. And, from those spectra, they retrieved the effective temperature, $T_{\rm eff}$, the surface gravity, $\log g$, and the metallicity [Fe/H]. For targets that presented an asteroseismic signal, like ours, they used the aforementioned three spectroscopic values, for stellar modeling, and so they retrieved more accurate values for the radius and the mass, than the previous values, and, as a result, for the surface gravity. Then, they fed that value to the spectroscopic analysis in order to retrieve more precise results for the T_{eff} and [Fe/H], and, with the new results, they ran one last time the stellar modeling. The fact that they did not use seismic indicators, but spectroscopic ones, could be the reason for deviations from our values for the age, the effective temperature, and the metallicity. Moreover, they carry a fit on the metallicity, something that we do not do, and this can also lead to deviations for the chemical composition. Indeed, the surface metallicity of our optimal model is much smaller than the value they provide. This clearly affects the inferred age, and it can be the reason for the large deviation of the ages. We note here that, from the presented studies, this is the study with the biggest departures form our values.

In the case of Bellinger et al. (2019), the authors wanted to study how the systematic errors and the underestimated uncertainties, of spectroscopic quantities, affect the stellar parameters, through stellar modeling. They used approximate scaling relations to obtain stellar radii (R), mean stellar densities (ρ), and stellar masses (M). Those relations use the effective temperature of the star (T_{He}), that is retrieved spectroscopically, the large separation ($\Delta\nu$), and the frequency of maximum oscillation power ($\nu_{\max}$). The fact that those relations are scaling, means that they make correlations with the respective values for the Sun. The values that they used for the solar reference values are $T_{\text{eff}\odot} = 5772$ K, $\nu_{\max\odot}$=309 ± 30 μHz, and $\Delta\nu_{\odot} = 135.1$ μHz. They created a large grid of models of solar-like stars, and they also obtained oscillation frequencies from observed stars, that implemented on the grid, to obtain their stellar parameters. They obtained their seismic data by calculating frequency separations and ratios, as in Roxburgh & Vorontsov (2003b). Their derived values agree with ours, except for the luminosity (L), which shows a small departure. This could have happened because of the different choice for the solar values.

Finally, in the case of Nsamba et al. (2021), the authors made three different stellar grids, by only varying the treatment of initial helium mass fraction. Their purpose was to study, how its value affects the general properties of a star, since this quantity is the most difficult to be derived. This is due to the fact that we cannot obtain it spectroscopically, because the surface temperature of solar-like stars, is not high enough to excite helium, and so few or no helium lines can be observed. They used the seismic data from Lund et al. (2017), where the large separation ($\Delta\nu$), is obtained by a linear fit in the frequencies of spherical degree l=0, expressed as a function of the radial order. Although they retrieved different results for each case, we show the values from the grid that is closer to our analysis. This is the one, in which they let the helium mass fraction free, something that we did too. In the other two grids they assumed a galactic enrichment relation (relating helium abundance to metal abundance), with fixed values for the helium-to-heavy element enrichment ratio ($\Delta Y/\Delta Z$), of 1.4 and of 2.0. They considered diffusion in their models, but that there is no overshooting between the convective envelope and the radiative zone, as we did. Our values agree for the mass, the age, and the radius. A large difference exists for the effective temperature (T_{He}), and the metallicity, due to the fact that those values where obtained spectroscopically, by Buchhave & Latham (2015). Furthermore, there is a small disagreement when it comes to the luminosity, probably because of the influence of the effective temperature (T_{He}), and the metallicity and, they are not used as constraints in our study. In Fig. 3.14 we show in an HR diagram, the position of our best model for our target, with the diamond, and with the black box and cross the values from observations, with the associated uncertainties. The values of the observations are from Nsamba et al. (2021). Those differences are probably due to the fact that their values come from spectroscopic observations, while ours come from the best model of the fitting procedure, using seismic indicators, and they were not part of our fitting.

In Fig. 3.15, we compare, in an échelle diagram, the observed frequencies, depicted with the circles, and those that we get from our best model, depicted with the diamonds. There is a big offset between those sets of values, although the general bahaviour of the curves remains the same. We identified the reason for that offset to be the difference in the mean $\hat{\epsilon}$, retrieved in both cases, which eventually affects the value of the frequencies through Eq. 2.13. We retrieved $\hat{\epsilon} = 1.027$ for the case of the model and $\hat{\epsilon} = 0.251$ for the case of the observations. This difference creates the almost 0.2 difference

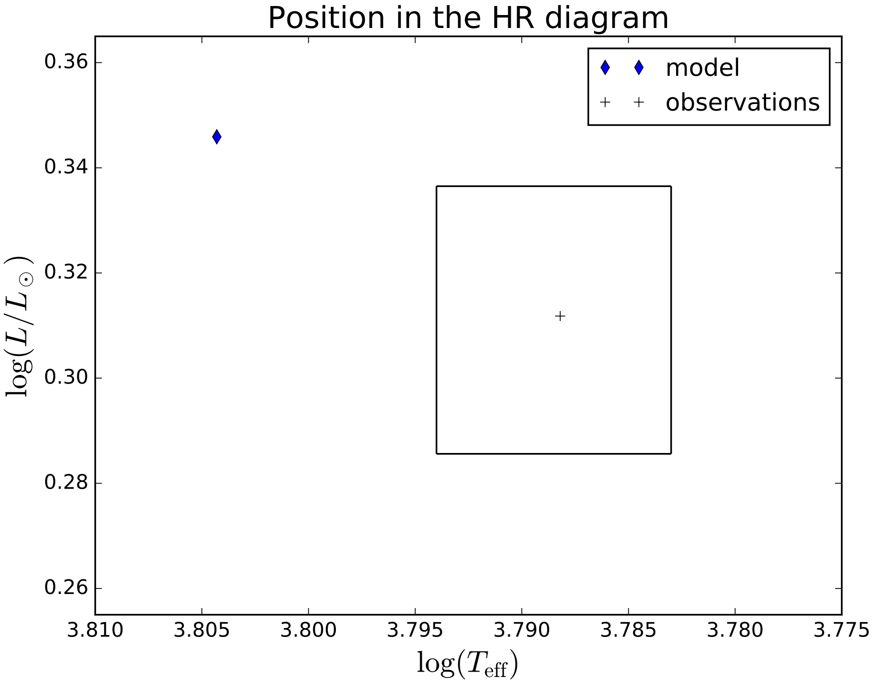

Figure 3.14: HR diagram for our target. The values of the observations are taken from Nsamba et al. (2021).

in the abscissa, in view of the fact that it represents the frequencies over large separation modulo 1. The difference in the case of the observations might be created because of the corrections for the surface effects using the relation prescribed by Sonoi et al. (2015). In Farnir et al. (2019), the authors show that this correction, it still does not give the best agreement with observations, and a difference between observations and models remains. Moreover, this was not part of the fitting constraints, and so, we can expect that they do not match.

In Fig. 3.16 we show the values for the glitches ($\delta\nu$), in μHz, as a function of the frequencies (ν), also in μHz. The observed data are the blue lines with their errorbars, and our best model are the diamonds. Moreover we show their fit, where the blue line is for the observations and the black line is for the model. In Farnir et al. (2019), the authors show that with WhoSGlAd, the observed and fitted glitches are close in amplitude and period. In our case, although the two sets follow the same behaviour when it comes to the period, we can clearly see that there is a significant horizontal offset between them. This is again due to the $\hat{\epsilon}$ difference that affects the frequencies ν, as in the case of the échelle diagram, Fig. 3.15. There is also a vertical offset, which could be due to a difference in the phase of the glitches. However, the amplitude is correctly fitted.

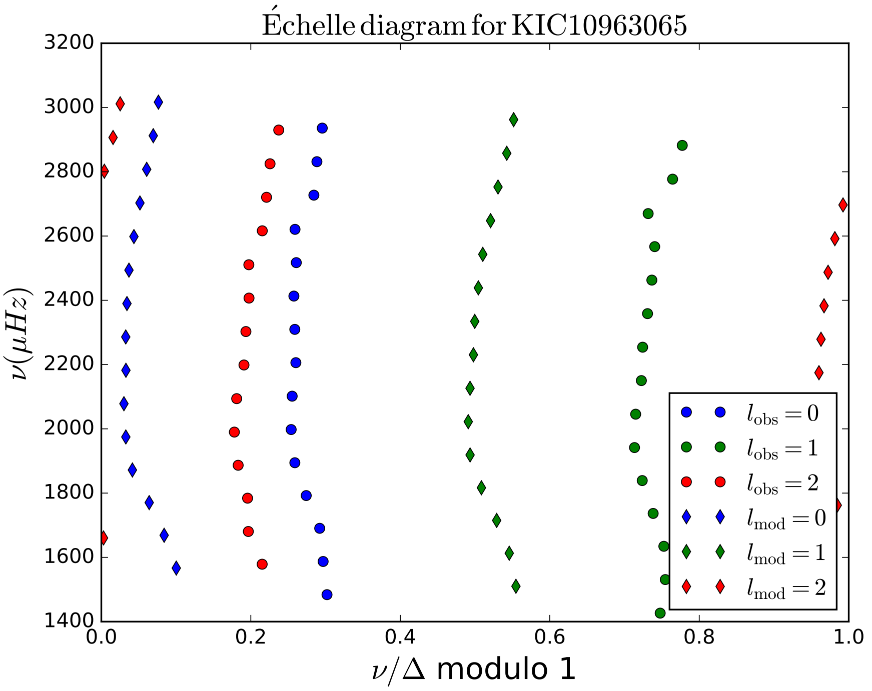

Figure 3.15: The échelle diagram of our target, with frequencies from observations and from our best model.

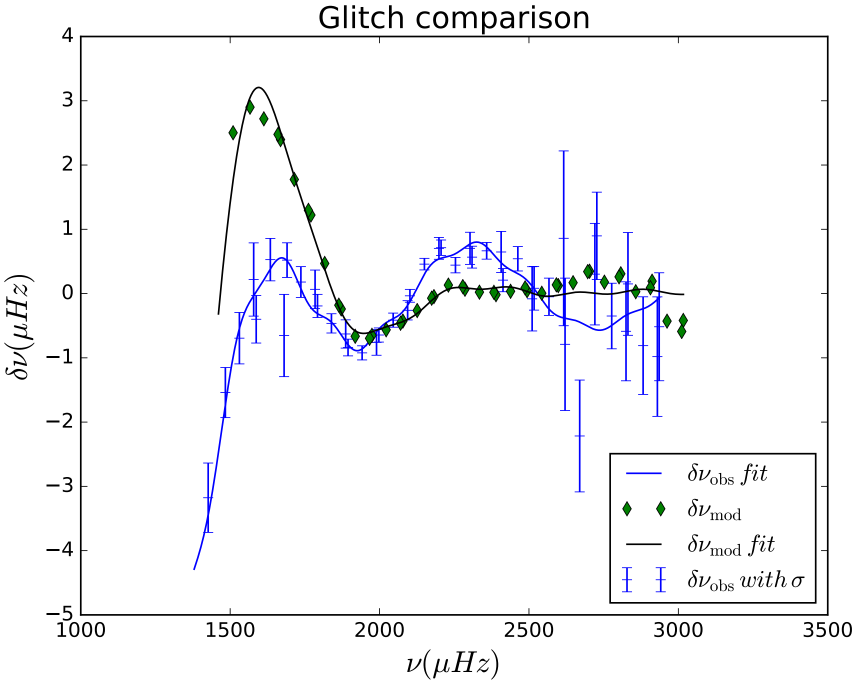

Figure 3.16: Comparison between the glitch amplitude of our observed frequencies and the amplitude of the frequencies of our best model. For the observed data are the blue lines with their errorbars, and for our best model are the diamonds. Moreover we show their fit, where the blue line is for the observations and the black line is for the model.

Chapter 4

Conclusions

In the present work, we developed a new method that provides a value for the dimensionless helium acoustic depth, T_{He}, as it is given by Eq. 3.2 and shown in Farnir et al. (2019). Using as observables the seismic indicators Δ_0 and $\hat{r}_{02}$, as it appears in Eq. 3.3, and as they are defined in WhoSGlAd method. That way we reduce significantly the time needed to retrieve the helium amplitude, A_{He}, when working with observations. This is a very important value because it works as a proxy for the helium abundance, in the region of the second helium ionization zone, which is located quite close to the surface. The proximity of that area to the stellar photosphere, and the fact that in this region, solar-like stars are fully convective, allows us to consider that helium abundance of that area is the same as that of the surface. The knowledge of the surface helium abundance allows us to improve our models and thus, better constrain processes, like mixing and transport processes, that affect the evolution of the star. For solar-like stars, this is the only way to retrieve it, since spectroscopically this value is not available.

We used the large separation Δ, and the small separation $\hat{r}_{02}$ in a linear relation, Eq. 3.2, in order to retrieve a value for the dimensionless helium acoustic depth T_{He}. We chose those two seismic indicators because, as it was presented in Farnir et al. (2019) and as it is shown in Fig. 3.1, they are connected by an almost monotonous relation, and so we could easily see whether or not T_{He}, was linearly connected to them. Indeed, we proved that this is the case in Fig. 3.5. The obtained value of T_{He} is used to retrieve A_{He}. We used WhoSGlAd for our analysis because that method takes advantage of both the information contained in the smooth part of the spectrum and in the glitches to provide seismic indicators as little correlated as possible by using the Gram-Schmidt algorithm.

Since our technique uses a linear relation, it is fast, and thus, it can be implemented in existing pipelines of stellar data processing, in order to give results in an automatic way, for large amounts of data. Past space missions, such as CoRoT (Baglin et al. 2009) and *Kepler* (Borucki et al. 2010), and the ongoing TESS space mission (Ricker et al. 2014) provide such large amounts of data. Future space missions, such as PLATO (Rauer et al. 2014), are expected to provide them as well. This makes it clear that small computation times are necessary, so that we can study more targets at the same time.

Furthermore, as explained in section 3.1, a value for the helium amplitude is needed, because it is one of the few ways to constrain the surface He abundance. We remind that this quantity is not available spectroscopically, and asteroseismology can provide an accurate value, through stellar modeling. Before our method, this was found by computing a model representative of most featuresof the stellar structure of our target.

Before implementing our method, we validated it by comparing its results to the original approach. We used a grid of models with a specific initial chemical composition, and we computed the differences given by the two approaches, and found that they are very low. The maximum difference reaches up to values of about 1.5 %. This is small, as Farnir et al. (2019), found that a 10 % difference still has a negligible impact on A_{He}. Then we used the fitting coefficients from previously, to test our method for a different initial chemical composition, and we showed that it works for that case too. Although in that case the maximum differences are up to about 3 %, which remains well below the 10 % example given in Farnir et al. (2019), for the deviation of the method, still returns accurate results. We also verified that our method is efficient, by comparing the values retrieved for the helium amplitude with our method and with the previous approach, for the case of 16 Cygni A, the same target that was used by Farnir et al. (2019). With the original method we obtained $A_{\mathrm{He}} = 29.6$, while with our method we obtained $A_{\mathrm{He}} = 29.1$. This difference is in the range of the σ of the helium amplitude in WhoSGlAd, which is equal to 1. That discussion proves the validity of our method.

However, our method is only useful for observations. When we process models, we have access to its structure and so we can easily retrieve the position of the helium glitch and of the sound speed profile from that point up to the stellar surface. Thus, the calculation of τ_{He}, is done by Eq. 3.1. This is a more efficient, accurate, fast and easy way, than the proposed method.

In addition, because our method uses seismic indicators provided by the WhoSGlAd method, the limits of that method apply to our method as well. Those limitations have to do mostly with cases where the linearity of the method breaks, and those cases are for stars that have evolved beyond the main-sequence phase, and for stars that have developed a convective core. WhoSGlAd can still provide accurate indicators for the smooth part of the spectrum, for those cases. Nonetheless, the values that depend on the glitches, for instance the dimensionless helium acoustic depth, (T_{He}), and the helium amplitude, (A_{He}), are not accurate.

Future perspectives would be to test our method for a larger range of initial chemical compositions, in order to see whether or not our method remains efficient for a larger sample of stars. Furthermore, we think that it would be interesting to investigate, whether or not a second order expression such as:

$$T_{\mathrm{He}} = a\Delta_0^2 + b\Delta_0 + c\hat{r}_{02}^2 + d\hat{r}_{02} + e\Delta_0\hat{r}_{02} + f, \tag{4.1}$$

where a, b, c, d, e and f are newly defined coefficients, could give more precise results than Eq. 3.3. On the one hand, the fact that this expression is of 2nd order, could indeed lead to better fit, while using only the same seismic indicators, Δ_0 and $\hat{r}_{02}$, as our relation, Eq. 3.2. On the other hand, we proved in our analysis, that the departures from the correct value, by using the proposed method, are insignificant, and do not result in errors in the derived values for the helium amplitude (A_{He}), meaning that it might not be useful to sacrifice the small computation times of our method, for slightly better results.

Appendix A

Nuclear reactions

As we said before, Solar like stars generate their energy in their core where the weight of the gas column above it makes it possible for thermonuclear reactions to take place. There are two cycles that can be at work and in both of them after a chain of reactions four protons (hydrogen nucleus) will give one alpha particle (helium nucleus), two positrons (e^+), two neutrinos (ν) and energy:

$$4\,^1\mathrm{H} \rightarrow\,^4\mathrm{He} + 2e^+ + 2\nu + 26.33MeV \tag{A.1}$$

One of those cycles is the proton-proton (pp) chain and in that cycle we begin with the production of deuterium (^{2}H) from two protons by the two following reactions:

$$^1\mathrm{H} +^1\mathrm{H} \rightarrow\,^2\mathrm{H} + e^+ + \nu \tag{A.2}$$

$$^1\mathrm{H} +^1\mathrm{H} + e^- \rightarrow\,^2\mathrm{H} + \nu \tag{A.3}$$

where the second one only takes place in 0.25%. Both those reactions are very slow, 10^{10} years in the former case and 10^{12} years in the latter and so they determine the duration of the whole pp chain. Then, the produced deuterium captures a proton and produces one ^{3}He:

$$^2\mathrm{H} +^1\mathrm{H} \rightarrow\,^3\mathrm{He} + \gamma \tag{A.4}$$

After that reaction, we have three different possibilities for the rest of the cycle. The first one is also the most possible and happens at about 85% of the times:

$$^3\mathrm{He} +^3\mathrm{He} \rightarrow\,^4\mathrm{He} + 2\,^1\mathrm{H} \tag{A.5}$$

The second one is quite rare:

$$^3\mathrm{He} +^1\mathrm{H} \rightarrow\,^4\mathrm{He} + e^+ + \nu \tag{A.6}$$

The third one starts with:

$$^3\mathrm{He} +\,^4\mathrm{He} \rightarrow\,^7\mathrm{Be} + \gamma \tag{A.7}$$

and is followed either by:

$$^7\mathrm{Be} + e^- \rightarrow\,^7\mathrm{Li} + \nu \tag{A.8}$$

$$^7\mathrm{Li} +\,^1\mathrm{H} \rightarrow\,2\,^4\mathrm{He} \tag{A.9}$$

either by:

$$\begin{aligned} {}^{7}\mathrm{Be} + {}^{1}\mathrm{H} &\rightarrow {}^{8}\mathrm{B} + \gamma \\ {}^{8}\mathrm{B} &\rightarrow {}^{8}\mathrm{Be} + e^{+} + \nu \\ {}^{8}\mathrm{Be} &\rightarrow 2\,{}^{4}\mathrm{He} \end{aligned}$$

with the third possibility being the one that gives neutrinos of high energy that are detected by neutrino detectors on Earth. All the positrons (e^+) that are produced from those reactions are almost immediately annihilated by electrons (e^-) and produce energy in the form of γ rays. The other cycle that produces He from 4 protons is the CNO (Carbon-Nitrogen-Oxygen) cycle which needs high temperatures to take place and is dominant in high mass stars. In the case of the Sun the pp chain is the dominant cycle and counts to about 99% of the reactions and that's why we won't go into the details for the CNO cycle.

Appendix B

Other compositions

Here we show plots like Fig. 3.5, showing the relative differences between T_{He}, calculated with our method and with the integral relation, of models of different initial chemical compositions. The chemical compositions of those plots, are those from the grid that we made, and did not present in our analysis, because that would be redundant. The sets of initial hydrogen abundance (X_0), and of initial metallicity (Z_0/X_0), that are shown here are: $X_0 = 0.70$ and $Z_0/X_0 = 0.012$, $X_0 = 0.70$ and $Z_0/X_0 = 0.014$, $X_0 = 0.725$ and $Z_0/X_0 = 0.010$, $X_0 = 0.725$ and $Z_0/X_0 = 0.012$, $X_0 = 0.75$ and $Z_0/X_0 = 0.010$, $X_0 = 0.75$ and $Z_0/X_0 = 0.014$ respectively. For all the cases, we see that the value of δT_{He} remains small, which proves the accuracy of our method.

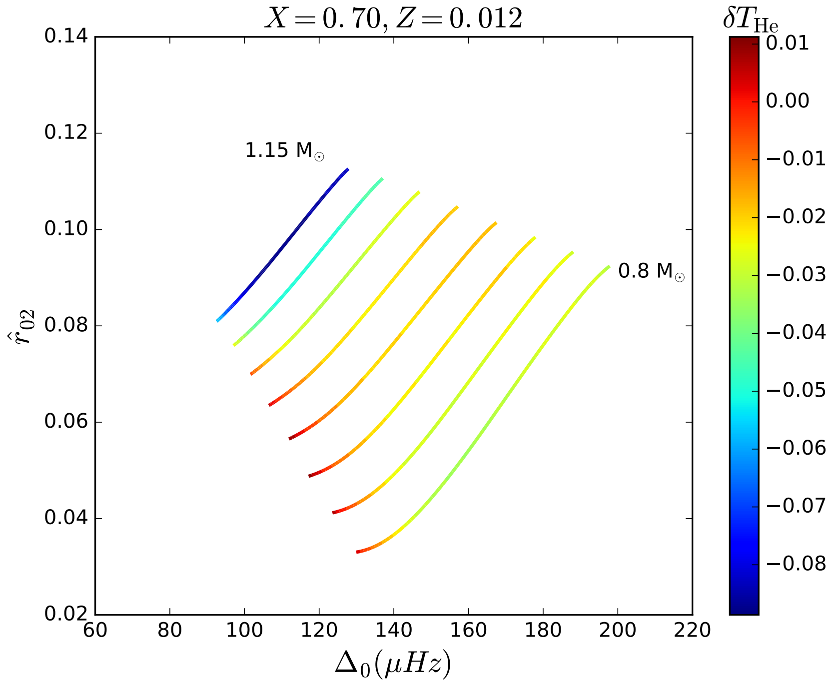

Figure B.1: The evolution of Δ_0 with $\hat{r}_{02}$ for masses in range $[0.8\,M_\odot, 1.15\,M_\odot]$ with a step of $0.05\,M_\odot$, for the case of initial chemical composition of X_0=0.70 and Z_0=0.012. The color scale here corresponds to the relative difference between the 2 values of $T_{\rm He}$, $\delta T_{\rm He}$.

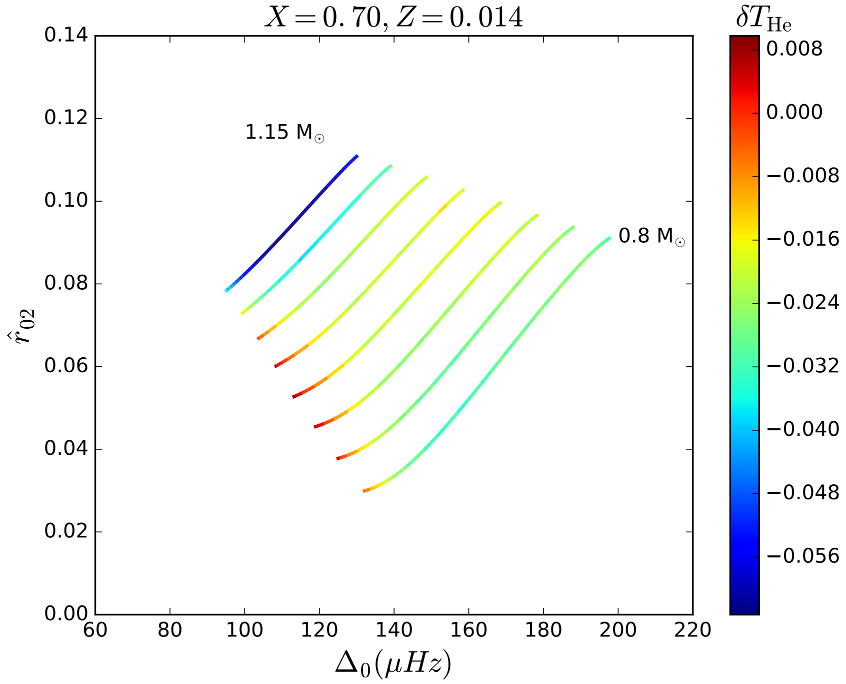

Figure B.2: The evolution of Δ_0 with $\hat{r}_{02}$ for masses in range $[0.8\,M_\odot, 1.15\,M_\odot]$, with a step of $0.05\,M_\odot$, for the case of initial chemical composition of X_0=0.70 and Z_0=0.014. The color scale here corresponds to the relative difference between the 2 values of $T_{\rm He}$, $\delta T_{\rm He}$.

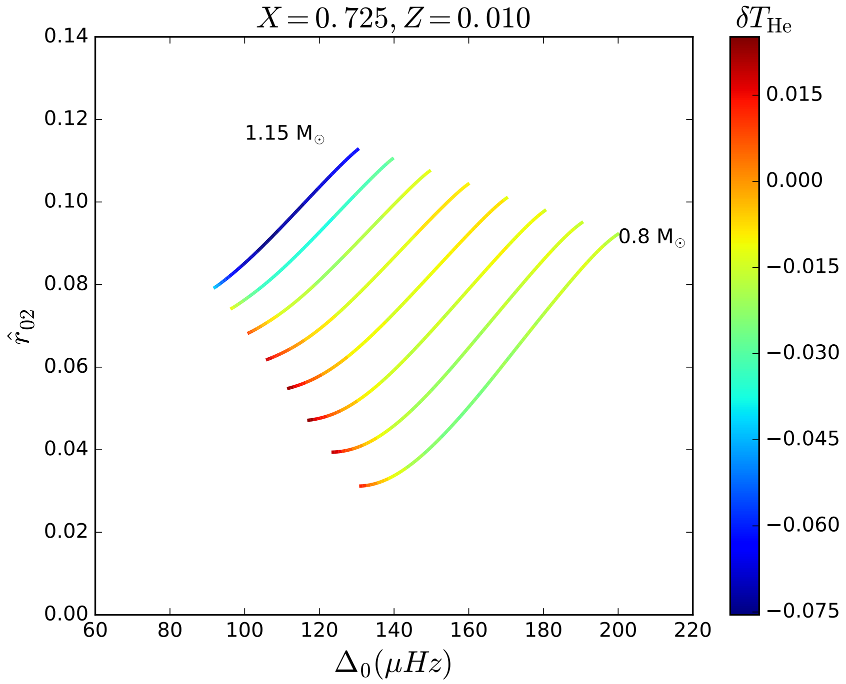

Figure B.3: The evolution of Δ_0 with $\hat{r}_{02}$ for masses in range $[0.8\,M_\odot, 1.15\,M_\odot]$ with a step of $0.05\,M_\odot$, for the case of initial chemical composition of X_0=0.725 and Z_0=0.010. The color scale here corresponds to the relative difference between the 2 values of T_{He}, δT_{He}.

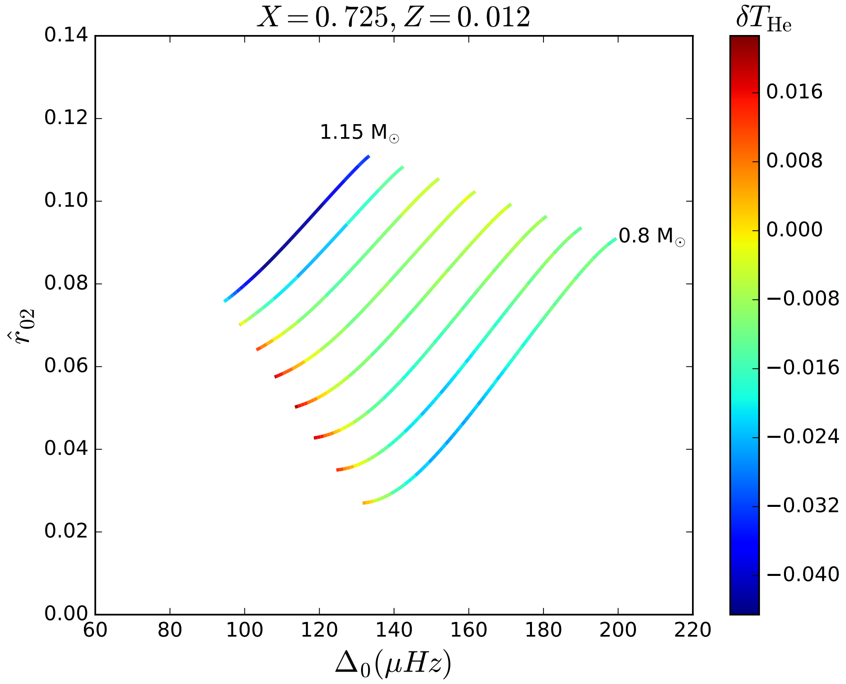

Figure B.4: The evolution of Δ_0 with $\hat{r}_{02}$ for masses in range $[0.8\,M_\odot, 1.15\,M_\odot]$ with a step of $0.05\,M_\odot$, for the case of initial chemical composition of X_0=0.725 and Z_0=0.012. The color scale here corresponds to the relative difference between the 2 values of T_{He}, δT_{He}.

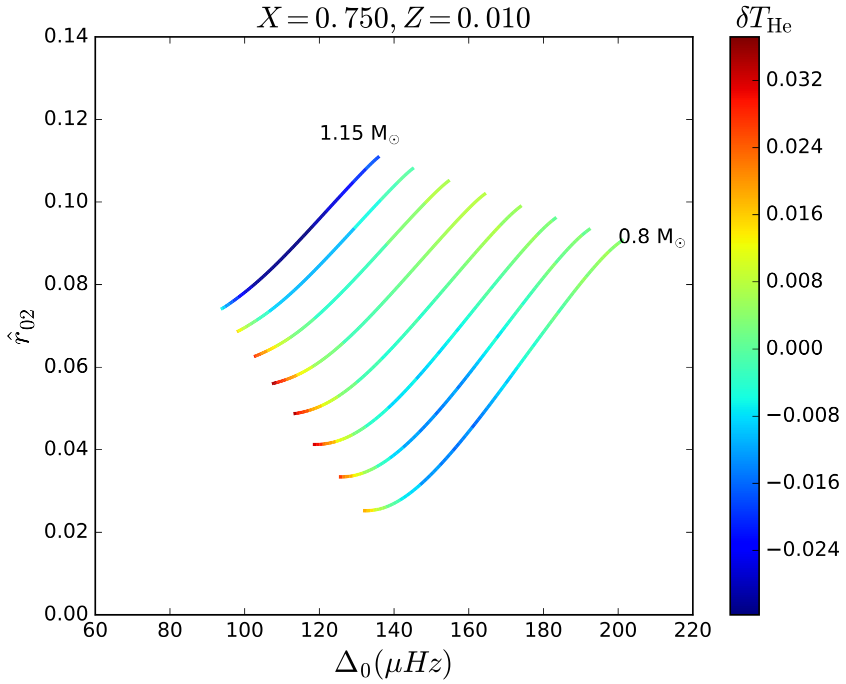

Figure B.5: The evolution of Δ_0 with $\hat{r}_{02}$ for masses in range $[0.8\,M_{\odot}, 1.15\,M_{\odot}]$ with a step of $0.05\,M_{\odot}$, for the case of initial chemical composition of X_0=0.75 and Z_0=0.010. The color scale here corresponds to the relative difference between the 2 values of T_{He}, δT_{He}.

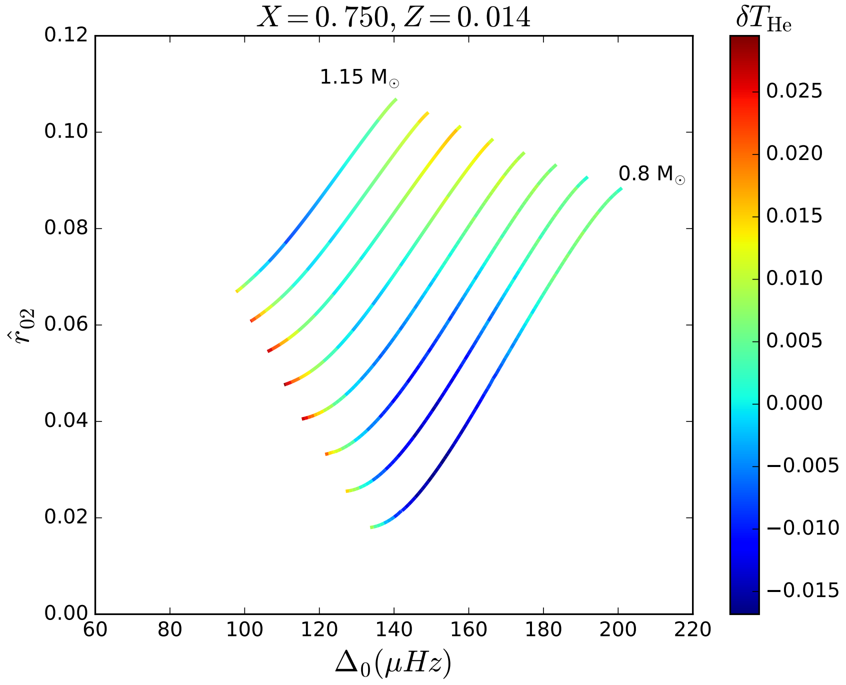

Figure B.6: The evolution of Δ_0 with $\hat{r}_{02}$ for masses in range $[0.8\,M_{\odot}, 1.15\,M_{\odot}]$ with a step of $0.05\,M_{\odot}$, for the case of initial chemical composition of X_0=0.75 and Z_0=0.014. The color scale here corresponds to the relative difference between the 2 values of T_{He}, δT_{He}.

Bibliography

Adelberger, E. G., García, A., Robertson, R. G. H., et al. 2011, Reviews of Modern Physics, 83, 195

Asplund, M., Grevesse, N., Sauval, A. J., & Scott, P. 2009, ARA&A, 47, 481

Baglin, A., Auvergne, M., Barge, P., et al. 2009, in Transiting Planets, ed. F. Pont, D. Sasselov, & M. J. Holman, Vol. 253, 71–81

Bellinger, E. P., Hekker, S., Angelou, G. C., Stokholm, A., & Basu, S. 2019, A&A, 622, A130

Borucki, W. J., Koch, D., Basri, G., et al. 2010, Science, 327, 977

Buchhave, L. A. & Latham, D. W. 2015, ApJ, 808, 187

Cassisi, S., Salaris, M., & Irwin, A. W. 2003, ApJ, 588, 862

Chaplin, W. J. & Miglio, A. 2013, ARA&A, 51, 353

Christensen-Dalsgaard. 2003

Christensen-Dalsgaard, J. 1988, in Advances in Helio- and Asteroseismology, ed. J. Christensen-Dalsgaard & S. Frandsen, Vol. 123, 295

Davies, G., Silva Aguirre, V., Bedding, T., et al. 2015, Monthly Notices of the Royal Astronomical Society, 456

de Meulenaer, P., Carrier, F., Miglio, A., et al. 2010, A&A, 523, A54

Deheuvels, S., Brandão, I., Silva Aguirre, V., et al. 2016, A&A, 589, A93

Farnir, M., Dupret, M. A., Salmon, S. J. A. J., Noels, A., & Buldgen, G. 2019, A&A, 622, A98

Ferguson, J. W., Alexander, D. R., Allard, F., et al. 2005, ApJ, 623, 585

Gough, D. O. 1986, Highlights of Astronomy, 7, 283

Houdek, G. & Gough, D. O. 2007, MNRAS, 375, 861

Iglesias, C. A. & Rogers, F. J. 1996, ApJ, 464, 943

Lebreton, Y. & Goupil, M. J. 2014, A&A, 569, A21

Lund, M. N., Silva Aguirre, V., Davies, G. R., et al. 2017, ApJ, 850, 110

Marcy, G. W., Isaacson, H., Howard, A. W., et al. 2014, ApJS, 210, 20

Marquardt, D. W. 1963, SIAM Journal on Applied Mathematics, 11, 431

Miglio, A. & Montalbán, J. 2005, A&A, 441, 615

Nsamba, B., Moedas, N., Campante, T. L., et al. 2021, MNRAS, 500, 54

Press, W. H., Teukolsky, S. A., Vetterling, W. T., & Flannery, B. P. 1992, Numerical recipes in FORTRAN. The art of scientific computing

Rauer, H., Catala, C., Aerts, C., et al. 2014, Experimental Astronomy, 38, 249

Ricker, G. R., Winn, J. N., Vanderspek, R., et al. 2014, in Society of Photo-Optical Instrumentation Engineers (SPIE) Conference Series, Vol. 9143, Space Telescopes and Instrumentation 2014: Optical, Infrared, and Millimeter Wave, ed. J. Oschmann, Jacobus M., M. Clampin, G. G. Fazio, & H. A. MacEwen, 914320

Roxburgh, I. W. & Vorontsov, S. V. 2003a, A&A, 411, 215

Roxburgh, I. W. & Vorontsov, S. V. 2003b, A&A, 411, 215

Scuflaire, R., Montalbán, J., Théado, S., et al. 2008, Ap&SS, 316, 149

Sonoi, T., Samadi, R., Belkacem, K., et al. 2015, A&A, 583, A112

Ulrich, R. K. 1986, ApJ, 306, L37

Verma, K., Faria, J. P., Antia, H. M., et al. 2014, ApJ, 790, 138